Atomic layer deposited nickel oxide for perovskite solar cells

Dučinskas, Algirdas

Award date:
2018

Technische Universiteit
Eindhoven
University of Technology

Department of Mechanical Engineering
Sustainable Energy Technology

Atomic layer deposited nickel oxide for perovskite solar cells

Master Thesis

Algirdas Dučinskas

Master program: Sustainable Energy Technology
Defence date: 14^{th} of September 2018

Supervisors:
Dr. M. Creatore (Graduation professor)
D. Koushik (Daily supervisor)

Research performed at Department of Applied Physics
Plasma and Materials Processing group

Eindhoven, September 2018

TU/e Technische Universiteit Eindhoven University of Technology

Declaration concerning the TU/e Code of Scientific Conduct for the Master's thesis

I have read the TU/e Code of Scientific Conduct[i].

I hereby declare that my Master's thesis has been carried out in accordance with the rules of the TU/e Code of Scientific Conduct

Date

30/08/2018

Name

Algirdas Dučinskas

ID-number

1279890

Signature

Submit the signed declaration to the student administration of your department.

[i] See: http://www.tue.nl/en/university/about-the-university/integrity/scientific-integrity/
The Netherlands Code of Conduct for Academic Practice of the VSNU can be found here also.
More information about scientific integrity is published on the websites of TU/e and VSNU

Abstract

Over the last decade, perovskite solar cells have drawn a tremendous attention owing to phenomenal improvement in power conversion efficiency (PCE), which in less than a decade have reached 23.3 %. Currently, most of the efficient solar cells employ organic hole transport layers like Spiro-MeOTAD, PTAA. However, these materials are costly, not environmentally stable and suffer from optical absorption losses. These drawbacks have induced a search for alternative inorganic hole transport materials, which are cheap and have high environmental stability and do not exhibit parasitic light absorption. One of the good candidates is nickel oxide (NiO_x), which is a wide bandgap p-type semiconductor. In this work, NiO_x has been investigated as a hole transport layer in inverted planar perovskite solar cells (PSC). Ultra-thin 10 nm, polycrystalline, having a E_g of 3.8 eV NiO_x films have been processed by plasma-enhanced atomic layer deposition (ALD) technique. When these films have been implemented in perovskite solar cells, a power conversion efficiency of 13.15 % has been achieved.

Furthermore, the NiO_x/perovskite interface has been investigated under three conditions. Next to the analysis of pristine NiO_x films, films have also been post-annealed in air at 150°C for 1 hour or at 300°C for 20 minutes. It has been demonstrated that perovskite solar cells based on NiO_x post-annealed at 300°C exhibit the best efficiency compared to the other two cases. Champion cell yields a short-circuit current (J_{SC}) of 20.73 (mA/cm^2), open-circuit voltage (V_{OC}) of 1.005 (V), fill factor (FF) of 73.57 (%) and power conversion efficiency PCE of 15.33(%). However, perovskite solar cells having NiO_x films post-annealed at 150° C exhibit even lower PCE than solar cells based on pristine NiO_x. In order to elucidate the reasons for changes in PCE, NiO_x films have been investigated by means of XPS. It has been found that with annealing temperature NiO_x surface dehydroxylates. Furthermore, UPS analysis has revealed that upon post-annealing treatment Fermi level shifts closer to the valence band, thus NiO_x films become more p-type. In addition to that, it has been shown that NiO_x ionization potential is also affected by post-annealing treatment. Surprisingly, it has been found that the best perovskite and NiO_x valence band alignment (off-set 0.55 eV) is achieved in case of annealing at 150 °C, which results in the lowest PCE. In contrast to this, the valence band off-set between perovskite and NiO_x annealed at 300 °C is the highest (0.74 eV). These findings strongly suggest that valence band alignment is not sufficient to guarantee high solar cell performance. In fact, this work has revealed that NiO_x/perovskite interface is crucial for efficient solar cells and reduction in surface hydroxyl groups results in more efficient solar cells.

Acknowledgement

I have to admit that this MSc project was the most interesting, driving and challenging task that I have done in my life so far. I cannot imagine that this project could have been completed without the help and support from people, who guided and assisted me in this journey. Therefore, I would like to show gratitude and appreciation to all, who motivated, educated, discussed me.

Firstly, I would like to thank Adriana, who gave me the opportunity to carry out MSc thesis in the field of perovskite cells and continuously supported and help me. I really appreciate your patience and time on correcting my thesis and giving advices.

Secondly, I would like to show my gratitude to Dibya. You have helped me tremendously by explaining experimental set-ups, sharing literature, discussing results and sharing experimental results and your opinion. I am also very thankful for your assistance in writing my thesis. You have checked dozen of times my thesis and I imagine that it is not the most exciting work to do.

Thirdly, I would like to thank Christian for XPS and training and instructions in cleanr room and for AR-XPS measurements, Christ for UPS analysis, Marcel for TEM images, Michele Sessolo (from University of Valencia) for APS analysis, Marko Jost (from HZB) for manufacturing perovskite solar and measuring their performance.

In addition, I would like to show appreciation to my friends in Eindhoven and in Lithuania, who were around and cheered me up and made my studies full of adventures.

Most importantly, I would like to thank my family and my girlfriend for constant love, support and empathy, for motivating me and staying with me in every decision I make.

Contents

Chapter 1

Introduction

According to International Energy Agency, in 2015 more than four-fifths ($\approx$ 81.2%) of total primary energy supply came from fossil fuels such as oil, gas and coal [1]. These fossil fuels are the main source of carbon dioxide (CO_2) generation. In nature, CO_2 is recycled by plants during photosynthesis process. Currently, the generation rate of CO_2 is much faster than nature's capabilities. Thereby, the concentration of CO_2 in the atmosphere is increasing and this has led to the growing average global temperature. As stated by national air and space agency (NASA), this year average global temperature is 0.8 °C above the pre-industrial levels (see Figure 1.1). The changes in weather patterns have been experienced all around the globe. For instance, in 2018 the Netherlands recorded the hottest night ever [2].

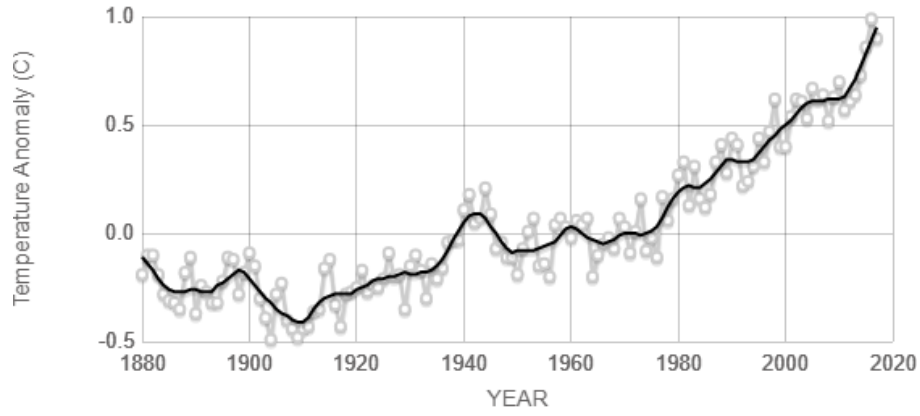

Figure 1.1: Deviation of annual global temperature from pre-industrial levels. Adopted from [3].

Environmentalists alert that if in the coming decades carbon CO_2 concentration in the atmosphere is not substantially and gradually reduced, irreversible changes in nature is expected to occur. Considering the urgency and importance of this issue, in 2015 in Paris world leaders signed an agreement on the reduction of CO_2 emissions, with the ultimate goal to keep the global average temperature well below 2° C compared to pre-industrial levels. In order to address this issue effectively, fossil fuels should be replaced by renewable energy resources. In fact, renewable energy resources are vast. For instance, Perez *et al.* [4] reported that Earth receives 23000 Terawatt-year of energy from the Sun. In comparison, annual world energy consumption is only 16 Terawatt-year, thereby ideally global energy demand could be satisfied by solar energy alone. However, this is far from reality. Considering the global electricity market, it is reported that electricity generation by solar Photovoltaic (PV) accounts for only 1.9 % of global electricity production [5]. Nonetheless, the solar PV market is getting momentum. As seen in Figure 1.2, over last ten years global solar PV capacity has increased more than 50 times. More interestingly, last year there

was more Solar PV capacity installed in comparison to any other power generating technologies. Therefore, it is evident that solar PV is getting more attention and becoming more important in the global energy sector [5].

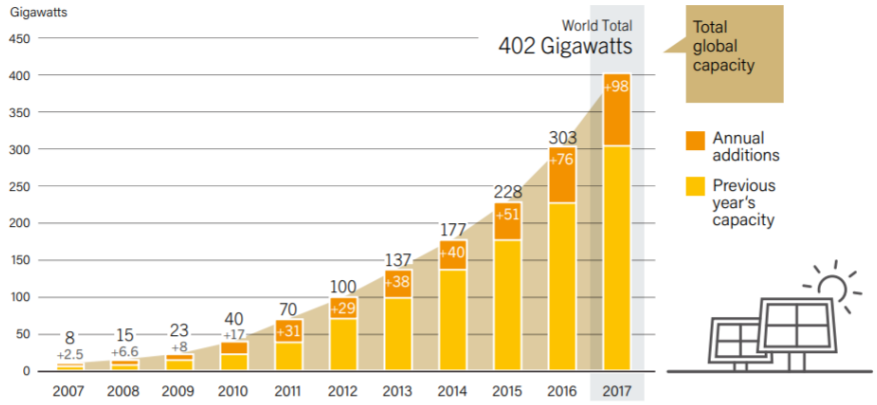

Figure 1.2: Global capacity of installed solar PV. Adopted from [5].

1.1 Solar PV Technologies

Solar PV technologies can be classified into three generations [6]. The first generation solar cells utilize wafer-based mono-crystalline, poly-crystalline silicon semiconductors. These PV technologies are dominating the PV industry and have 95% of global PV market share [7]. Concerning manufacturing process of these solar cells, Czochralski or casting methods are used to grow silicon ingots. In fact, both of these techniques require high-temperature treatments, thereby production of the first generation solar cells is an energy-intensive process. Moreover, production of these cells is not efficient in terms of materials usage since substantial amount of waste is generated when silicon ingots are sliced into wafers. Additionally, first generation solar cells are stiff and rigid, thus cannot be used on flexible substrates. Aforementioned drawbacks have triggered the development of the second generation solar PV technologies, which are based on thin film semiconductors such as CdTe, CIGS, μ-Si:H, a-Si. Unlike the first generation solar cells, these cells can be produced on substrates which are flexible to some extent [8],[9]. Furthermore, production of the second generation solar cells generates less waste. According to Fraunhofer Institute, the market share of these technologies is 5% [7]. Limited market penetration of the second generation solar cells is determined by high price, which is a consequence of two factors. Firstly, high-temperature treatments are not avoided in production, thus the manufacturing process is energy intensive. Secondly, chemical elements used for second generation solar cells are scarce [10]. It has stimulated the development of cheap, aesthetically appealing, versatile third generation solar cells. This group encompasses technologies such as organic PV, dye-sensitized and perovskite solar cells. The latter one was introduced only in 2009, but as demonstrated in Figure 1.3 it already has surpassed the power conversion efficiency (PCE) of 23% [11]. This phenomenal rapid growth has drawn attention and this technology is regarded as one of the most promising PV technology.

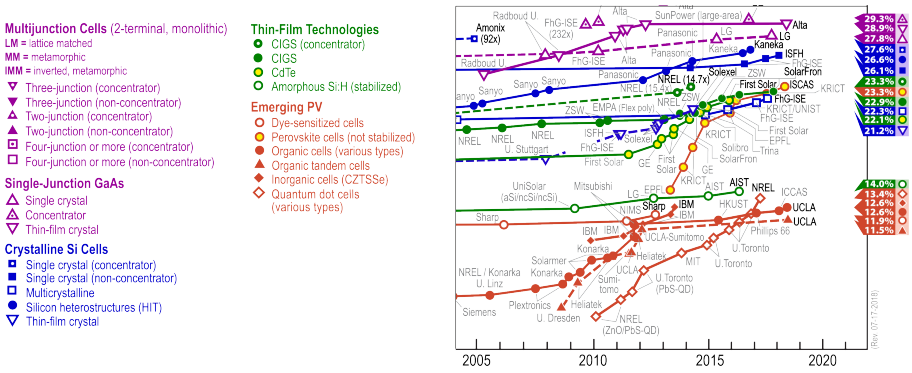

Figure 1.3: Best research-cell efficiencies in 2018. Adopted from [11].

1.2 Perovskite solar cells

Perovskite solar cells (PSC) are based on organo-metal halide perovskite semiconductors such as $CH_3NH_3PbI_3$ or $CH_3NH_3PbBr_3$, which belong to perovskite crystal family that comprises of totally inorganic and hybrid perovskites (see subsection 2.1.1). Due to good optoelectronic features (see subsection 2.1.2) these organo-metal halide perovskites are utilized as photo-active layers in perovskite solar cells. Actually, this technology has a huge potential to challenge conventional solar cells like c-Si, CdTe, GaAs. The main reasons, why perovskite solar cells are promising, are presented below.

- **High efficiency**;

  In less than a decade, the PCE of perovskite solar cells has skyrocketed to 23.3 % level [11], which is comparable with PCEs of existing PV technologies.

- **Easy to process**;

  Production of perovskite solar cells does not require high-temperature treatments since perovskite is solution processed [12], or vapour-deposited [13]. Thus, processing of these solar cells is less energy-intense and more environmentally friendly.

- **Consist of abundant elements**;

  Typically perovskite solar cells contain semiconductors $CH_3NH_3PbI_3$, $CH_3NH_3PbBr_3$, which consist of elements that are more abundant than cadmium, indium and tellurium [10].

- **Versatile**;

  Perovskite solar cells can be manufactured on flexible substrates [14], thereby these cells can be implemented in buildings and complex structures. Aside from that, perovskite solar cells are suited for an industrial roll-to-roll manufacturing process.

Unlike other solar PV technologies, PSCs are classified into planar and mesoscopic. These cells are depicted in Figure 1.4. As it is shown, incoming light is absorbed and charges are generated in the perovskite layer. Subsequently, produced electron and hole drift to opposite directions until they reach charge transport layers, where charges are selectively collected depending on their polarity and then transported to electrodes. As can be seen, in the mesoscopic perovskite solar cells electrons have two alternatives to reach charge transport layer. They can be transported by perovskite itself or by mesoporous scaffold structure. Unlike in mesoscopic solar cells, charges generated in planar solar cells are transported by perovskite itself. Regardless of the architecture perovskite solar cells have hole and electron charge transport layers. Apart from their main role to separate and transport generated charges, these layers also are important for perovskite solar cells environmental stability, which is one of most serious issues along with other challenges such

as scalability, reproducibility and toxicity (see subsection 2.1.4). Currently, scientists are using different approaches to tackle these problems. For instance, by changing the perovskite chemistry [15],[16],[17], modifying perovskite interface with inorganic layers [18],[19] or implementing inorganic charge transport layers [20]. Subsection 2.1.5 provides more information about these strategies. Hitherto, most of the efficient perovskite solar cells are based on organic hole transport materials (Spiro-MeOTAD, PTAA) [21],[22], which are not the best option. Firstly, they are expensive owing to complex multi-step synthesis process [23]. Secondly, Spiro-MeOTAD and PTAA are not environmentally stable because of hygroscopic and acidic nature [20]. Degraded organic hole transport layers are not capable to protect perovskite from moisture or oxygen ingress. Thereby, it leads to overall poor device stability. As an alternative to these materials, metal oxides, having good environmental stability, high transparency and other features that are listed in subsection 2.2.1 can be used.

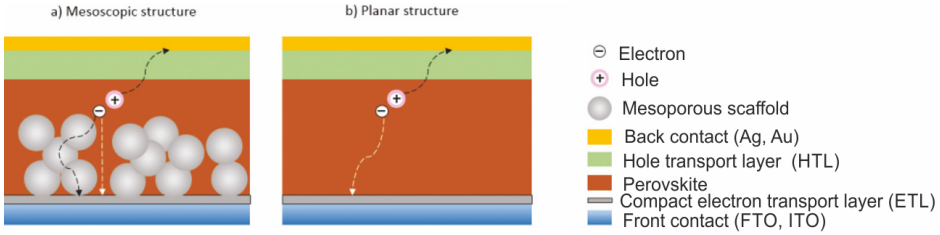

Figure 1.4: Example of perovskite solar cells having a) mesoscopic structure and b) planar structure. Reproduced from [24].

1.3 Nickel Oxide in Perovskite Solar Cells

Nickel oxide (NiO_x) because of its wide band gap and proper valence band position is considered as a good candidate to replace Spiro-MeOTAD or PTAA. It is well documented that perovskite solar cells utilizing solution-processed NiO_x as a hole transport layer can attain PCE above 17% [25], [26]. In order to improve perovskite solar cell performance, several research groups have doped NiO_x films, arguing that doping could improve NiO_x conductivity. In fact, it has been shown that perovskite solar cells having NiO_x doped with Cu or Mg and Li could exhibit PCE above 20% [27],[28]. More interestingly, it has been reported that NiO_x films could be doped intrinsically by post-annealing them in air or oxygen atmosphere [29], [30]. Seo *et al.* [31] has demonstrated that perovskite solar cells having post-annealed atomic layer deposited NiO_x films have better performance than the ones based on pristine NiO_x.

1.4 Project objective and approach

The goal of this thesis is to investigate atomic layer deposited NiO_x as a hole transport layer in inverted planar perovskite solar cells (configuration is described in subsection 2.1.3). Even though atomic layer deposition (ALD) technique is capable to produce highly conformal and uniform films with thickness control at the atomic level (see subsection 3.1.1)), there is only one research group which has published studies about ALD NiO_x for perovskite solar cells [31],[32]. In one of their studies, post-annealing effects on ALD NiO_x and on PSC performance have been investigated. However, there is still lack of knowledge about post-annealing effects. Thereby, this thesis presents a systematic study of post-annealing effects on ALD NiO_x, on the interface of ALD NiO_x/perovskite and its implications for solar cell performance. In order to perform this study three different cases are investigated: pristine, annealed in air at 150°C for 1 hour and annealed

in air at 300°C for 20 minutes. The main research questions being addressed in this thesis are as follows:

- What is the performance of perovskite solar cells utilizing pristine atomic layer deposited nickel oxide?
- How are the bulk/interface material properties of atomic layer deposited nickel oxide affected by post-annealing?
- How is the perovskite solar cell performance affected by NiO_x post-annealing?

1.5 Outline

This thesis is divided into 6 Chapters. Chapter 2 introduces perovskite solar cells, the main challenges that this technology encounters and possible solutions to overcome them. In addition, this chapter provides information about general requirements for hole transport materials. It ends with a section about state of art in perovskite solar cells having NiO_x as a hole transport layer. Descriptions about experimental set-ups and their working principles are provided in Chapter 3. ALD NiO_x process development is presented in Chapter 4. Here, apart from general process description and saturation curves, proposed ALD NiO_x reaction scheme on OH- terminated surface is presented. Chapter 5 is the cornerstone of this thesis. In the first part of this chapter the characterization of pristine ALD NiO_x is presented. In the second part of this chapter study on post-annealing effects on NiO_x properties is presented. Lastly, this chapter is concluded with the analysis of the performance of solar cells having pristine and annealed NiO_x films and the short discussion about possible post-annealing effects. Finally, Chapter 6 presents the conclusions that are drawn from the obtained results and recommendations for future investigations on ALD NiO_x for perovskite solar cells.

Chapter 2

Perovskite Solar Cells: General Aspects, Challenges and Solutions

This chapter is divided into two sections. The first section introduces organo-metal halide perovskite and solar cells which are based on this semiconductor. In addition to that, here main perovskite solar cell drawbacks/challenges and strategies to overcome them are presented. Requirements for hole transport layers are described in the second section. It is followed up with a discussion about possible inorganic materials for hole transport layers. The second section is concluded with an overview of perovskite solar cells having NiO_x as a hole transport layer.

2.1 General Aspects of Organo-Metal Halide Perovskite and Solar Cells

2.1.1 Introduction to Organo-Metal Halide Perovskite

Materials which are crystalline and have chemical formula ABX_3 (A, B are cations and C is anion) are classified as perovskites. The name for these type of crystals is given after Russian mineralogist Lev Perovski. First documented perovskites are calcium titanate ($CaTiO_3$) and barium titanate ($BaTiO_3$). Their existence is known for more than 50 years [33]. In 2009 Kojima *et al.* [34] reported that organo-metal halide perovskites $CH_3NH_3PbI_3$ (MAPI) and $CH_3NH_3PbBr_3$ (MAPBr) can be implemented in mesoscopic solar cells as solar harvesters. The PCE of first solar cells utilizing organo-metal hybrid perovskites was reported to be 3.13 % (MAPBr) and 3.81 % (MAPI). This discovery triggered interest in organo-metal halide perovskites. In less than ten years perovskites solar cells have achieved the PCE of 23.3 % [11] which is comparable with other long existing solar cell technologies. In order to reveal why perovskite solar cells are efficient, the properties of organo-metal halide perovskites are presented in the following subsection.

2.1.2 Properties of Organo-Metal Hybrid Perovskites

This type of perovskites similarly as other perovskites are crystalline, having chemical formula ABX_3. In case of organo-metal halide perovskites A cation is organic methylammonium (MA), $CH_3NH_3^+$; formamidinium (FA), $CH_3(NH_2)_2^+$ [35],[36], B cation is divalent metal Pb^{2+},Sn^{2+} [37], and X is halide anion Cl^-, Br^-, I^- [38],[39]. Perovskite crystalline structure depends on the temperature. For instance, $CH_3NH_3PbI_3$ perovskite at the temperature lower than 163 K is in orthorhombic phase, at temperature range 163 - 327.2 K it is in tetragonal phase and at higher temperatures it attains cubic structure [40]. Figure 2.1 shows the typical cubic structure of perovskite. In case of $CH_3NH_3PbI_3$, the unit cell comprises of iodine octahedra, which contains one lead ion located at the center of each octahedron. Voids between inorganic octahedra are occupied by methylammonium. The size of the organic counterpart is limited by the dimensions of

cavities between inorganic octahedra. In order to have structurally stable cubic perovskite crystal, organic cations should fit in the cavity and not distort it. Scientist Goldschmidt introduced the tolerance factor, which is an indicator for stability and distortion of crystal structures. This factor is calculated by applying the following formula:

$$t_f = \frac{r_A + r_x}{\sqrt{2}(r_B + r_x)} \tag{2.1}$$

where r_A, r_B, r_x are the radius for organic cation, metal and halide, respectively. Tolerance factor of highly stable cubic perovskite crystals cannot exceed unity [41]. Thereby, organic counterparts have to be carefully selected in order to have structurally stable perovskites. Hitherto, mainly perovskites containing MA, which t_f is 0.99 [42], and formamidinium $CH_3(NH_2)_2^+$ (FA), which t_f is 0.91 [42], are extensively studied.

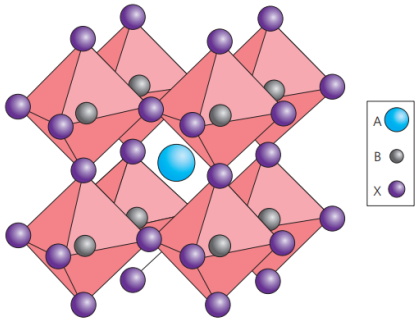

Figure 2.1: Perovskite crystal structure in cubic phase. Adopted from [43].

Investigations on optical features have revealed that $CH_3NH_3PbI_3$ has high optical absorption coefficient with sharp optical absorption edge, which is comparable with GaAs technology [44] (see Figure 2.2), which holds the world record of PCE (28.8%) of research-based single junction solar cells [11]. More importantly, the absorption edge of $CH_3NH_3PbI_3$ can be shifted to a lower wavelength region by incorporating FA ions [45], so that PSCs attain higher J_{SC}. Optical band gap can be also tuned by changing the halide anion composition. For instance, it is reported that perovskites having bromide instead of iodine attain larger optical band gap [46]. Interestingly, perovskite morphology also has an influence on its optical features. For instance, Prasanna *et al.* [47] have reported that band gap of perovskite consisting of contracted cubic unit cells is reduced with respect to undistorted perovskite, whereas perovskites consisting of unit cells, which octahedra are tilted, attain higher band gap with respect to the regular case. Thereby, organo-metal hybrid perovskite semiconductors are suitable for tandem solar cell applications owing to their tunable optical band gap.

Furthermore, organo-metal halide perovskite exhibits ambipolar charge transport [48]. On top of that electron and hole diffusion lengths are comparable and can be up to 1 μm [49]. Thus, perovskite can be implemented in the planar solar cells, which will be described later in this chapter. Additionally, Sum *et al.* [50] revealed that the binding energy of excitons generated in $CH_3NH_3PbI_3$ ranges from 19 meV to 50 meV. At room temperature thermal energy is around 25 meV, thus excitons can be dissociated without any additional energy. All aforementioned things considered, organo-metal halide perovskites have high potential in the field of solar PV.

2.1.3 Planar and Tandem Perovskite Solar Cells

As previously mentioned in subsection 2.1.1 the dawn of the perovskite solar cells started in 2009, when Kojima *et al.* [34] revealed that organo-metal halide perovskites could be used as light absorbers. At that time $CH_3NH_3PbI_3$ and $CH_3NH_3PbI_3$ were implemented in the solar cells having mesoscopic scaffold structure, which resembles to dye-sensitized solar cells (DSSC). Eventually,

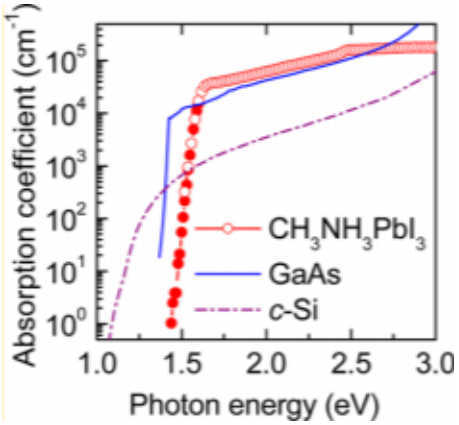

Figure 2.2: Optical absorption coefficients of c-Si, GaAs and $CH_3NH_3PbI_3$ semiconductors. Adopted from [44]

organo-metal halide perovskites were incorporated into solar cells having a planar structure. Unlike mesoscopic solar cells, in planar architecture perovskite is sandwiched between two charge transport layers. Considering the fact that perovskite exhibits ambipolar charge transport, two possible configurations of planar perovskite solar cells are available. Figure 2.3 a) shows classical planar structure. As can be seen, it is n-i-p configuration, where n is an electron transport layer, i is a photoactive layer and p is a hole transport layer. Structure of inverted planar solar cell, having p-i-n configuration is depicted in Figure 2.3 b).

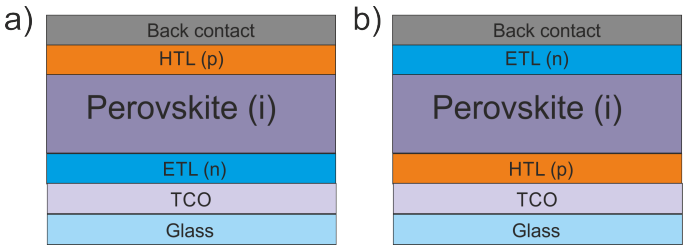

Figure 2.3: Configurations of planar perovskite solar cells. a) n-i-p, classical structure; b) p-i-n, inverted structure. Here p is hole transport layer (HTL), i is photo-active layer (perovskite) and n is electron transport layer (ETL).

Additionally, organo-metal halide perovskites can be implemented in tandem solar cells. Owing to the fact that perovskites have a tunable band gap, tandem solar cells can be based on perovskites having different band gaps. Alternatively, tandem solar cells can be made by combining perovskite with other photo-active materials such as silicon. In fact, recently silicon/perovskite tandem solar cells have achieved power conversion efficiency of 27.3% [51], which is higher than the world record efficiency for single junction silicon solar cells 26.6% [11]. Even though perovskite-based solar cells have succeeded in having comparable power conversion efficiency with conventional photovoltaic technologies, it is a challenge to make perovskite solar cells fully exploitable and commercial due to several factors, which are introduced in the coming subsection.

2.1.4 Challenges in Perovskite Solar Cells

In order to commercialize perovskite solar cells, several criteria have to be fulfilled. Firstly, solar cells have to be reliable and under ambient conditions exhibit stable performance. Secondly, technology has to be easily reproducible and scalable. Lastly, the risk of toxicity has to be minimized to acceptable levels. Actually, all the aforementioned requirements are only partially

met by perovskite solar cells. Each of these aspects is discussed in detail below.

- **Environmental stability**.

  Organo-metal halide perovskites are not rigid under ambient conditions. Due to the presence of organic counterparts perovskite gradually decomposes and loses its optoelectronic features. Moisture, heat and UV light are one of the most aggressive factors inducing perovskite degradation. Each of these elements is briefly discussed below.

  - **Moisture/water stability**. Chun-Ren Ke *et al.* [52] and Li *et al.* [53] have proposed that under exposure to water perovskite decomposes undergoing following chemical reaction:

    $$CH_3NH_3PbI_3 \longrightarrow (-CH_2-) + NH_3(g) + HI(g) + PbI_2. \tag{2.2}$$

    Alternatively, Phillipe *et al.* [54] and Niu *et al.* [55] have suggested that upon reaction with water $CH_3NH_3PbI_3$ decomposes through this chemical reaction:

    $$CH_3NH_3PbI_3 \longrightarrow CH_3NH_3I(aq) + PbI_2. \tag{2.3}$$

    Both proposed chemical reactions imply that organic cation is washed away and PbI_2 is left in the film. Water-induced degradation can be monitored by photoelectron spectroscopy, since PbI_2 rich films are more n-type [56], due to created iodine vacancies, lead interstitials, which act as n-dopants [57].

  - **Thermal stability**. It has been reported that at temperatures above 80-85 °C perovskites start to decompose [58],[59],[60] due to diffusion of volatile organic counterparts. Weak heat tolerance makes the perovskite solar cells manufacturing process challenging. Only low-temperature deposition techniques can be used to produce perovskite solar cells. Concurrently, the operation of perovskite solar cells in hot countries may be problematic.

  - **UV light stability**. Perovskites also suffer from light-induced degradation, especially when exposed to UV light[61]. If perovskite is in contact with metal oxides degradation is more aggressive because under UV light oxygen in oxides is converted into superoxide O_2^-, which easily reacts with organic species [42]. Aristidou *et al.* [62] has proposed that perovskite and superoxide reaction products are water, methylamine and lead iodide.

- **Toxicity**.

  Highest solar cell efficiencies are achieved utilizing organo-metal halide perovskites containing lead. However, it is well known that lead is toxic and its usage is highly regulated. Thereby, toxicity issue for perovskite solar cells is actual. To tackle this problem, lead is replaced by tin. However, till now the PCE of solar cells containing Sn ($\eta \approx 9\%$) [63],[64] are far from Pb based perovskites.

- **Scalability, reproducibility and hysteresis**.

  Currently, the size of perovskite solar cells exhibiting efficiencies above 20% is less than 1 cm^2 [65]. Up-scaling perovskite solar cells is an issue since precise control on perovskite crystal growth, grain size and crystallinity is required [66]. Additionally, it is a challenge to make reproducible perovskite solar cells because perovskite grain boundaries are sensitive to moisture [67]. Apart from challenges in reproducing solar cells, it is well documented that perovskite solar cells relation between current density and voltage (J-V) depends on the scan direction of J-V measurement. Deviations in J-V results complicates perovskite solar cells licensing and benchmarking procedure. Hitherto, there is no explicit explanation why perovskite solar cells exhibit this behaviour, which is called hysteresis. Till now, it has been proposed that the hysteresis phenomenon could be due to the ionic displacement/ion migration [68],[69], trapping of electronic carriers at the perovskite interface [70].

2.1.5 Strategies for Stable Perovskite Solar Cells

In order to tackle the aforementioned perovskite solar cell issues, several strategies are used. Short descriptions of these approaches are described below.

- **Perovskite chemistry**.

  In the previous subsection, it is pointed out that upon exposure to humidity, heat and UV light perovskite decomposes leaving behind PbI_2 rich films. This implies that organic cation is Achilles' heel of perovskite. Thus, one of the possible ways to improve perovskite stability is change or mix organic cations. For instance, organic counterparts in FA based perovskites can be mixed with Cs, having the ionic radius which meets Goldschmidt tolerance factor requirement [71]. Incorporation of Cs helps to achieve better perovskite crystallization due to entropic stabilization. In turn, perovskites containing Cs exhibit better thermal and humidity stability [17], [72]. Moreover, the addition of Rb^+ may also help to improve perovskite stability [16]. Not only monovalent metal ions help to improve perovskite stability but also other inorganic counterparts can do it. For instance, better perovskite stability can be achieved by incorporating ($CH_6N_3^+$) guanidinium (Gua) ions into $CH_3NH_3PbI_3$ perovskites. Jodlowski *et al.* [15] reported that perovskites with the mixture of Gua/MA cations attain better stability than MA-based perovskites. In addition, it has been demonstrated that the performance of perovskite solar cells based on Gua/Ma based perovskites is stable for 1000 hours under continuous light irradiation. Furthermore, better perovskite material stability can be attained by adding salts. For example, Boopathi *et al.* [73] reported that $CH_3NH_3PbI_3$ containing 0.75 % KCl salt have better stability. The enhancement of stability is attributed to better crystallinity and closed films, thus films are more compact and not permeable for oxygen and moisture, which attacks perovskite and triggers degradation.

- **Passivation layers**.

  Improvements in perovskite solar cells stability are also attained by modifying interfaces between perovskite and charge transport layers. For example, solar cells with TiO_2 as an electron transport layer may suffer from UV light exposure due to TiO_2 catalytic features. In order to overcome UV-induced degradation, interface between perovskite and TiO_2 can be modified by incorporating a thin layer of CsCl salt [71]. Other than that, it has been demonstrated that Al_2O_3 layer implementation between perovskite and charge transport layer can improve stability by hampering water-induced degradation [18], [74].

- **Inorganic charge transport layers**.

  Perovskite solar cells stability solely depend on the charge transport layers and its robustness under ambient conditions. Careful selection of charge transport layers may have significant implications on the perovskite solar cells stability. Hitherto, efficient perovskite solar cells are developed utilizing organic hole transport materials such as Spiro-MeOTAD, PTAA [21],[22]. However, due to organic nature both of these materials suffer from poor long-term UV, moisture and thermal stability [20]. Degraded charge transport layers lose their ability to protect perovskite from oxygen, moisture. In literature it has been already demonstrated that SnO_2 help to improve perovskite solar cells moisture stability [75].

2.2 Hole transport layers

In this section requirements for good hole transport layers are introduced. Following that, possible inorganic hole transport layers are discussed and compared with organic ones. Lastly, the case of NiO_x as a hole transport layers is introduced.

2.2.1 Requirements for Hole Transport Layers

In order to have highly efficient perovskite solar cells, hole transport layers should meet several requirements, which are listed below.

- **Specific energy band alignment**.

  The valence band of hole transport layers should be in good alignment with perovskite valence band. In this way, generated holes do not encounter a potential barrier, thus are effectively extracted from the perovskite layer. Another important aspect is the conduction band position. In order to prevent electron flow from perovskite to hole transport material, the conduction band of hole transport layer should deliver a high potential barrier in order to make electrons' quantum transmission coefficient and the probability of sufficient thermal excitation low. Illustration of good hole transport layer in terms of energy band alignment is presented in Figure 2.4 a).

- **High hole mobility**.

  To ensure that holes are extracted and sufficiently transported to the electrode, the mobility of major charge carriers in hole transport materials should be high [20],[76].

- **Lateral electrical continuity**.

  Hole transport layers should be uniform and conformal to ensure that perovskite is not in direct contact with an electrode. Otherwise, photogenerated charges recombine at defective areas, which are shown in the inset of Figure 2.4 b). In addition, the occurrence of pin-holes inside the hole transport layer may lead to a significant drop in shunt resistance due to the formation of shunt pathways. This effect is detrimental to perovskite solar cells performance (see subsection 3.3.2).

- **High optical transmittance**

  In planar perovskite solar cells having p-i-n configuration it is essential that hole transport layer is highly transparent in the broad range of the spectrum, so that majority of photons reach perovskite layer. Thereby, hole transport layers should have a wide optical band gap in order to limit parasitic light absorption.

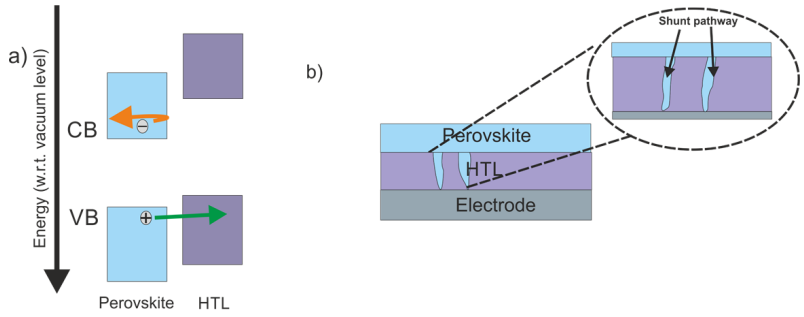

Figure 2.4: a) Schematic representation of desired hole transport layer (HTL) and perovskite energy bands. Holes are extracted from perovskite (green arrow), whereas electrons are prevented from flowing to HTL (orange arrow); b) Illustration of electrode/HTL/perovskite cross-section. In presence of pinholes, photogenerated charges recombine. Additionally, perovskite solar cell shunt resistance drops due to formed shunt pathways (black arrows).

2.2.2 Inorganic Hole Transport Layers

As previously mentioned, Spiro-MeOTAD and PTAA are utilized in the most efficient solar cells. However, these hole transport materials are not an ideal solution for cheap, stable and efficient perovskite solar cells. Firstly, Spiro-MeOTAD and PTAA are costly owing to the multi-step synthesize process [23]. Secondly, organic hole transport layers have poor environmental stability [20]. Thirdly, organic hole transport layers suffer from parasitic absorption, especially when they are doped [77]. These downsides have stimulated the search for inorganic counterparts, which are robust and not prone to degradation [20],[76]. Figure 2.5 demonstrates possible inorganic materials that can be implemented in perovskite solar cells as hole transport layers. As it can be seen, NiO_x is a good candidate for hole transport material. More particularly, because of its wide bandgap NiO_x is promising for applications in planar inverted perovskite solar cells. However, it is not yet validated and confirmed that NiO_x has superior features to improve perovskite solar cells moisture stability. This question remains open for further scientific investigations. Here, only initial perovskite solar cells efficiency is considered. Short discussion about it is presented in the next subsection.

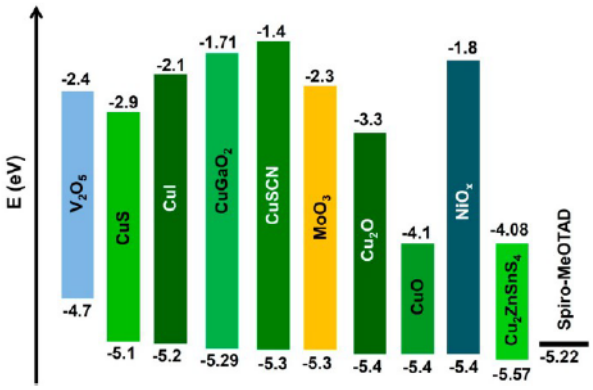

Figure 2.5: Energy level diagram of inorganic hole transport materials along with HOMO level of Spiro-MeOTAD. Adopted from [20].

2.2.3 Nickel Oxide as Hole Transport Layer

NiO_x is most successfully applied in inverted planar perovskite solar cells [20]. Four different cases of NiO_x are discussed in this subsection, according to literature studies:

- **Non-ALD, un-doped NiO_x.**

  Metal oxides can be deposited using various deposition techniques and NiO_x is not an exception. Table 2.1 presents PCEs of inverted planar perovskite solar cells having non-ALD,un-doped, as-deposited NiO_x. As can be seen, PCEs of perovskite solar cells utilizing NiO_x depend on deposition technique. The best PCE of 18.45% is attained by implementing pinhole free, high-quality solution processed NiO_x film [25]. However, PCE of perovskite solars cells based on un-doped NiO_x hardly achieve 20% [20],[76].

- **Non-ALD, doped NiO_x.**

  It is considered that perovskite solar cell efficiency is limited by NiO_x conductivity. In fact, it has been shown that NiO_x conductivity can be improved by doping NiO_x films [81]. Concurrently, it has led to higher solar cell performance. For instance, Yue *et al.* have reported that NiO_x layer doped with 5% Cu leads to more efficient perovskite solar cells. Furthermore, Xie *et al.* [27] have demonstrated that PCE over 20 % (20.65 %) can be

Table 2.1: PCE of inverted planar perovskite solar cells based on un-doped as-deposited NiO_x.

HTL	Deposition method	Perovskite	PCE [%]	Paper
NiO_x	Solution-processed	$MAPbI_3$	17.6	[25]
NiO_x	Electrodeposition	$MAPbI_{3-x}Cl_x$	7.25	[78]
NiO_x	Spray pyrolysis	$MAPbI_3$	13.49	[79]
NiO_x	Magnetron sputter	$MAPbI_3$	11.6	[80].

achieved by implementing NiO_x, which is doped with Li and Mg. Summary of these two aforementioned cases is presented in Table 2.2.

Table 2.2: PCE of inverted planar perovskite solar cells based on doped NiO_x.

HTL	Deposition method	perovskite	PCE [%]	Paper
NiO_x	Spin-coating	$MAPbI_{3-x}Cl_x$	14.47	[28]
NiO_x + 5% Cu	Spin-coating	$MAPbI_{3-x}Cl_x$	20.5	[28]
$Li_{0.05}Mg_{0.15}Ni_{0.8}O$	Spray pyrolysis	$FA_{1-x}MA_xPbI_3$	20.65	[27]

- **Non-ALD, un-doped, post-treated NiO_x.**

  More interestingly, it has been reported that PCE of perovskite solar cells based on un-doped NiO_x can be boosted by applying UV-ozone or annealing post-treatments. In the case of former, it has been demonstrated that ionization potential of UV-ozone treated NiO_x films increases [82],[83],[84]. Thereby, NiO_x valence band level can be tuned to attain desired band alingment between perovskite and NiO_x valence bands. Additionally, it has been reported that UV-ozone post-treated NiO_x films are more hydrophilic [82], thus perovskite spreads better on these films. As a consequence, deposited perovskite layer contains fewer pin-holes and forms a stable interface with NiO_x layer [84]. Results of studies reporting solar cell performance parameters with respect to UV-ozone post-treatment are presented in Table 2.3.

Table 2.3: Performance parameters of perovskite solar cells containing as-deposited or UV-ozone treated NiO_x.

HTL	Deposition method	Post-treatment	V_{OC} (V)	J_{SC} (mA cm^{-2})	FF (%)	PCE (%)	Paper
NiO_x	Solution-processed	As-deposited	0.72	10.71	59	4.6	[82]
	Solution-processed	UV-ozone	0.88	13.53	58	6.9	
NiO_x	Solution-processed	As-deposited	1.04	16.73	68.4	12.00	[84]
	Solution-processed	UV-ozone	1.03	20.66	74.2	15.9	
NiO_x	Solution-processed	As-deposited	0.84	11.8	45	4.4	[83]
	Solution-processed	UV-ozone	0.95	13.1	45	5.9	

Another way to boost perovskite solar cell efficiency is to post-anneal NiO_x films in air. Referring to literature, it is well documented that hole concentration in NiO_x increases upon post-annealing [29],[85]. Table 2.4 shows that post-annealed NiO_x films implemented in perovskite solar cells result in more efficient devices. Increase in power conversion efficiency is mainly attributed to higher fill factor (FF) and short-circuit current density J_{SC}. This observation suggests that post-annealed NiO_x films may have enhanced conductivity and/or more stable interface, which suppress charge recombination at the conjunction between NiO_x and perovskite.

Table 2.4: Performance parameters of perovskite solar cells containing as-deposited or post-annealed NiO_x.

HTL	Annealing temperature (°C)	Deposition method	Annealing atmosphere	V_{OC} (V)	J_{SC} (mA cm^{-2})	FF (%)	PCE (%)	Paper
NiO_x	As-deposited	Pulsed layer deposition	Air	0.96	11.39	48.6	5.38	[85]
	450	Pulsed layer deposition	Air	1.01	19.86	62.78	12.59	
NiO_x	As-deposited	Solution-processed	Air	1.02	3.55	24.3	0.88	[86]
	300	Solution-processed	Air	1.09	20.2	76.9	16.68	

- **ALD NiO_x films**. ALD material processing technique has huge advantage compared to other techniques. Here, deposited film thickness can be controlled at Ångstrom level. In case of window layers in the perovskite solar cells, thickness control is crucial aspect owing to direct relation between window layer thickness and parasitic light absorption. In comparison, the thickness of ALD NiO_x films implemented in the perovskite solar cells varies from 5 to 10 nm [31],[32], whereas in other cases film thickness are 20 - 100 nm [25],[78].

  ALD NiO_x have shown potential in application for polymer solar cells [87],[88]. However, the literature about perovskite solar cells based on ALD NiO_x is scarce. Until now, only one research group has published studies about ALD NiO_x films in perovskite solar cells. The first publication was released in 2016. Here, Seo *et al.* [31] reported that perovskite solar cells based on pristine ALD NiO_x could attain PCE of 11.82 %. In a similar study, it was revealed that post-annealing ALD NiO_x led to more efficient perovskite solar cells. As shown in Table 2.5 solar cells attained higher PCE due to increase in J_{SC} and FF values. Two years after first publication same research group published a paper reporting that solar cells based on pristine ALD NiO_x could attain *PCE* up to 18.45 % [32].

Table 2.5: Performance parametersof inverted planar perovskite solar cells based on ALD NiO_x.

Post-treatment	Architecture	V_{OC} (V)	J_{SC} (mA cm^{-2})	FF (%)	PCE(%)	Year	Paper
None	ITO/ALD-NiO_x/$MAPbI_3$/PCBM/Ag	1.02	18.94	61	11.82	2016	[31]
Annealed at 300°Cin air	ITO/ALD-NiO_x/$MAPbI_3$/PCBM/Ag	1.04	21.87	72	16.4	2016	[31]
None	FTO/ALD-NiO_x/$Cs_{0.05}MA_{0.95}PbI_3$/PCBM/ BCP/ALD-AZO/Ag	1.047	22.56	78.1	18.45	2018	[32]

In conclusion, ALD is a promising technique to deliver high-quality NiO_x films, which result in efficient perovskite solar cells. From the literature, it is known that post-annealed ALD NiO_x helps to improve solar cell performance. However, post-annealing effects on ALD NiO_x are not well described in the literature. Thereby, this thesis delivers a systematic study of post-annealing effects on ALD NiO_x interface and its relation with perovskite solar cell performance.

Chapter 3

Experimental Setup

This chapter describes experimental set-ups and analytical techniques used for material characterization. It is divided into three sections. The first introduces ALD deposition system and the basic principle of ALD reactions. The second section describes thin film characterization techniques and principles of data interpretation. The last section presents characterization techniques of the perovskite solar cells.

3.1 Atomic Layer Deposition

3.1.1 Principles of Atomic Layer Deposition

Atomic layer deposition (ALD) is vacuum vapour phase deposition technique, which is extensively used for fabricating ultra-thin layers of materials such as metal oxides [89],[90]. ALD comprises cyclic reactions, which consist of two half-cycles (see Figure 3.1).

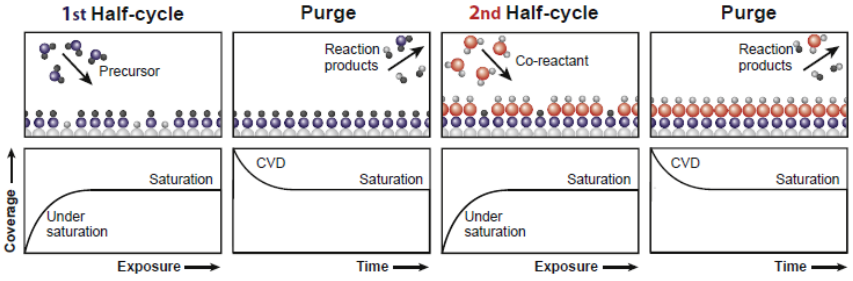

Figure 3.1: Representation of the AB ALD cycle. The first half cycle is denoted as A, whereas second as B. Adopted from [91].

In the first half cycle precursor is injected into the ALD reaction chamber. Then precursor starts to adsorb on the substrate and this process continues till all reactive substrate sites are covered. Simultaneously precursor losses ligand or ligands, which are reaction by-products. These compounds together with residual precursor can eventually trigger chemical vapour deposition (CVD) reactions, which are not desired. Thus, reaction by-products and remaining precursor are purged away from the reaction chamber. Purging time needs to be long enough in order to ensure that residual precursor and reaction by products are removed sufficiently, to prevent any possibility of CVD reactions. The second half cycle starts with a co-reactant step. Similarly, as in the first half-cycle, the residence time of co-reactant has to be long enough to ensure that all accessible surface sites have reacted with co-reactant. After saturation is achieved, all reaction products and remaining co-reactant are purged away for sufficient time to avoid CVD reactions. This step completes one ALD cycle. Ideally, each cycle produces a monolayer of deposited material. The

thickness of deposited films can be controlled at the Ångstrom level by changing the number of ALD cycles. Moreover, utilizing ALD, highly uniform films can be produced. This is primarily determined by the fact that ALD reactions are self-limiting.

3.1.2 Atomic Layer Deposition system

In this work, ALD NiO_x process is developed in a home-built ALD-1 reactor, which is schematically presented in the Figure 3.2.

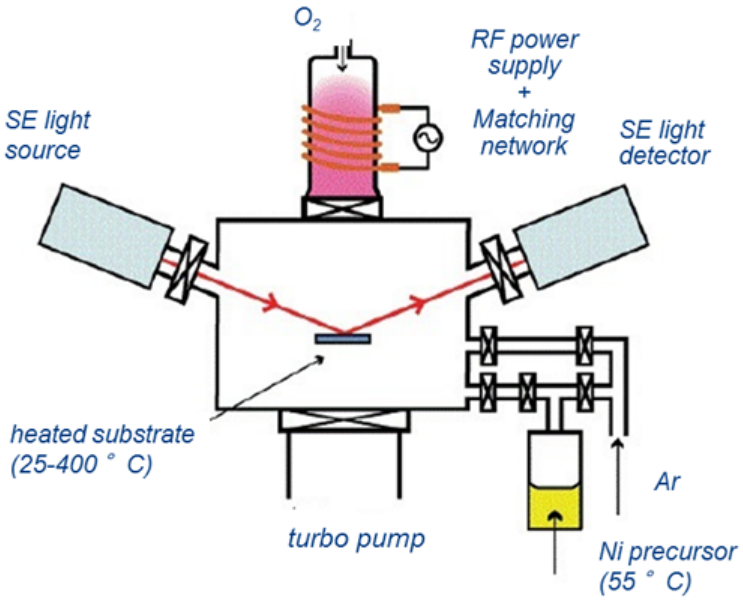

Figure 3.2: Scheme of home-built ALD-1 reactor.

The reactor is equipped with a table, which can be heated up to a predefined temperature in the range of 25-400 °C. Since ALD is a vacuum technique, the pressure in the reactor chamber is controlled by the turbo pump. To run ALD reactions precursor needs to be in a gaseous state, therefore depending on the precursor, the bubbler is heated up to a temperature at which the precursor is volatile. For instance, in the case of nickel-bis(methylcyclopentadienyl) [$Ni(MeCp)_2$] precursor, the bubbler is heated up to 55 °C (see figure 3.2). Argon gas flow transports precursor from bubbler to the ALD chamber, via tubes, which are also heated up to prevent condensation inside the tubes. Similar conditions are applied to the exhaust lines.

ALD-1 reactor can be used for plasma-enhanced ALD processes because this reactor is equipped with an inductively coupled plasma source. To attain plasma, chamber of inductively coupled plasma source is filled with particular gas, which subsequently is ignited and converted to plasma. Different plasma chemistries can be obtained by simply changing the gas inlet to the chamber of the inductively coupled plasma source. In ALD-1 case, inlets of O_2, N_2,H_2 can be used. The plasma power is controlled remotely by controlling alternating current power applied to a cylindrical copper wire which is wrapped around a quartz tube. Moreover, the ALD reactor can be equipped with an in-situ spectroscopic ellipsometer to measure thickness and optical constants of the film.

3.2 Analytical Techniques

In this section, the characterization tools applied to analyse the ALD films are presented. Spectroscopic Ellipsometry (SE) is used to determine the thickness of deposited films. Layer morphology

is investigated using X-ray diffraction (XRD) technique, which provides information about material structure (crystalline or amorphous), crystallite size. The extensive part of this section is devoted to the theory and data analysis of Photoelectron Spectroscopy (PES) technique, which is utilized to probe chemical environment and to measure energy levels (valence band, work function and ionization potential) of deposited layers. To further investigate ionization potential Air Photoemission Spectroscopy (APS) is employed. The surface wettability is analysed by performing contact angle measurements. Optical properties of the investigated films are determined by Ultraviolet-Visible-Near Infrared (UV-VIS-NIR) spectroscopy. Lastly, scanning and transmission electron microscopy techniques are employed to investigate solar cell stack, NiO_x/perovskite interface and conformality of deposited NiO_x layer.

3.2.1 Spectroscopic Ellipsometry

Spectroscopic ellipsometry measures the change in the light polarization between the incident and reflected light. Using spectroscopic ellipsometry (SE) characterization technique optical band gap, refractive index n, extinction coefficient k and layer thickness of analysed samples can be determined. This characterization technique is non-destructive, thereby, is widely applied in thin film analysis for both in-situ and ex-situ studies.

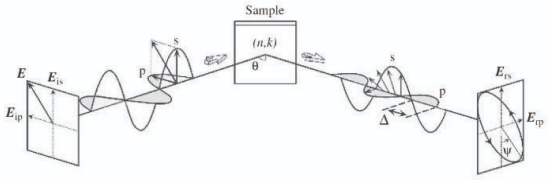

Figure 3.3: Linearly polarized light is generated by the light source. The reflected light is not any more linearly polarized. The change in phase Δ and light intensity Ψ is measured by the detector.

The working principle of spectroscopic SE is based on the light phenomenon to change its polarization after reflection. In SE case, the incident light is linearly polarised, thus there is no phase difference Δ between s (oscillating perpendicular to the plane of incidence) and p (oscillating parallel to the plane of incidence) electromagnetic wave components (see Figure 3.3). After reflection from the substrate, light polarization is converted from linear to elliptical, meaning that s and p components are oscillating at different phases. By measuring the Δ and the amplitude ratio Ψ of reflected p and s components, the complex reflectance ratio ρ is obtained

$$\rho = \tan(\Psi)e^{i\Delta}. \tag{3.1}$$

In order to determine the film thickness and all the aforementioned optical properties, experimental results are simulated utilizing mathematical dispersion models. In this work, SE is used only for determining film thickness. For this reason, experimental SE results are simulated by Cauchy dispersion model. This mathematical model is based on consideration that in the region $E_g < E$ material is highly transparent and absorbance is negligible.

3.2.2 X-ray Diffraction

The principle scheme of X-ray diffraction (XRD) spectrometer is presented in Figure 3.4. As it can be seen, it consists of X-ray tube, collimators, which focus X-ray beam to sample, sample holder and detector. X-Ray tube generates beam of X-ray photons which are collimated and then directed to the sample at the given angle θ. Subsequently, incident X-rays diffract from specimen and are collected at detector.

In crystalline films, which consist of crystal planes orientated in preferential directions, X-rays are scattered in a specific order, whereas amorphous films scatter X-ray beams randomly. In the

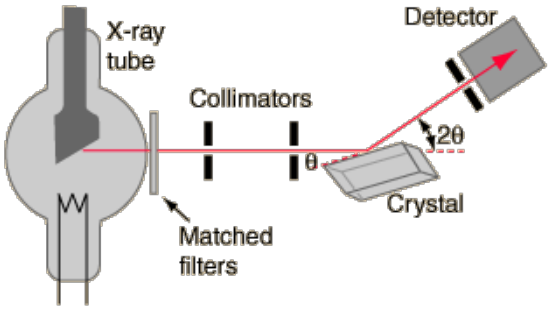

Figure 3.4: Principal scheme of XRD spectrometer.

case of former, at some angles diffracted X-rays (see figure 3.5) are coherent, thus electromagnetic waves interfere constructively. This phenomenon is described by the Bragg's law

$$2d \sin\theta = n\lambda, \tag{3.2}$$

where d is the distance between crystal planes, λ is the wavelength of X-rays and n is an integer.

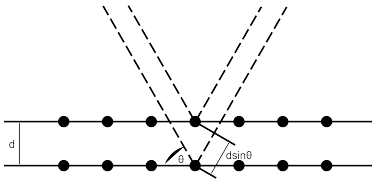

Figure 3.5: X-ray diffraction between two crystal planes.

By changing the angle between the detector and incident X-ray beam (2θ), the XRD diffractogram is recorded. The peak position in XRD spectrum represents the angle at which X-ray interference maximum is achieved. Then from equation 3.2 inter-planar distance d can be found. Furthermore, if the lattice parameter a of the investigated crystal is known, the direction of crystal planes, which are present in the specimen, can be determined. In case of cubic crystals, the relation between lattice parameter and crystal planes is as follows

$$\frac{1}{d^2} = \frac{h^2 + k^2 + l^2}{a^2}. \tag{3.3}$$

There h, k and l are Miller indices and a is unit cell constant. Consequently, the set of hkl indices provide information about crystal plane direction.

Additionally, to measure thin films, the incidence X-ray angle should be very small and close to the critical angle. In turn, X-ray penetration depth is limited, so that, substrate effects are negligible. Sometimes this type of spectroscopy is called grazing-incidence X-ray diffraction(GIXRD). Nonetheless, the working principle of GIXRD is similar to XRD.

3.2.3 Fundamentals of Photoelectron Spectroscopy

Photoelectron spectroscopy (PES) is based on the photoelectric effect. Applying PES the information about occupied states - core level electrons and valence electrons is obtained. The kinetic energy E_k of electrons emitted from the sample is the main source of information that is collected during PES measurements. Using relation (3.4), the electron binding energy E_b, which is defined as the energy difference between Fermi and probed energy levels, and work function Φ, which is the energy difference between vacuum and Fermi levels, can be found. It follows that electrons with the highest kinetic energy have the weakest binding energy and are closest to the Fermi level.

$$h\nu = E_k + E_b + \Phi \tag{3.4}$$

Table 3.1: Silicon case. It is considered that silicon crystal structure is face-centered diamond-cubic, the lattice constant is 0.543 nm, m_n^*=1.08m_0, m_p^*=0.56m_0 [92].

Material	T, K	Eg, eV	ni ,cm^{-3}	n, cm^{-3}
Silicon	300	1.11	$8.3 * 10^9$	$2 * 10^{23}$
Silicon	500	1.11	$9.507 * 10^{13}$	$2 * 10^{23}$

It may be argued that information about the electrons which are in the conduction band can also be extracted from PES results. However, it is very hard to obtain sufficient information about conduction by means of PES. This can be simply explained by comparing intrinsic carrier concentration n_i with electron concentration in the valence band n. The intrinsic carrier concentration n_i described by Fermi-Dirac distribution and effective density of states. The mathematical expression of n_i is presented below

$$n_i = \sqrt{N_c N_v} \exp\left(- \frac{E_g}{kT} \right) \tag{3.5}$$

,there E_g - energy band gap,$N_{c,(v)}$ - effective electron (hole) density of states in conduction (valence) band, k - Boltzmann constant, T - absolute temperature. Alternatively, the density of valence electrons n depends on the atom density n_{at} and the number of electrons in the valence levels k_e. Applying mathematical formula (3.6) the density of valence electrons can be calculated.

$$n = n_{at} k_e \tag{3.6}$$

The comparison of intrinsic carrier and valence band electron concentration for silicon case at room temperature and 500 K is presented in Table 3.1. It is seen that $n >> n_i$, therefore the contribution of photoelectrons populated in the conduction band is negligible. Even if semiconductors are doped the contribution from free carriers is small.

3.2.4 Photoelectron Spectroscopy Set-Up and Probing Depth

The scheme of a typical PES spectrometer is presented in figure 3.6. The main components of the spectrometer are photon source, electrostatic transfer lens, analyser, detector. Noteworthy to mention, that whole set up is in the ultra-high vacuum in order to avoid electron collisions and to ensure that the kinetic energy of electrons is not lost. Depending on the photon source (see Table 3.2) the PES is classified into X-ray Photoelectron Spectroscopy (XPS) and Ultraviolet Photoelectron Spectroscopy (UPS).

Table 3.2: Commonly used photon sources for PES.

Radiation source	Photon energy, eV	Class
Mg-K	1253.6	XPS
Al-K	1486.6	XPS
He I	21.22	UPS

In order to filter out electrons selectively by their kinetic energy, the analyser is hemispherical and is subjected to the electrostatic field, which is generated by applying a potential difference between opposite analyser walls. In this manner only electrons moving at particular speed travel in defined hemispherical trajectory, while others collide to the wall. Subsequently, electrons are collected at the detector and then analysed

.

Using PES only surface layers of an investigated specimen can be analysed. This restriction comes from the fact that excited electrons easily lose their kinetic energy due to inelastic scattering.

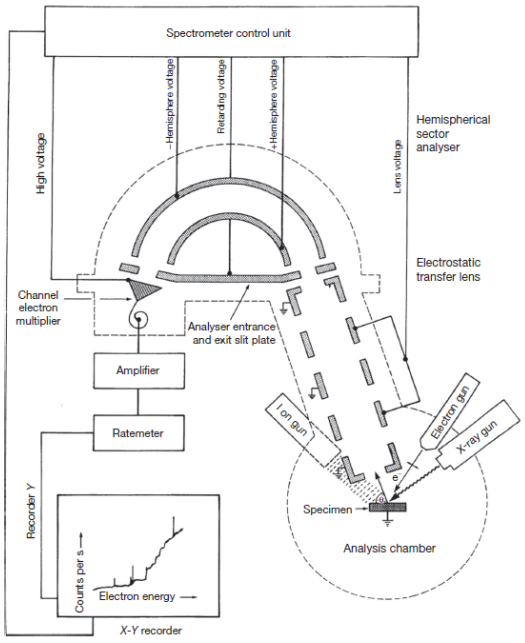

Figure 3.6: Schematic of a typical XPS spectrometer [93].

The distance at which the initial kinetic energy of excited an electron is reduced by the factor of mathematical constant e is called inelastic mean-free path (IMFP), which is denoted as λ. This parameter depends on the initial kinetic energy of an electron and on the composition of the material. In Figure 3.7 it is seen that more energetic electrons have longer inelastic mean-free paths.

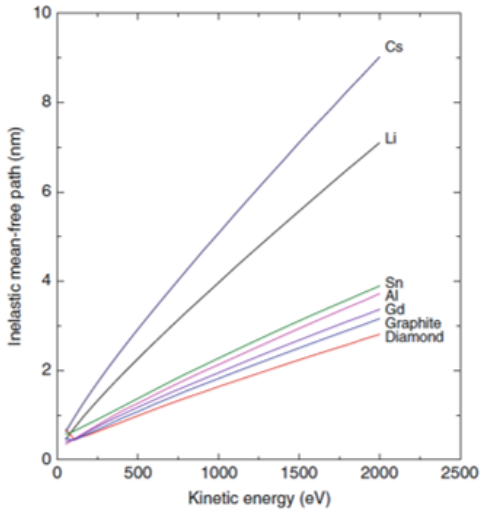

Figure 3.7: IMFP vs Kinetic energy [94].

From inelastic mean free path concept it follows that the photoelectron current is described by Beer-Lambert law:

$$I_s = I_0 \exp(-d/\lambda \sin\theta), \tag{3.7}$$

there I_s is a flux of electrons, which reach a surface and are detected, I_0 is an intensity of electrons,

which are excited at a depth d, λ is an inelastic mean-free path, θ is an electrons detection angle with respect to the substrate plane. Generally, it is assumed that PES sampling depth is $3\lambda \sin\theta$, so that only 5% of electrons emitted at the $3\lambda \sin\theta$ distance from the surface could leave the sample and potentially reach the detector. Actually, sampling depth can be controlled and there are two ways of doing it. The first method is to change the angle between the detector and the surface plane. By increasing angle θ the probing depth gets longer. The example of such measurements are presented in Figure 3.8 a). Considering the working principle of this specific PES case, this method is called angle-resolved photoelectron spectroscopy (ARPES).

The second way to control probing depth is by changing the energy of incident photons. More energetic photons excite electrons, which have higher kinetic energy. In turn, the inelastic mean free path of these electrons is longer (refer to Figure 3.7). In Figure 3.8 b) the schematic representation of sampling depths in XPS and UPS case is given.

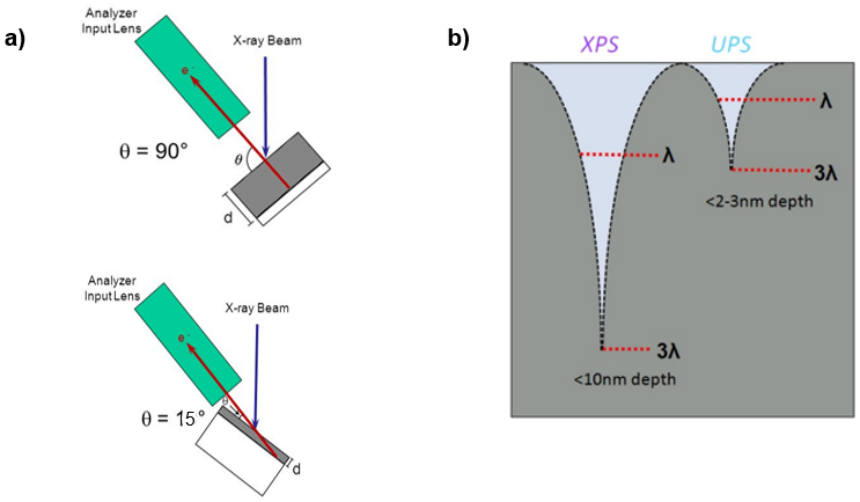

Figure 3.8: a) Representation of ARPES case, here probing depth is denoted as d. b) Scheme of sampling depths attained by XPS and UPS. Adopted from [95].

3.2.5 Peaks and Data Analysis of XPS Spectrum

The XPS spectrum is formed by the primary and secondary electrons. The former have resonant kinetic energy distribution, while the latter form dispersed energy spectrum owing to inelastic scattering events. Due to a closely interacting electron system, primary electrons are further separated into photoemission, Auger and satellite electrons. The processes leading to the formation of the aforementioned electrons are schematically shown in the Figure 3.9. In the following paragraph, only a brief discussion about photoemission electrons is presented.

Since photoemission electrons are primary electrons they do not lose their initial energy, thus form a resonant energy spectrum with unique peak distribution. The position of the peak is determined by the electron binding energy, which is an intrinsic electron feature depending on the atomic orbital and on the material nuclei. For example, from table 3.3 it is seen that the difference between binding energies of carbon 1s,2s and silicon 1s,2s electrons is significant. Therefore, by monitoring photoemission peak position, the information about the elemental composition of the specimen can be retrieved. To make a comparative analysis, XPS spectra is corrected by defining that adventitious carbon peak position is at 284.8 eV.

Additionally, when XPS spectrum contains broad photoemission peaks they can be deconvoluted into individual Gaussian peaks, which are defined by two parameters: binding energy and full width at half maximum (FWHM). The increase of FWHM parameter suggests that the scanned

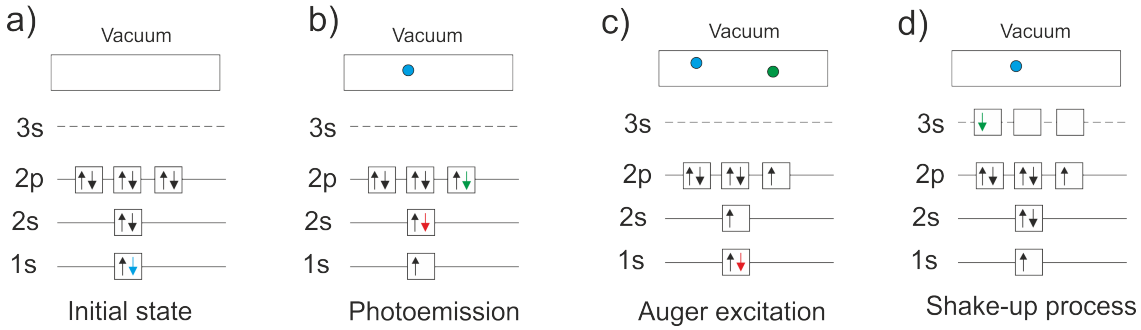

Figure 3.9: Overview of possible events. In a) ground state of atom is presented. After photoexcitation the atom is ionized and 1s electron (blue arrow) is emitted b). The created vacancy then can be filled by electron (red arrow) from 2s energy level and then electron (green arrow) from 2p level is ejected to vacuum level c). In shake-up process, electron ejected from 1s energy level excites electron from 2p to 3s.

Table 3.3: Binding energies of carbon and silicon [96]

IV A group	1s electron binding energy, eV	2s electron binding energy, eV
C	284.4	18.1
Si	1839.4	150.7

element changes its bonding state with neighbouring elements and that chemical environment is changed. The shift of peak position also indicates that chemical environment is changed. More specifically, if the probed element is less electronegative than environment it donates valence electrons. In turn, the withdrawal of the valence electron weakens the screening effect which leads to an increase in binding energy. Conversely, if the analysed element is more electronegative than surrounding atoms the binding energies are reduced. This effect is called the chemical shift (see Figure 3.10).

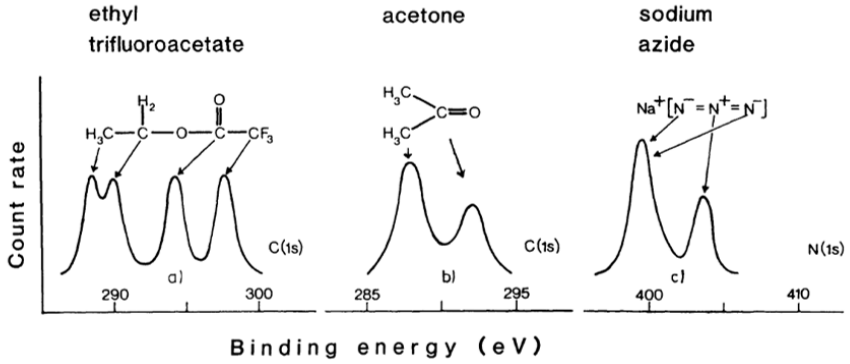

Figure 3.10: The chemical shift of carbon in ethyl trifluoroacetate a). Electronegativity of fluorine is 3.98, of oxygen is 3.44, of carbon is 2.55 and of hydrogen is 2.2 [97]. It is seen that electrons of carbon bonded with fluorine have highest binding energy, whereas carbon bonded with hydrogen has electrons with lowest binding energy. The same trend is seen in acetone b). The example of case when the chemical environment do not changing is prestented in c). Negative sodium atoms attain electrons and it result in lower binding energies, while in case of sodium cations it is vice versa. Adopted from [98].

In some cases, doublet photoemission peaks are observed. It can be explained by quantum mechanics and electrodynamics. From quantum mechanics, it is known that electrons have a spin, whereas from electrodynamics it is well known that moving charges generate a magnetic field. Since electrons are moving charged particle and have an intrinsic magnetic moment, electron energy levels are split into a more finite structure. To further explain how energy levels are split, a brief explanation with equations is provided below. Since an electron has spin, the induced electron magnetic moment is expressed as follows:

$$\mu_{\mathbf{s}} = -2\frac{e}{2m_0}\mathbf{s} \tag{3.8}$$

, there $\mathbf{s}$ is electron spin, m_0 is electron mass. At the same time, the external magnetic field is generated inside the atom. Using Biot-Savart law the magnetic field acting on an electron inside the atom is expressed as follows:

$$\mathbf{B} = \frac{Ze\mu_0}{4\pi r^3 m_0}\mathbf{l} \tag{3.9}$$

, there Z is an atomic number, μ_0 is vacuum permeability and $\mathbf{l}$ is angular momentum. The dot product of electron spin magnetic moment and the magnetic field is equal to potential energy V_B:

$$V_B = (\mathbf{B} * \mu_{\mathbf{s}}) \propto \mid \mathbf{s} \mid * \mid \mathbf{l} \mid \cos\alpha. \tag{3.10}$$

Since electrons have spin up or down there are only two possible angles α between vectors $\mathbf{s}$ and $\mathbf{l}$. Thus energy levels of electrons can be split in two additional states and as consequence doublets in XPS spectra are apparent. However, not all electrons form doublets. For instance, the angular momentum quantum number of electrons in s atomic orbitals is zero, which means that s electrons do not form doublet peaks.

3.2.6 Calibration and Data Analysis of UPS Spectrum

The UPS spectrum comprises of primary and secondary electrons. The latter ones are excited to the vacuum level and emitted from the sample without any interactions. Thereby, the contribution of primary electrons forms a peak structure which represents the density-of-states function of the valence band. The kinetic energy of primary electrons can be found by Einstein relation (3.4). In contrast to primary electrons, secondary electrons are scattered before leaving sample. Because of complex and multiple scattering events, information about kinetic energy is lost. Thus, secondary electrons form a sloping background spectrum with a cut-off region. This spectral part is formed by the slowest secondary electrons, which virtually have no kinetic energy when emitted to the vacuum level. In order to detect these electrons, a bias voltage is applied between the sample and the detectors. The relation between corrected (with applied bias) and not corrected kinetic energies is presented below:

$$E_{kin}^{[obs]} = E_{kin}^{[out]} + e(\phi_s - \phi_d) + e|V_b| + c. \tag{3.11}$$

There $E^{[obs]}$ is kinetic energy after bias is applied, $E^{[out]}$ is kinetic energy before application of bias, V_b is applied voltage, which in this study is 6 eV, ϕ_s is sample work function, ϕ_d is work function of detectors and c is instrumental correction factor, which is 0.273 eV. The latter two terms are detector dependent and in order to take them into account UPS spectrometer is calibrated with respect to the Fermi level, considering that Fermi level is constant in the whole system. Usually, this calibration step is done by measuring the UPS spectrum of metals, which have sharp and defined Fermi edges. The on-set of the attained spectrum is fitted with a Fermi-Dirac function which defines the position of the Fermi level.

The typical UPS spectrum is presented in the figure 3.11. As it can be seen, the spectrum has on-set and cut-off edges. The former one is formed by the electrons, which have the weakest binding

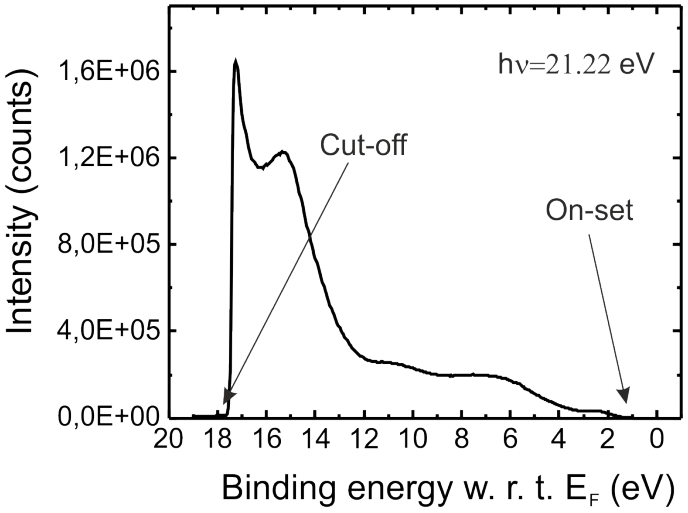

Figure 3.11: Typical UPS spectrum.

energy (valence band maximum). The cut-off or secondary electron edge provide information about slowest secondary electrons.

For solid samples, the on-set and cut-off energies are found by extrapolating the tangent through the point of inflection of the leading edges of the UPS spectrum to the background level. In order to obtain the point of inflection and tangent through this point, three different methods can be used. The first is Gaussian extrapolation, which is based on the consideration that the valence band density-of-states (DOS) distribution can be approximated by Gaussian. Thus, the on-set and cut-off energies are determined by the intersection point between the background signal and tangent drawn through the inflection point of a Gaussian curve. The second widely used method is linear extrapolation. Employing this technique, UPS spectra edges are extrapolated by linear curves. It is the most straight-forward method to carry out UPS analysis. However, this technique can easily lead to the erroneous results (see Figure 3.12) because of the difficulty to visually define the region which should be extrapolated. Using the third extrapolation technique the leading edges of the UPS spectrum are approximated by fitting third order polynomial. After that, the inflection point of the fitted curve is found and then the tangent is drawn through this point. Consequently, the cut-off and on-set energies are determined by the intersection point between the tangent and background lines. This technique is considered to be most reliable since no prior assumptions are made.

Once cut-off and on-set energies are found the work function and ionization potential, which can be seen in the energy band diagram presented in the Figure 3.13, can be calculated using formulas 3.12.

$$\begin{cases} IE = h\nu - (E_{cut-off} - E_{on-set}) \\ WF = h\nu - (E_{cut-off} - E_{Fermi}) \end{cases} \tag{3.12}$$

In metals E_{on-set} and E_{Fermi} are at the same level, therefore the ionization potential and work function are equal. In semiconductors E_{on-set} and E_{Fermi} are at different levels, thus the ionization potential and work function are not matching. The difference between these energy levels (see Figure 3.13) provides information about the position of valence band maximum (VBM) with respect to Fermi level. Noteworthy to mention that the VBM of materials can be measured both by UPS and XPS but the values may differ due to different probing depths and resolution of measurements.

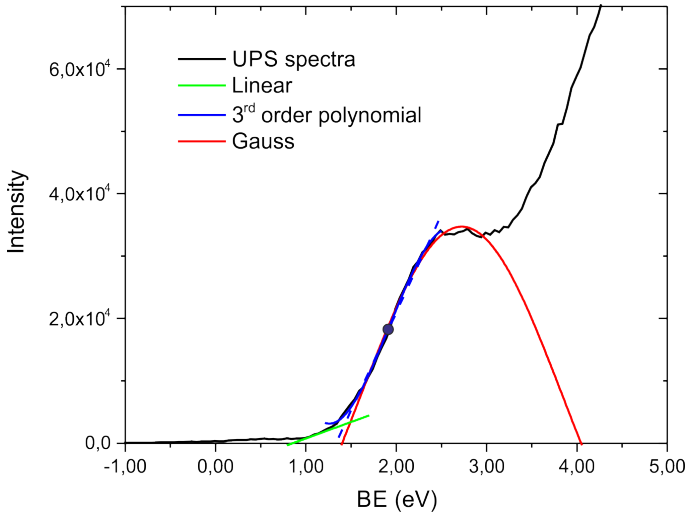

Figure 3.12: Example of different extrapolation techniques. The black dot represents the inflection point of 3rd order polynomial fitted in the edge region. The dashed blue line is a tangent drawn using 3rd order polynomial.

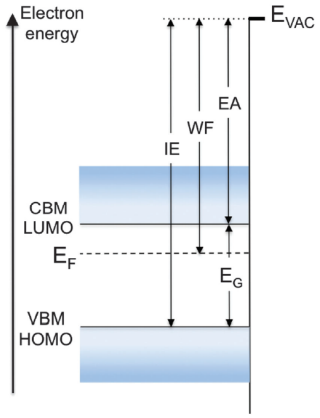

Figure 3.13: Energy band diagram of semiconductor. IE ionization potential, WF work function, E_g band gap, E_{ea} electron affinity. Adopted from [99].

3.2.7 Air Photoemission Spectroscopy

The ionization potential of semiconductors can also be determined by air photoemission spectroscopy (APS). The set-up of this type of spectrometer is shown in figure 3.14. As it is seen, APS set up is divided into two blocks. Block A consists of a spectrometer and photon source. This block is filled with N_2 in order to avoid UV-induced ozone generation. Block B comprises of Kelvin probe and sample stage, which are in air under ambient pressure. These blocks are connected by optical cables.

The working principle of air photoemission spectroscopy can be divided into four steps, which are presented below.

1. A sample is irradiated by photons (3.0-7.0 eV), which are generated by deep ultraviolet (DUV) lamp and sent through optical fiber directly to sample.

2. Ejected photoelectrons form a cloud close to sample because under ambient pressure the inelastic mean free path of electrons is in the range of 1-3 μm. Information about electron

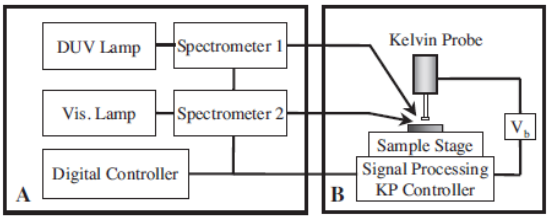

Figure 3.14: The principal scheme of APS set-up. Block A represents spectrometer and optical set up arrangement. Block B consists of sample stage and Kelvin Probe. Adopted from [100].

kinetic energy is lost as they inelastically collide with N_2 and O_2 molecules. However, some electrons stick to the molecules and negative ions are generated.

3. Negative ions are collected at the positively charged Kelvin probe tip.

4. Ion current is recorded as a function of incident photon energy.

From recorded ion current graph the ionization potential of the investigated sample can be obtained by applying Fowler's theory [101]. According to it, the relation between ion photocurrent and incident photon energy is expressed as follows

$$R^{1/3} = k(E_{ph} - h\nu_0) \tag{3.13}$$

, there R is photocurrent, E_{ph} is photon energy and $h\nu_0$ is ionization potential of semiconductor. It follows that ionization energy of semiconductor is determined from the intersection point between linear extrapolation of $R^{1/3}$ and x axis. The example of APS data analysis is presented in the Figure 3.15.

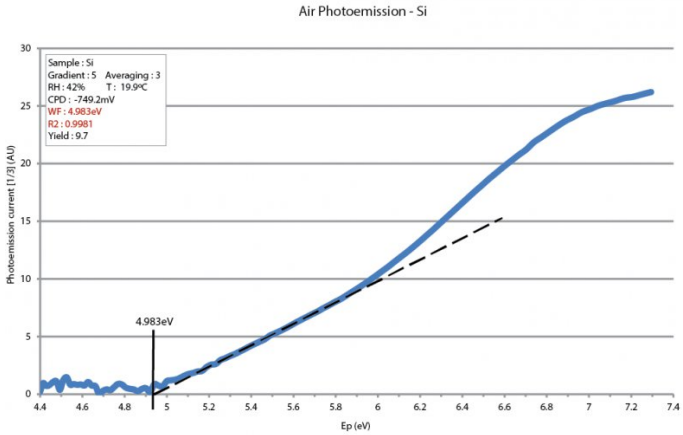

Figure 3.15: Air photoemission spectra of silicon. Dashed line represents linear extrapolation of photo current cube root. Adopted from [102].

3.2.8 Ultraviolet-Visible-Near Infrared Spectroscopy

In this work Ultraviolet-Visible-Near Infrared (UV-VIS-NIR) spectroscopy is used to measure material transmittance (T) and reflectance (R) spectra in the wavelength range of 300 - 1200 nm. Since light can be transmitted, reflected or absorbed, the absorbance (A) spectra can be obtained using relation:

$$A = 1 - R - T. \tag{3.14}$$

Additionally, having transmittance and reflectance spectra the absorption coefficient α can be calculated using formula [103] :

$$\alpha = \frac{1}{t} ln \left[\frac{(1 - R(\lambda))^2 + [(1 - R^4(\lambda)) - 4R^2(\lambda)T^2(\lambda)]^{1/4}}{2T(\lambda)} \right] \tag{3.15}$$

, there t is film thickness, which in our case is determined by SE. Subsequently, the Tauc plot of material can be obtained by applying relation (3.16)

$$\alpha h\nu = A(h\nu - E_g)^n \tag{3.16}$$

, there A is a constant and E_g is an optical band gap. The power factor n depends on the structure of the band gap [103]. In case of direct band gap, the n is equal to $1/2$, while for indirect band gap n is 2. From formula (3.16) it follows that on-set of Tauc plot is determined by the optical band gap of material. Thus, the value of optical band gap can be estimated by linear extrapolation of the on-set edge.

3.2.9 Contact Angle Measurements

Contact angle measurements are used to investigate surface wettability. Using this method the liquid drop is placed on the solid surface. Eventually, the molecular forces acting between liquid and solid surface equilibrates and liquid droplet attains static shape. The form of the droplet depends on the pressure, temperature, and on the material properties of investigated liquid and solid surface. If first two parameters are kept constant the droplet shape is determined by materials properties. When the interaction between liquid and solid surface is strong, a surface is hydrophilic or in other words highly wettable. In this case, liquid droplet is flattened and the angle between surface and droplet surface is acute $\theta_c < 90°$. When the interaction between liquid molecules and solid surface species is weak the surface is hydrophobic, meaning that contact angle $90° < \theta_c < 150°$. Lastly, if the contact angle is above 150°, the surface is non-wettable. All the aforementioned cases are summarized in the figure 3.16.

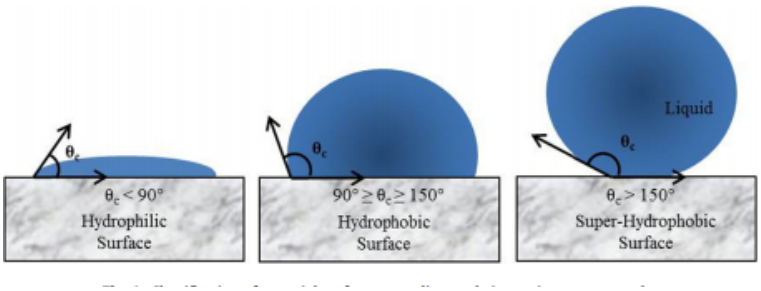

Figure 3.16: Classification of material surfaces according to their wetting contact angles. Adopted from [104].

3.2.10 Scanning Electron Microscopy

Scanning electron microscopy (SEM) is a high-vacuum technique used for imagining specimen topography at the resolution down to few nm. Unlike conventional light microscope, this technique employs electrons (see Figure 3.17) to attain an image of the specimen surface.

Utilizing this technique, an electron beam is accelerated up to 2.00 keV energy and focused to the sample by the magnetic lens system. After hitting the sample incident electrons can be backscattered or they can generate secondary electrons by ionizing atoms present in the sample. Subsequently, backscattered and secondary electrons are collected by the separate detectors. The

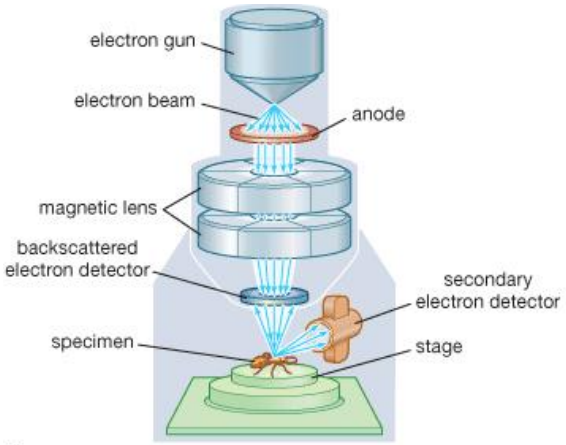

Figure 3.17: Principle scheme of SEM microscope. Adopted from [105]

former electrons are collected by a detector which is above the sample, whereas the secondary electrons are collected by a detector, which is on the side of the stage (see Figure 3.17). By collecting electrons in raster scanning mode the magnified topographical image of specimen surface is produced. Additionally, SEM can be also used for cross-sectional sample imaging. In this case, a sample has to be bisected by focused Gallium ion beam.

3.2.11 Transmission Electron Microscopy

The magnification capabilities of conventional light microscopes are limited by the wavelength of photons. These type of microscopes are not sufficient when investigating structures and features in the scale of Ångstroms. In order to gain information on features at the Ångstrom level transmission electron microscopy (TEM) is used. Similarly as in SEM, TEM employs electrons, but here electrons are accelerated up to 200 keV. The wavelength of accelerated electrons reduces down to picometers. Owing to limited electron penetration depth thickness of analysed sample has to be less than 100 nm.

The principle scheme of TEM microscope is depicted in the Figure 3.18. As it can be seen, microscope consists of an electron source, a magnetic lens (condenser) system and imaging system. By changing the configuration of condenser system and detectors, TEM can be operated in two different modes, which are described below.

- Conventional TEM.

  Operating TEM in this mode broad electron beam, which is parallel to optical axis, is directed to a specimen. Electrons, which penetrated through the sample, are focused by the magnetic lens system. Then electrons pass through the optical aperture, which filters out highly scattered electrons. Thus, transmitted and weakly scattered electrons are collected at the detector. The intensity and energy of incoming electrons depend on density, crystallinity and nuclei mass of the material that specimen is made of. By means of charge-coupled device image of scanned sample is obtained.

- Scanning TEM.

  Unlike conventional TEM, scanning TEM utilizes a narrow electron beam having a spot size of 0.05-0.2 nm. The sample is scanned in raster mode in such a way that electron beam remains parallel to the optical axis. Then transmitted electrons are collected at the detectors. In contrast to CTEM, performing STEM measurements only strongly scattered electrons are detected at high-angle annular dark field (HAADF) detector, which has a shape of an extended ring (see Figure 3.19). Moreover, other characterization techniques such as

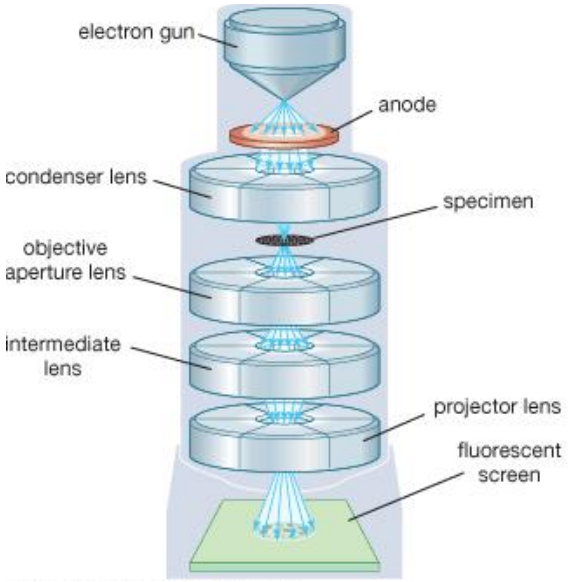

Figure 3.18: Principle scheme of TEM microscope. Adopted from [106]

energy dispersive X-ray spectroscopy (EDX) or electron energy loss spectroscopy (EELS) can be used along with scanning TEM.

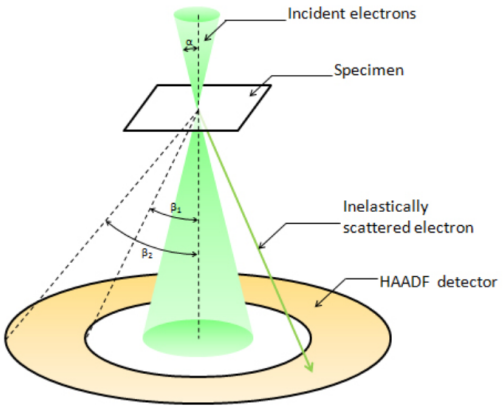

Figure 3.19: Representation of HAADF detector. Adopted from [107].

3.3 Perovskite Solar Cells

3.3.1 Fabrication of Perovskite Solar Cells

Complete perovskite solar cells are fabricated at Helmholtz Centrum Berlin, whereas ALD NiO_x depositions are done at Eindhoven University of Technology. Patterned ITO/glass substrates (30 mm x 30 mm), which are used as the front transparent contact, are ultrasonically cleaned for 5 minutes in dissolved detergent, deionized water, and isopropanol, respectively. Then NiO_x hole transport layer is deposited by ALD technique. Prior to perovskite deposition, NiO_x/ITO/glass stacks are pristine, post-annealed in air at 150°C for 1 hour or at 300°C for 20 min. The following fabrication steps are done in N_2 atmosphere. The perovskite is prepared following the typical

triple cation perovskite [72] process and it is spin coated on top of NiO_x/ITO/glass using one step solution process (4000 rpm for 35 s). After 25 seconds of spinning ethyl acetate anti-solvent drop is utilized. Afterward, the spin-coated perovskite films are annealed at 100 °C for 1 h. Lastly, 15 nm electron transport layer C60/BCP and back electrode Cu are thermally evaporated.

3.3.2 Characterization of Perovskite Solar Cells

In general, a performance of the solar cells is determined from current density vs. voltage (J-V) graphs. In order to find the relation between voltage and current density, the solar cell is illuminated by light which simulates 1 Sun spectrum at 1.5 atmospheric mass (AM) conditions. Then by applying incrementally increasing or decreasing voltage to the solar cell electrodes and by simultaneously measuring current density, the (J-V)graph is recorded. The example of (J-V) graph is shown in Figure 3.20. As it can be seen (J-V) curve has to specific points, which determine open circuit voltage and short circuit current density. The definitions of these parameters are presented below:

- The open circuit voltage (V_{OC}) value shows the maximum possible voltage in the solar cell when no current is flowing across the electrodes. In ideal semiconductors, the (V_{OC}) is equal to the splitting of quasi-Fermi levels.
- The short circuit current density (J_{SC}) value shows the maximum possible current density in the solar cell when the voltage is zero.

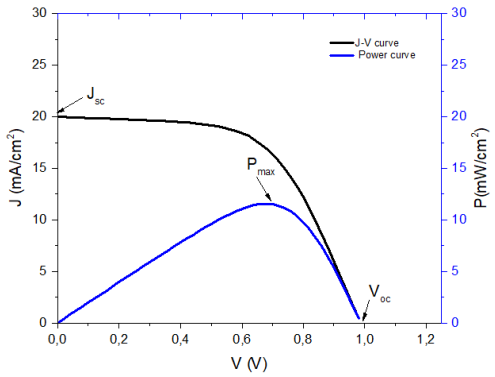

Figure 3.20: Typical (J-V) curve of perovskite solar cells. J_{SC} is maximum current density point and V_{OC} point indicates maximum voltage in the solar cell. P_{max} shows at what voltage highest possible power is achieved.

Knowing the relationship between current density and voltage, the maximum power density of the solar cell can be found by applying formula as follows:

$$\frac{d(J_{max}V_{max})}{dV} = 0. \tag{3.17}$$

Usually, maximum power is not used for comparing and benchmarking solar cells. Instead, the fill factor (FF) parameter is used, which is a ratio between maximum power point and product of J_{SC} and V_{OC}. In ideal case FF of efficient solar cells may come close to unity.

$$FF = \frac{P_{max}}{J_{SC}V_{OC}} \tag{3.18}$$

The power conversion efficiency (PCE) of the solar cells is obtained by dividing solar cell output power by incident power. However, it is well documented that perovskite solar cells suffer from

degradation which leads to a noticeable reduction in PCE. Thus, static PCE measurements are not informative enough. In order to get more information about the perovskite solar cells performance, the maximum power point (MPP) is tracked for the given period of time. The negative slope of MPP curve indicates that solar cell performance drops over time (see Figure 3.21).

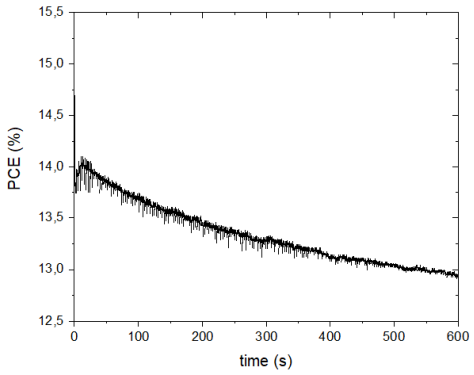

Figure 3.21: Representation of MPP tracking graph of perovskite solar cell.

Additionally, the shape of (J-V) curve is governed by electrical resistance in the solar cells. Series resistance (R_s) is associated to the intrinsic resistivity of charge transport layers, photo-active layer and electrodes. Shunt resistance (R_{sh}) is determined by the uniformity of each layer in the solar cell stack. In the case of poor quality films, which have pin-holes, shunt resistivity decreases. Taking into account both aforementioned resistances, the diode equation for solar cells is described as follows:

$$I = I_L - I_0(e^{q(V+IR_s)/k_BT} - 1) - \frac{V + IR_s}{R_{sh}} \tag{3.19}$$

, where I_L is photocurrent, I_0 is saturation current, k_B is Boltzmann's constant, T is absolute temperature. The influence of R_s and R_{sh} on J-V curve is depicted in the Figure 3.22.

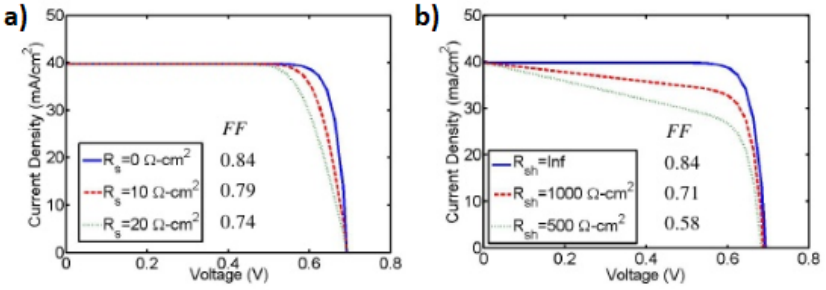

Figure 3.22: a) indicates the effect of series resistance and b) shows the influence of shunt resistance. Adopted from [108].

As it can be seen, the (J-V) curves of solar cells with higher R_s (see Figure 3.22 a)) exhibit less steep slopes in the V_{oc} range. Accordingly, FF of the solar cell is lower, which means that the efficiency of the solar cells drops. The shunt resistance also has an influence on the solar cell performance. Figure 3.22 b) shows that FF decreases with shunt resistance. As previously mentioned, one of the possible reasons for low shunt resistance is the existence of pin-holes in any of the solar cell stack layer. These pin-holes may form ohmic shunt pathways, which are

detrimental to solar cells. Therefore, in order to have highly efficient solar cells it is important to make sure that R_s is low and R_{sh} is very high.

To gain further insight into solar cell performance, measurements of external quantum efficiency (EQE), which is the ratio of the number of charge carriers collected by the solar cells to the number of photons of a given energy shining on the solar cell, are done. Example of EQE spectra is presented in the Figure 3.23. The on-set in the longer wavelength regions provides information about the band gap of the photoactive layer. The cut-off region indicates the wavelength of the most energetic photons that can be successfully converted to electrons which are in turn extracted from the solar cells. The integral of EQE curve is associated to J_{SC} value, which is obtained from (J-V) measurement. Thus by comparing (J-V) and EQE graph more information about J_{SC} can be obtained.

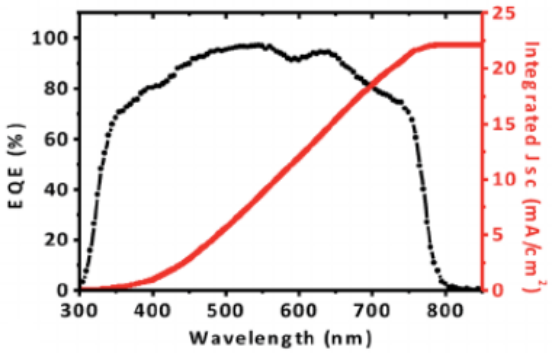

Figure 3.23: Representation of perovskite solar cell EQE and integrated J_{SC} spectra. Adopted from [109].

Chapter 4

Atomic layer deposition of Nickel Oxide

4.1 Literature overview

NiO_x films can be produced using various combinations of Ni precursors and co-reactants. For instance, it is reported that nickel bis-cyclopentadienyl ($Ni(Cp)_2$)[110], [111], nickel bis-ethylcyclopentadienyl ($Ni(EtCp)_2$) [111], and nickel bis(1-dimethylamino-2-methyl-2-butanolate) $Ni(dmamb)_2$ [31] in combination with ozone (O_3) are used for ALD NiO_x film deposition. Furthermore, there are studies reporting that ALD NiO_x films are produced utilizing nickel bis(N,N-ditertialbutylacetamidinate) ($Ni(^tBu_2\text{-}AMD)$)[29], nickel bis(N,N- di-tert-butylacetamidinate) $Ni(^tBu\text{-}MeAMD)$[87], nickel (1-dimethylamino-2-methyl-2-propanolate) $Ni(dmamp)_2$ [112] precursor in combination with water (H_2O). Apart from all aforementioned NiO_x ALD recipes, which are based on thermal process, Song *et al.* [113] demonstrated that ALD NiO_x films can be produced utilizing plasma enhanced ALD process. In this particular case, the combination of nickel bis-methylcyclopentadienyl $Ni(MeCp)_2$ precursor and oxygen plasma were used. A brief summary of reported ALD NiO_x processes is presented in Table 4.1.

Table 4.1: NiO_x precursors and co-reactants and GPC obtained in the table temperature range of 120 - 230°C.

Precursor	Precursor molecular formula	Co-reactant	ALD	GPC (nm/cycle)	Substrate	Temperature (°C)	Paper
$Ni(Cp)_2$	$C_{10}H_{10}Ni$	O_3	Thermal	0.092	Si	230	[110]
$Ni(Cp)_2$	$C_{10}H_{10}Ni$	O_3	Thermal	0.32	Si	150	[111]
$Ni(EtCp)_2$	$C_{14}H_{18}Ni$	O_3	Thermal	0.09	Si	150	[111]
$Ni(dmamb)_2$	$C_{14}H_{32}N_2O_2Ni$	O_3	Thermal	0.34	Si	200	[31]
$Ni(^tBu_2\text{-}AMD)_2$	$C_{20}H_{42}N_4Ni$	H_2O	Thermal	0.075	FTO	175	[29]
$Ni(^tBu\text{-}MeAMD)_2$	$C_{20}H_{42}N_4Ni$	H_2O	Thermal	0.039	Si	200	[87]
$Ni(dmamp)_2$	$C_{12}H_{32}N_2O_4Ni$	H_2O	Thermal	0.08	Si	120	[112]
$Ni(MeCp)_2$	$C_{12}H_{14}Ni$	O_2	Plasma	0.04 - 0.075	W,Pt,Ru	150	[113]

As it can be seen, GPC values vary from 0.039 nm/cycle to 0.34 nm/cycle. Highest growth rates are achieved by thermal ALD process utilizing ozone O_3. However, there is one exception for $Ni(EtCp)_2/O_3$ recipe. In this case, the GPC is comparable with ALD reactions using water as a co-reactant. From theory, it is known that GPC can be limited due to low precursor and co-reactant reactivity or bulky ligands, which may block surface reactive sites and induce steric hindrance effects. In fact, $Ni(EtCp)_2$ ligands are larger than the ones in $Ni(Cp)_2$ precursor. Thus, in $Ni(EtCp)_2/O_3$ case lower GPC may be attributed to the steric hindrance effect [111], which is responsible for limited precursor adsorption. Moreover, the GPC of plasma enhanced $Ni(MeCp)_2/O_2$ ALD process is comparable with water-based ALD reactions. In conclusion, NiO_x films can be produced by thermal and plasma ALD process and the highest GPCs are attained when utilizing O_3 as a co-reactant.

4.2 General Procedure

In this work plasma enhanced ALD process for NiO_x has been developed in an ALD-1 home-built reactor, which scheme can be found in Figure 3.2. Before starting NiO_x depositions, ALD reactor walls are coated with Al_2O_3 (500 thermal ALD cycles) and NiO_x (200 plasma ALD cycles). It is done in order to prevent contamination originating from previous ALD processes. Then substrates are loaded into the reaction chamber and placed on the table, which is heated up to the predefined temperature. Subsequently, turbopumps are switched on to reduce pressure inside the chamber. When pressure in the chamber reaches base level ($3x10^{-6}$ mbar), the substrate is exposed to oxygen plasma in order to remove surface contamination and prepare it for NiO_x depositions. After that ALD NiO_x process starts. In the first step the Ni precursor is injected into the ALD reaction chamber by Argon gas flow. Then introduced Ni precursor reacts with available substrate surface sites. Upon reaction, Ni precursor loses one of the ligands owing to a newly formed bond between nickel and groups. The precursor dosing step continues till all available surface sites react with Ni precursor and saturation is reached. After that second step starts and reaction by-products along with residual precursor are purged and pumped away with Argon gas. Considering that any remaining residual by-products may trigger CVD reactions, which are detrimental to ALD process, the purge time step should be sufficiently long in order to remove all reaction products. After a successful purge step, the third step is initiated. Initially, ALD chamber is filled with oxygen. Subsequently, oxygen pressure inside the reaction chamber stabilizes and plasma is ignited by ICP plasma source. Generated plasma species start to react with the surface, which is passivated by Ni precursor. During this event, oxygen plasma reacts with Ni precursor ligands and eliminates them from Ni atom. Plasma exposure step continues until ligands from accessible surface sites are removed. Afterwards, residual oxygen species and generated by-products are purged away with Argon gas. Completion of this purging step finalizes one ALD cycle. Ideally, a mono-layer of NiO_x is deposited every single cycle. Thereby, the thickness of the produced material is controlled by a number of ALD cycles.

4.3 Development of ALD Recipe

- **General information about $Ni(MeCp)_2$ precursor**

  In this study Bis-methylcyclopentadienyl-nickel ($Ni(MeCp)_2$) precursor is chosen. The structural formula of $Ni(MeCp)_2$ (Sigma-Aldrich, 97% purity) precursor is presented in the Figure 4.1.

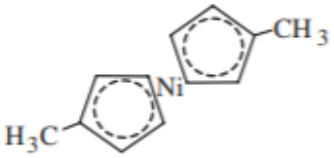

Figure 4.1: Structure of $Ni(MeCp)_2$ precursor. Nickel is in +2 oxidation state. Adopted from [114].

  As it can be seen, nickel is divalent, connected to two methyl-cyclopentadienyl (MeCp) rings. It is well documented that at room temperature this precursor is in a solid state and has green colour [114],[115]. The melting point of this precursor is around 36° C, thereby at relatively low temperatures this precursor starts to sublimate and becomes volatile. This intrinsic feature is beneficial for ALD since this technique is based on vapour phase reactions. Considering co-reactant or in other words oxidizer, similarly as in the only reported plasma enhanced ALD NiO_x paper [113] oxygen plasma is chosen.

- **Challenges of using $Ni(MeCp)_2$ precursor**

In CVD community $Ni(MeCp)_2$ precursor is known as a good option to deposit high-quality NiO_x films [116]. However, it is reported that $Ni(MeCp)_2$ has two main drawbacks. Firstly, the deposition rate of CVD processes utilizing $Ni(MeCp)_2$ is slow [116],[117]. Referring to the Table 4.1, ALD process based on $Ni(MeCp)_2$ has also slow growth rate. In comparison to other ALD processes reported in the literature, its GPC is 3-10 times smaller. Secondly, it is reported that $Ni(MeCp)_2$ precursor is not thermally stable and it gradually decomposes when placed in a crucible in air [114]. Actually, in this work it is observed that GPC of $Ni(MeCp)_2/O_2$ plasma process gradually drops and after 4-5 days precursor loses its reactivity. Considering the fact that $Ni(MeCp)_2$ is not thermally stable, this behaviour is attributed to the decomposition of the Ni precursor. Slow growth rate and relatively short time window for effective precursor usage makes $Ni(MeCp)_2/O_2$ ALD process technically challenging.

- **NiO_x ALD process parameters and saturation curves**

  In this work, NiO_x depositions are done at table temperature of 150°C. The base pressure during the ALD process is set at $3x10^{-6}$ mbar, whereas the operating pressure level is $\approx 10^{-3}$ mbar. Precursor bubbler is heated up to 55° C, which is enough to make $Ni(MeCp)_2$ precursor volatile [114]. In order to prevent precursor and by-products from condensation and adsorption on the tube walls, the inlet and exhaust lines are kept at 75°C. The power of inductively coupled source power is set to be constant at 100 W.

  A very important aspect of the ALD process is a duration of all four individual steps (see subsection 4.2). In order to achieve reproducible and high-quality NiO_x films, the timing of each step in the ALD process has to be optimized in such a way that the growth rate is in saturation mode. To determine necessary and desired time steps, saturation graphs are made. The procedure how of to acquire data for these graphs is presented below:

  – ALD recipe is prepared in such a way that the time interval of analysed step is variable, while the time of other steps is kept constant; for instance, the recipe for Ni precursor dosage time analysis follows this time steps sequence x-b-c-d; there x is variable (precursor dosage time), b - purge time, c - oxygen plasma time , d - purge time;

  – a layer thickness of the film being deposited is measured every 350 cycles by SE;

  – growth per cycle for given recipe is calculated and measurements are repeated several times;

  – variable time step is changed.

  The obtained saturation curves for all four plasma-enhanced ALD NiO_x process steps are presented in the Figure 4.2.

  As it can be seen the GPC saturation is achieved when precursor dosage time is 3 s (Figure 4.2 a)). The initial non-saturated growth in the first 3 seconds may be attributed to the slow precursor adsorption. Considering the precursor purge time, it is observed that after 1s time step of precursor purge (Figure 4.2 b)), saturated GPC is observed. Here, the flat shape of the GPC curve implies that CVD reactions are sufficiently suppressed. Figure 4.2 c) indicates that 3 seconds of plasma exposure is sufficient to achieve saturated GPC. Lastly, Figure 4.2 d) shows that the GPC saturation is achieved after the plasma is purged for 1 s. In comparison to thermal NiO_x ALD process, which requires 8 s of co-reactant purge step to achieve GPC saturation [118], in this work the attained time step for oxygen plasma purge is noticeably shorter. The longer co-reactant purge time in case of thermal ALD processes may be associated to the slow co-reactant desorption from reactor walls [90]. In order to ensure that NiO_x is deposited by ALD reactions, the final recipe is built according to the results of saturation curves. Thus, in this work NiO_x ALD cycle consists of 3 seconds of precursor dose step, followed by 3 seconds of purge step, then oxygen plasma is ignited for 3 seconds and the last purge step is done for 1 s.

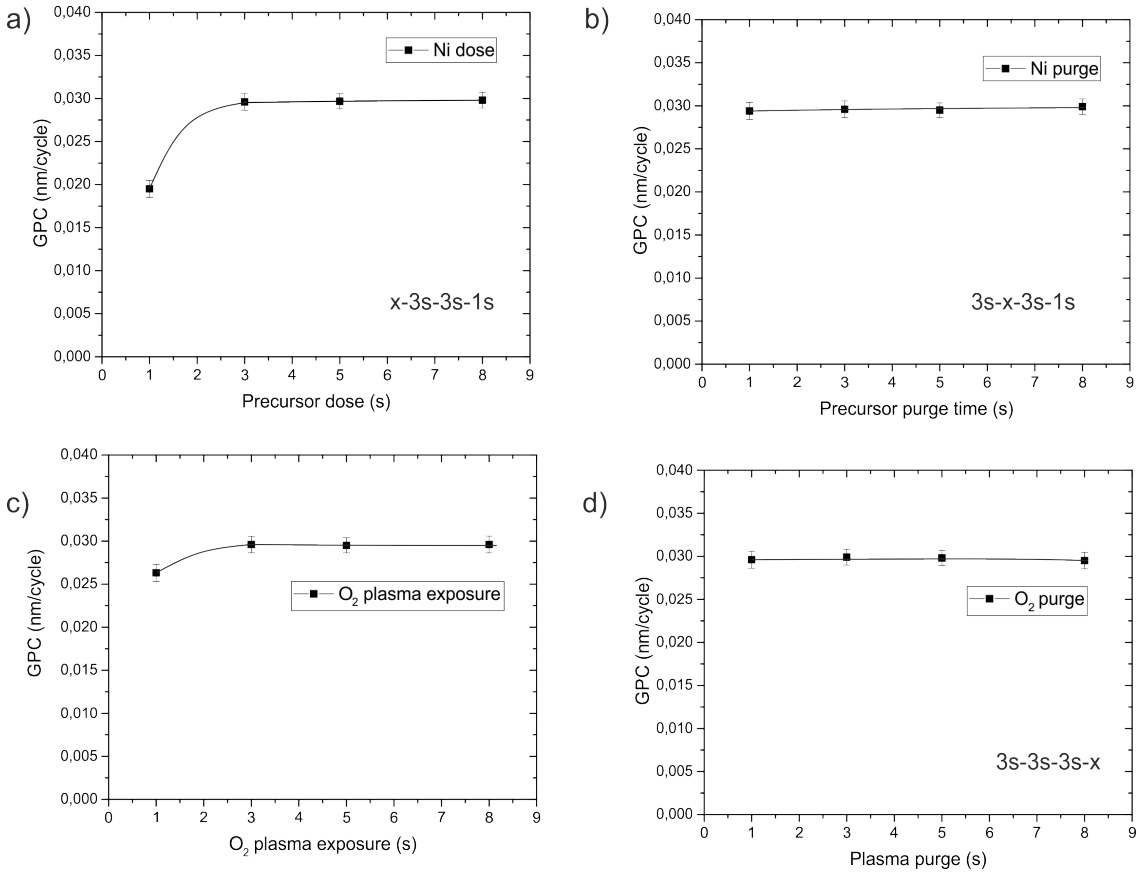

Figure 4.2: Saturation curves of a) $Ni(MeCp)_2$ precursor dosing step, b) precursor purge step, c) O_2 plasma step and d)plasma purge step.

From all saturation curves, it is seen that maximum attainable GPC is in the range of 0.03 nm/cycle, which is comparable with Song *et al.* [113] results on same ALD NiO_x process. However, compared to the other ALD NiO_x papers presented in Table 4.1, in this work GPC is substantially lower. In fact, as previously pointed out Park in book [116] has reported that $Ni(MeCP)_2$ precursor is known for slow deposition rates [116]. Thereby, low GPC values are solely attributed to $Ni(MeCp)_2$ precursor. In order to unveil and clarify the root of low GPC, theoretical and experimental studies on precursor reactivity are required.

- **Proposed scheme of NiO_x ALD reactions** According to the in-situ studies on Sc_2O_3 ALD processes utilizing $Sc(MeCp)_3$ [119] and on ZrO_2 ALD based on $[Zr(MeCp)_2(Me)(OMe)]$ precursor [120], MeCp ligands upon reaction with surface groups form MeCpH compound. Following these findings, the proposed scheme of NiO_x ALD reactions is presented in Figure 4.3. As it is depicted in step a), a substrate has OH terminated surface, which reacts with $Ni(MeCp)_2$ precursor. Upon precursor adsorption on the surface, one of the precursor ligands is eliminated owing to (MeCp)-Ni-O bond formation. Removed ligand bonds with a hydrogen ion, which leads to the creation of MeCpH. Nickel precursor adsorption continues for 3 seconds till GPC saturation is reached. Afterwards, the purging step is initiated. Figure 4.3 b) shows that upon completion of the purging step (3s) the surface is terminated by MeCp ligands. At the beginning of the second half-cycle oxygen plasma is ignited. Figure 4.3c c) demonstrates that oxygen plasma reacts with MeCp ligands and it is expected that upon reaction ligand is converted into CO_2 and H_2O molecules [113]. Subsequently, OH groups bonds to Ni metal due to the existence of unsaturated bonds. The oxygen plasma step goes

for 3 seconds until all accessible ligands are eliminated. Afterwards, reaction by-products (CO_2, H_2O) and residual oxygen are purged away with Argon gas. After successful purge step surface is completely terminated by OH groups (see Figure 4.3 d)). However, in order have a better understanding about ALD NiO_x reaction mechanism, in-situ quadrupole mass spectrometry (QMS) and/or in-situ Fourier-transform infrared (FTIR) spectroscopy have to be used.

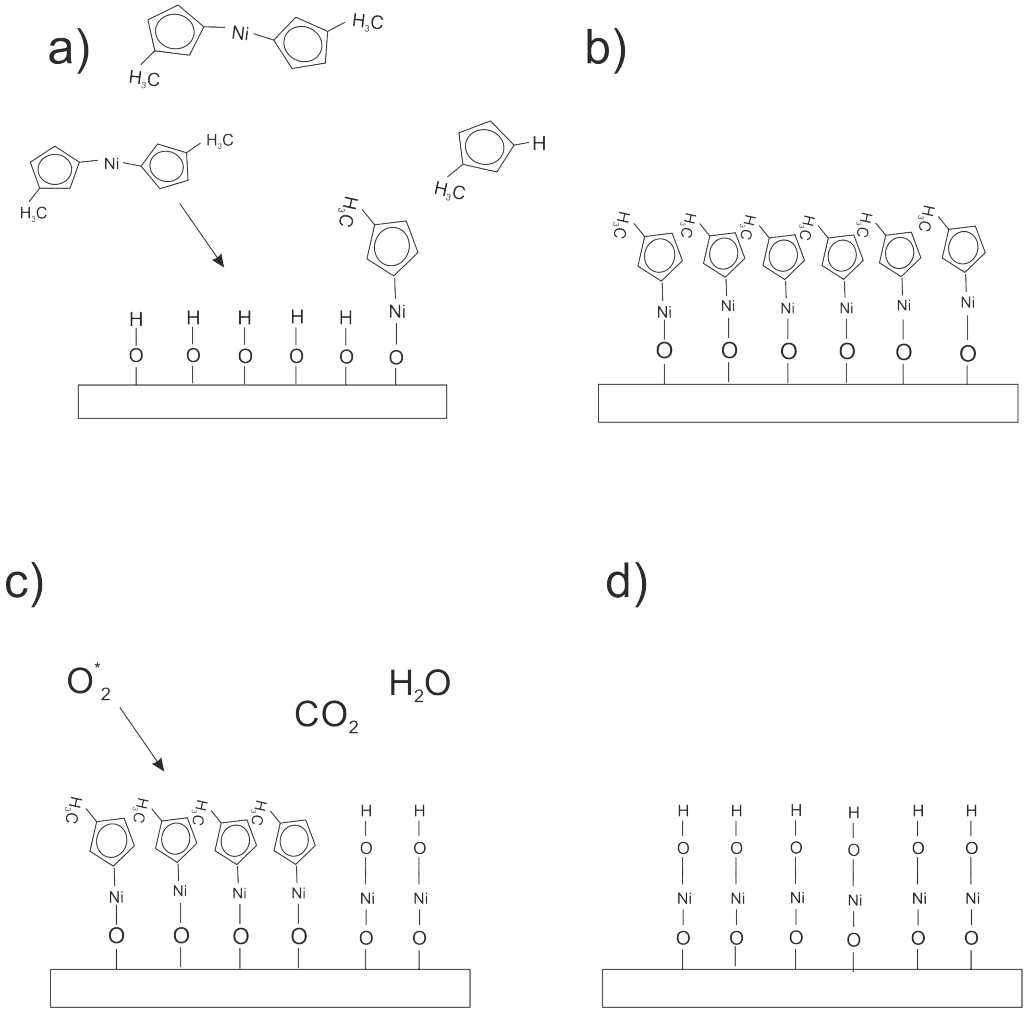

Figure 4.3: Proposed ALD reaction schemes for: a) $Ni(MeCp)_2$ precursor dosage, b) precursor purge, c) O_2 plasma dosage d) plasma purge steps.

Chapter 5

Results and Discussions

5.1 Material Characterizations of Atomic Layer Deposited Nickel Oxide

In this section, the morphology, chemical composition, electronic structure and optical features of pristine 10nm NiO_x films deposited by ALD at 150°C are presented and compared with the literature.

5.1.1 NiO_x Morphology

In ALD literature it is well documented that NiO_x morphology depends on the ALD chemistry. For instance, it has been reported that amorphous NiO films are obtained using $Ni(MeCp)_2/H_2O_2$ [121], $Ni(dmamp)_2/H_2O$ [112], $Ni(dmamb)_2/H_2O$ [122] recipes, whereas (100) oriented NiO films are processed by running $Ni(apo)_2$ and $i(dmg)_2/O_3$ [123] , $Ni(acac)_2/O_2/H_2O$ [124] ALD recipes. Considering the morphology of NiO_x films deposited utilizing ALD chemistry $Ni(MeCp)_2/O_2$ plasma, Song *et al.* has reported that NiO_x films are polycrystalline. To double check if it is the case in this work, the morphology of ALD NiO_x is analysed. In order to investigate the bulk morphology of NiO_x films, XRD measurements are performed. Since NiO_x film is only 10 nm thick, the XRD set-up is configured in grazing-incidence mode. In this way, the contribution of diffraction peaks coming from the substrate is minimized. Figure 5.1 demonstrates XRD diffractogram of as-deposited ALD NiO_x film. Clear peak structure illustrates that film is polycrystalline. The presence of crystal planes having Miller indices (111), (200), (220) and (311) indicates that NiO_x is in cubic phase [31],[87],[125].

The unit cell of cubic NiO_x phase has rock-salt, NaCl structure, which is depicted in the figure 5.2. From here it follows that NiO_x (200),(220),(311) crystal planes consist of nickel and oxygen atoms. In contrast to that, (111) crystal planes consist of alternating nickel and oxygen planes. Thereby, these planes have strong dipolar momentum [126]. In fact, it is reported that due to polarity (111) NiO_x surfaces easily hydroxylate via dissociative water adsorption reactions [126],[127],[128],[129], whereas (200),(220) [128], [130] and (311) surfaces are less reactive and dissociative water adsorption is less likely to happen. Therefore, owing to the presence of (111) crystal planes, it is expected that the surface of polycrystalline NiO_x film is hydroxylated and that NiO_x films are hydrophilic. In order to check these hypotheses, NiO_x surface chemistry is investigated by means of XPS, while surface wettability is assessed by water contact angle measurement. The results of XPS study is presented in the next subsection, whereas the results of water contact angle measurements are presented in the subsection 5.2.5.

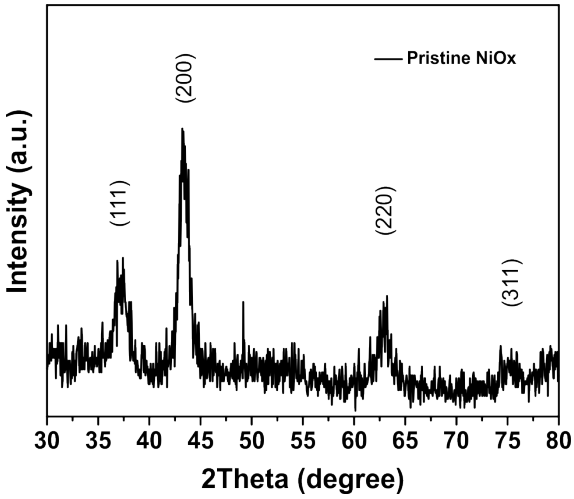

Figure 5.1: XRD spectrum of pristine ALD NiO_x thin film.

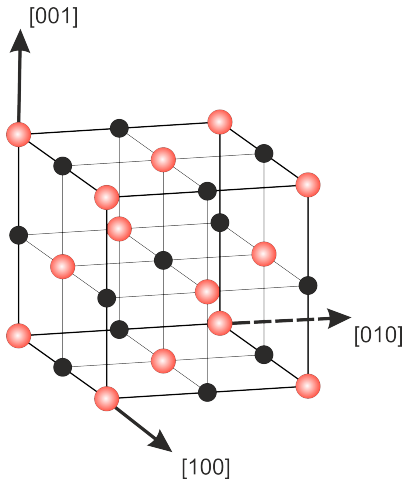

Figure 5.2: Unit cell of NiO crystal. Oxygen ions are in red and nickel are in black. The coordinate axes are defined by Miller indices.

5.1.2 Chemical analysis of pristine NiO_x

In this work, angle-resolved XPS (AR-XPS) is employed to investigate NiO_x surface chemical environment. Following from previous subsection 3.2.4, XPS probing depth can be controlled by adjusting the electron take-off angle. In this section, the results of AR-XPS measurements done at 90° (lower surface sensitivity) and 15° (higher surface sensitivity) are presented and discussed.

In figure 5.3 a) the XPS spectrum of Ni $2p_{3/2}$ obtained at 90° electron take-off angle is presented. As it is seen,the spectrum is deconvoluted into four individual peaks. First located at the 853.9 eV is attributed to Ni^{2+} ions in NiO crystal lattice. Its binding energy is in good agreement with the literature values [131],[132],[133]. The second peak located at 855.9 eV is attributed to hydroxyl groups (nickel hydroxides $Ni(OH)_2$ and nickel oxy-hydroxides NiOOH) [31],[129],[88],[134],[135],which are present due to water adsorption on NiO_x surfaces or because of hydroxylated Ni sites, which have not reacted during ALD. Lastly, the third and fourth peaks in Ni $2p_{3/2}$ spectrum located at 860.6 eV and 864 eV are satellites, which are the result of the shake-up process.

Figure 5.3 b) presents the XPS spectrum of Ni $2p_{3/2}$ at the take-off angle of 15 °. Due to reduced electron detection angle, measurement results are more surface sensitive, thus the contribution of

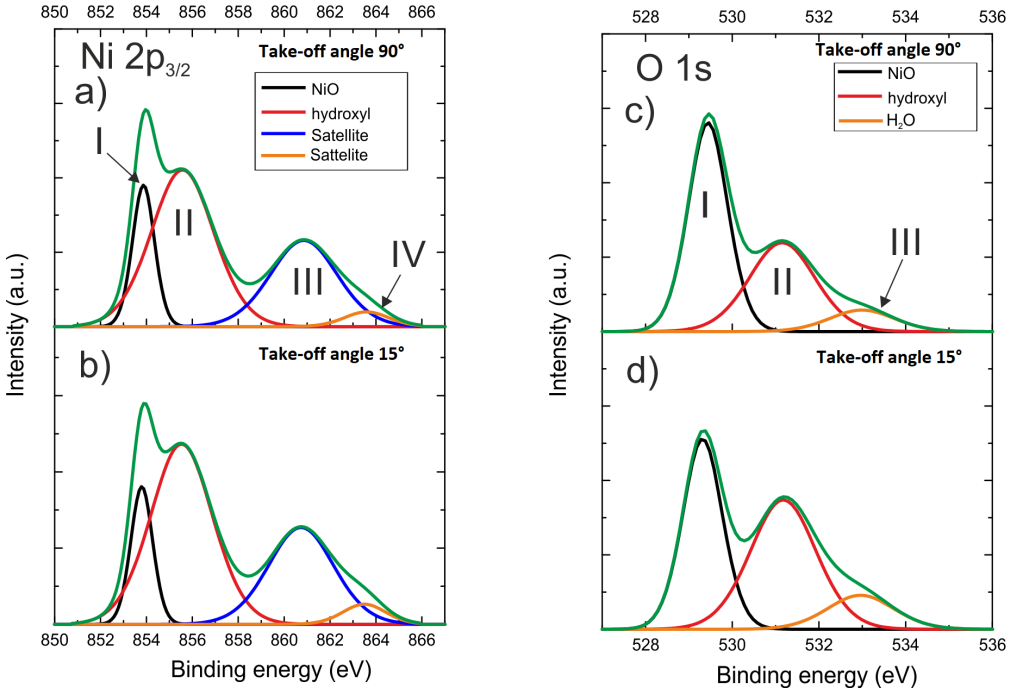

Figure 5.3: The AR-XPS spectrum of ALD NiO_x, a) $Ni2p_{3/2}$ at take-off angle 90°,b) $Ni2p_{3/2}$ at take-off angle 15° and c)O1s at take-off angle 90°, d)O1s at take-off angle 15°. The satellite peaks in $Ni2p_{3/2}$ spectrum are the consequence of the shake-up process during photo emission.

surface species can be observed more accurately. In order to compare results obtained at 90° and 15°, a ratio of integrated peak areas is taken as a comparative parameter, since peak intensities are angle dependent. The ratio of integrated areas of peaks corresponding to hydroxyl groups and NiO is calculated and results are presented in Table 5.1. It is clearly seen that hydroxyl groups/NiO ratio is higher in the case when XPS measurements are done at 15∘. This observation strongly suggests that hydroxyl species are more present at the surface and that additional hydroxyl groups are formed when water chemisorbs on NiO_x surface. Therefore, it means that the concentration of hydroxyl species is higher at the surface and these species could be denoted as surface groups. Similar behaviour is observed by Manders *et al.* [136].

Table 5.1: Ratio of integrated peak areas obtained from $Ni2p_{3/2}$ spectra when take off angle is set at 90° and 15°. In case of results obtained at 90°, error bars are determined from three individual analyses.

	Ratio of integrated peak areas
Take off angle	hydroxyl groups/NiO
90	3.29 ± 0.15
15	3.69

The XPS spectra of O 1s electrons are presented in figure 5.3 c) (take-off angle 90°) and d) (take-off angle 15°). The envelope of O 1s XPS spectrum is deconvoluted into three individual peaks. The one at the binding of 529.4 eV is attributed to the lattice oxygen (NiO) and its binding energy is in good agreement with the literature [131],[136],[137]. The peak at 531.2 eV is assigned to hydroxyl species and its binding energy is comparable with literature [87],[88],[136]. The last peak located at 533 eV indicates the presence of adsorbed water [31]. Similar to Ni 2p spectra analysis, the comparison of O1s spectrum obtained at 15∘ and 90∘ take-off angle is done

by calculating ratio of integrated peak areas. The results are presented in Table (5.2) table.

Table 5.2: Ratio of integrated peak areas obtained from O1s spectra when take off angle is set at 90° and 15°. In case of results obtained at 90°, error bars are determined from three individual analyses.

	Ratio of integrated peak areas	
Take off angle	hydroxyl groups/NiO	H_2O/NiO
90	0.635 ± 0.075	0.105 ± 0.065
15	1.13	0.30

Considering hydroxyl groups/NiO ratio, the similar trend as presented in Table 5.1 is observed. The consistent results confirm the hypothesis that the concentration of hydroxyl groups is higher at the surface layers. However, the relative increase of hydroxyl groups/NiO ratio is higher for O1s spectra. In fact, deposited NiO_x films contain carbon species, which are more prominent at the top surface layer (see Table 5.3). Since NiO_x samples have been transported to the XPS set-up in ambient environment, the presence of the carbon compounds on the surface is detected. In figure 5.4 a) it is seen that adventitious carbon (C-C) and carbon species (C-O-C),(C-O=C) are present in the film. In order to understand the nature of carbon and check if carbon is present in the film NiO_x bulk, sample is etched with Ar^+ ions. After 10.3 seconds of etching the XPS spectra of carbon 1s is noisy (see Figure 5.4 b)) and no pronounced peak is observed. This observation strongly suggests that carbon species are only present on the surface. In this work, all the XPS spectra are corrected with respect to C-C peak which binding energy is at 284.8 eV.

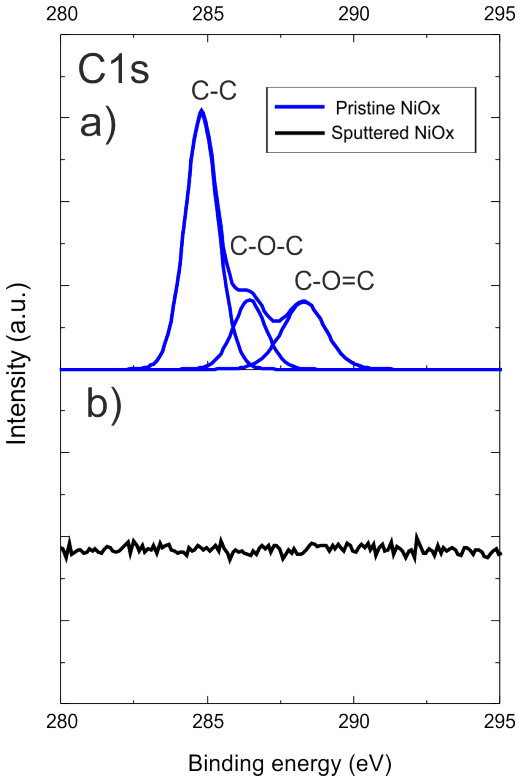

Figure 5.4: XPS spectrum of carbon species of pristine a) and 10.3 seconds sputtered with Ar^+ ions b) ALD NiO_x 10nm samples.

These carbon species are bonded to oxygen and form C-O and C=O bonds. The binding energy of O1s electrons in C-O, C=O environment is overlapping with O1s binding energy in hydroxyl

groups. Therefore, the more noticeable contrast in hydroxyl groups/NiO ratio is associated to the C-O, and C=O species. Additionally, results in Table 5.1 show that ratio of H_2O/NiO increases with lower take-off angle. This observation implies that adsorbed water is mainly present at the NiO_x surface.

Table 5.3: Atomic concentration of NiO films measured by XPS at take-off angles of 90° and 15°. In case of results obtained at 90°, error bars are determined from three individual analyses.

	Atomic concentration [%]		
Take off angle	Ni	O	C
90	27.1 ± 5.6	52.5 ± 1.5	20.4 ± 2.6
15	16.04	46.95	37.03

Ideally, the ratio between nickel and oxygen atoms in NiO_x should be 1:1. However, it is well known that normally NiO_x deviates from stoichiometric Ni-to-O ratio [133]. In order to investigate variations in stoichiometry, XPS quantitative analysis is performed. Before determining stoichiometry NiO_x films are sputtered by Argon ions for 10,3 seconds, so that adsorbed carbon species are removed (see Figure 5.4). Then ALD NiO_x stoichiometry is determined from integrated areas of $Ni2p_{3/2}$ and $O1_s$ spectra. Results presented in Table 5.4 indicate that deposited NiO_x films are oxygen rich.

Table 5.4: Stoichiometry of ALD NiO_x films obtained by XPS analysis.

Element	Photoelectron	Integrated area	Ni:O
O	1s	895.48	1:1.274
Ni	$2p_{3/2}$	702.74	

5.1.3 Electronic Structure of pristine NiO_x

In order to determine valence band maximum (VBM), ionization potential (IP) and work function(WF), UPS characterization technique is used. NiO_x UPS spectrum is presented in the Figure 5.5. As it can be seen, the foot feature is observed in the on-set region. Initially, this spectral

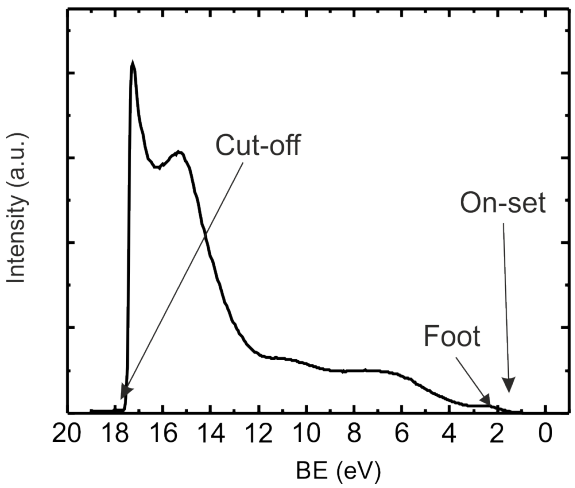

Figure 5.5: UPS spectrum of NiO_x

feature has been assigned to shallow defect, surface states [138]. However, from findings of theoretical studies [98], [139] it is known that NiO_x edge of valence band is formed by nickel 3d and

oxygen 2p electrons (see Figure 5.6). These electrons closely interact with each other, thereby valence band edge analysis can be troublesome. Moreover, nickel 3d and oxygen 2p electrons have different photoionization cross-sections [140], thus the photo-response of these electrons is different at given incident photon energies.

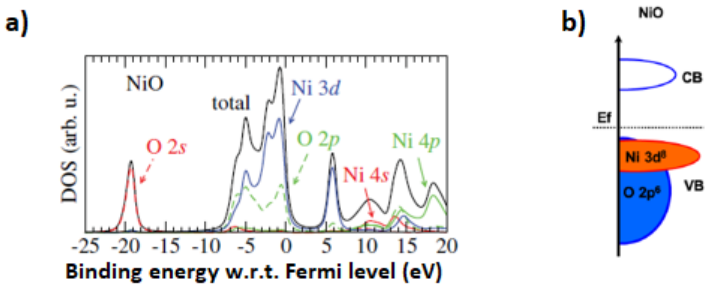

Figure 5.6: a)Electronic structure of NiO. Negative values indicate the energy levels below Fermi level. Adopted from: [139] b) Schematic NiO energy level diagram. Adopted from [23].

Zhang *et al.* [23] has shown that in XPS case the nickel 3d electrons are dominant and form the leading valence band edge. In this case, foot in ALD NiO_x UPS spectrum is not visible. Conversely, Eastman *et al.* [141] and Hufner [98] has demonstrated that on-set region of NiO_x UPS spectra is mainly determined by oxygen 2p electrons. It this case, foot feature in the UPS spectrum is present. Similar behaviour has been observed in other studies [28],[142],[143],[144], thus it is considered that foot in the UPS spectrum on-set region is a valence band feature. Then the leading edges of the UPS spectra are extrapolated using third order polynomial technique (detailed description of this technique can be found in the UPS experimental part 3.2.6). Results obtained from UPS spectrum of ALD NiO_x deposited on ITO substrate 5.7 are presented in Table 5.5. High ionization potential (5.46 eV) indicates that NiO_x has deep valence band, which maximum is 0.68 eV apart from Fermi level. The obtained results are in the range of literature values, which are presented in Table 5.6 (more extensive discussion can be found in subsection 5.1.4. Considering that the optical band gap of NiO_x is between 3.6-3.8 eV (see subsection 5.1.5), UPS results show that the Fermi level is closer to NiO_x films, which suggest is p-type.

Furthermore, NiO_x valence band position is measured utilizing APS technique. Figure 5.8 shows the recorded ion-current graph of ALD NiO_x deposited on n-Si substrate. By applying Fowler's theory, which is presented in subsection 3.2.7, it is found that the ionization potential is 5.21 eV. In comparison, to the UPS results this value is slightly lower. The small discrepancy between values is expected since APS and UPS operate under different conditions. Furthermore, NiO_x films for APS and UPS analysis are deposited on different substrates, thereby substrate induced effects, which are described in the following subsection, cannot be omitted.

Table 5.5: Work function (WF), ionization potential (IP), valence band maximum (eV) of pristine ALD NiO_x 10nm film obtained my means of UPS.

Sample	WF, eV	IP, eV	VBM, eV
Pristine	4.76	5.41	0.65

5.1.4 ALD NiO_x UPS results comparison with literature

As previously pointed out, NiO_x UPS results are in good agreement with the literature. However, it has been noted that literature values of NiO_x ionization potential (4.93 - 6.43 eV) and valence band maximum (0.24 - 1.09 eV) values are widely dispersed (see Table 5.6). Thereby, the main goal of this section is to introduce possible reasons leading to dispersed NiO_x UPS results.

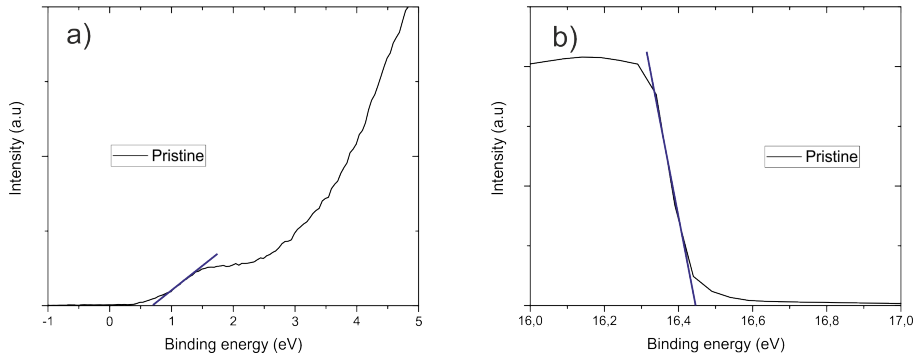

Figure 5.7: a) on-set and b) cut-off region of NiO_x UPS spectra. The leading edges are extrapolated using third order polynomial technique. Fermi level is at 0 eV.

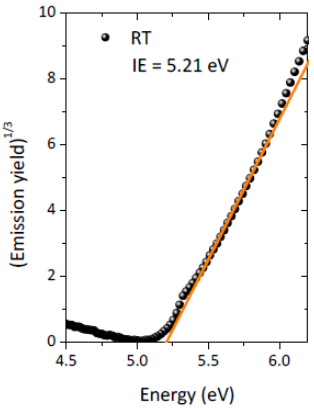

Figure 5.8: APS results of pristine NiO_x film.

All the possible mechanisms responsible for variations in UPS results are listed below:

- **Substrate**.
  There are a couple of studies reporting that the Fermi level of ultra-thin films may be pinned by the substrate. For example, Olthof *et al.* [151] have shown that Fermi level position of perovskite films is highly dependant on the substrate when perovskite film thickness is less than 200nm. More specifically, Miller *et al.* [152] using theoretical and experimental approach has concluded that insulating or n-type substrates shift perovskite Fermi level away from valence band while insulating p-type substrates attract Fermi level closer to the valence band. In order to check if this reasoning may be applicable for ALD NiO_x case, films deposited on different substrates have been analysed by means of UPS. Obtained spectra are presented in Figure 5.9.

  Table 5.7 presents the summary of study about substrate effects on ALD NiO_x UPS result. It is evident that substrate has influence on VBM values and Fermi level position. For instance, NiO_x deposited on n-Si attains highest VBM, which is 1.56 eV, whereas VBM of ALD NiO_x on p-Si is 0.96 eV. This observation is in good correspondence with aforementioned findings that have been reported in Miller *et al.* [152] study. Thus, it may be suggested that NiO_x Fermi level may be pinned by substrate's Fermi level. Additionally, it is seen that substrate has effect on ionization potential.

- **Film thickness**.
  The film thickness may also be a factor responsible for deviations in UPS results. In order to confirm if this is the case, UPS measurements of 50nm sputtered NiO_x films deposited on

Table 5.6: Overview of nickel oxide ionization potential and valence band maximum values measured by UPS.

Paper	IP, eV	VBM, eV	Deposition technique	Substrate	Treatment
Zhang et. al [23]	-	0.8	PLD	STO	-
Kim et. al [143]	5.39	0.53	Solution processed	ITO	Air-annealed
Kim et. al [143]	5.35	0.68	Solution processed	ITO	N_2-annealed
Li et. al [145]	5.09	0.59	Sputtered	FTO	Air-annealed
Kwon et. al [146]	5.37	-	Solution processed	ITO	-
Kwon et. al [146]	5.41	-	Solution processed	ITO	O_2 plasma
Wei et. al [144]	-	0.5	Solution processed	FTO	-
Seo et. al [31]	4.93	0.82	ALD	p-Si	-
Huang et. al [147]	5.36	1.09	Sputtered	FTO	-
Yue et. al [28]	5.43	0.84	Solution processed	ITO	Air-annealed
Tengeler et. al [148]	6.04	0.73	Sputtered	n-Si	In-situ
Jiang et. al [142]	5.49	0.24	Solution processed	ITO	
Jiang et. al [142]	4.97	0.36	Solution processed	ITO	Air-annealed
Ratcliff et. al [149]	5.2	0.5	Solution processed	Gold foil	-
Ratcliff et. al [149]	5.7	0.4	Solution processed	Gold foil	O_2 plasma
Greiner et. al [150]	6.43	-	Sputtered	Si	In-situ
Greiner et. al [150]	5.50	-	Sputtered	Si	Air-exposed
Qiu et. al [85]	5.04	0.46	PLD	ITO	-
Qiu et. al [85]	5.13	0.54	PLD	ITO	Air-annealed

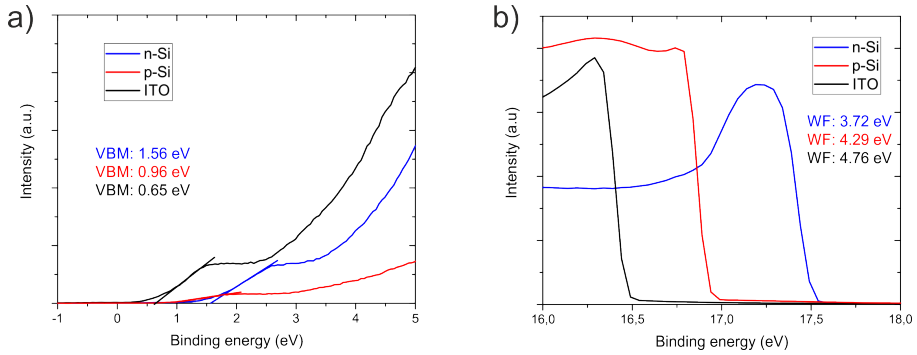

Figure 5.9: a)UPS spectra on-set region of NiO_x deposited on n-Si, p-Si and ITO substrates; b) UPS spectra cut-off region of 10nm thick ALD NiO_x deposited on n-Si, p-Si and ITO substrates.

Table 5.7: UPS results summary of 10 nm thick ALD NiO_x film deposited on different substrates.

Substrate	VBM, eV	WF, eV	IP, eV
n-Si	1.56	3.72	5.28
p-Si	0.96	4.29	5.25
ITO	0.65	4.76	5.41

ITO and Si substrates are performed. Results presented in Figure 5.10 indicate that unlike in 10 nm NiO_x results (see Figure 5.9), VBM and WF values of 50 nm thick films do not differ significantly as in 10nm ALD case. This observation suggests that film thickness may play a role in defining the Fermi level.

- **Oxygen content in NiO_x films**.
  As previously mentioned, ALD NiO_x films are not stoichiometric [133]. Slight variations in x values may have significant influence on the Fermi level position. For instance, in O rich NiO_x films the Fermi level is shifted closer to the valence band and material is p-type

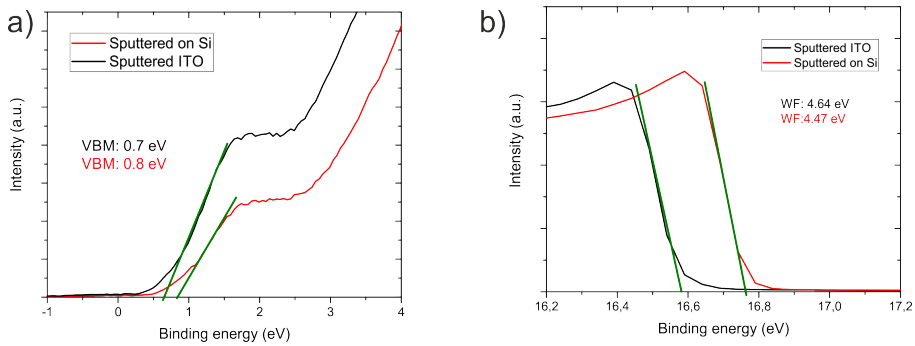

Figure 5.10: a) UPS spectra on-set region of 50 nm sputtered NiO_x films on top of ITO and Si substrates; b) UPS spectra cut-off region of 50 nm sputtered NiO_x films on top of ITO and Si substrates.

because of the holes generated due to excess oxygen atoms. In the case of Ni rich films, NiO_x is n-type [30], due to the free electrons coming from Ni atoms. The variations in stoichiometry may be attributed to differences in deposition conditions and methods.

- **Charging effects**;

UPS measurements are done without electron flood gun, thereby electrons ejected from the NiO_x sample due to photoexcitation are compensated via electrical contact with o-ring form sample holder. Thus, substrate resistivity plays a role in neutralising NiO_x film. If the substrate is resistive so that the flow of electrons from sample holder to NiO_x sample is not sufficient, the NiO_x sample is charged and electric field inside the NiO_x sample is generated. The induced electric field is oriented in such a way that ejected electrons are retarded. Subsequently, this effect results in the shift of the whole UPS spectra to the higher binding energies (see Figure 5.11). More particularly, Figure 5.9 demonstrates that UPS spectra ALD NiO_x on n-Si substrates, which resistivity is the highest (10-20 Ohm-cm) with respect to ITO (10^{-4}-10^{-2} Ohm-cm) and p-Si (1-5 Ohm-cm) substrates, is at the highest binding energy region. Thereby, the charging effect may be considered as a possible reason for dispersed literature results.

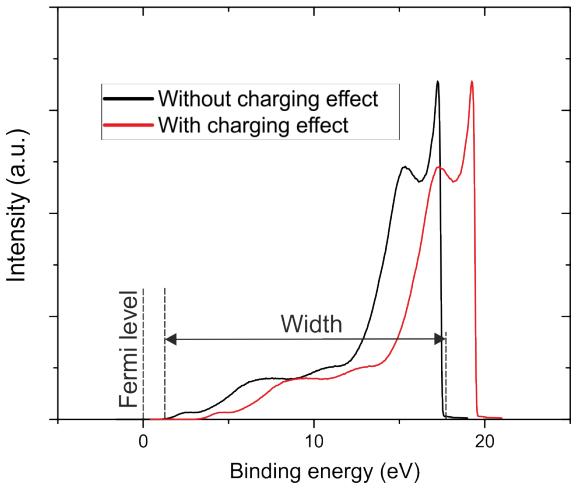

Figure 5.11: Possible influence of charging effect on UPS spectra

5.1.5 Optical properties of pristine NiO_x

NiO_x optical properties are investigated using UV-VIS-NIR spectroscopy. In order to get representative results, NiO_x is deposited on a glass substrate. Then light absorption related to the substrate is minimized. The results of UV-VIS-NIR study on NiO_x ALD films are presented in Figure 5.12. Reflectance and transmittance of NiO_x films are measured by UV-VIS-NIR spectrometer, whereas absorbance is calculated using formula (3.14).

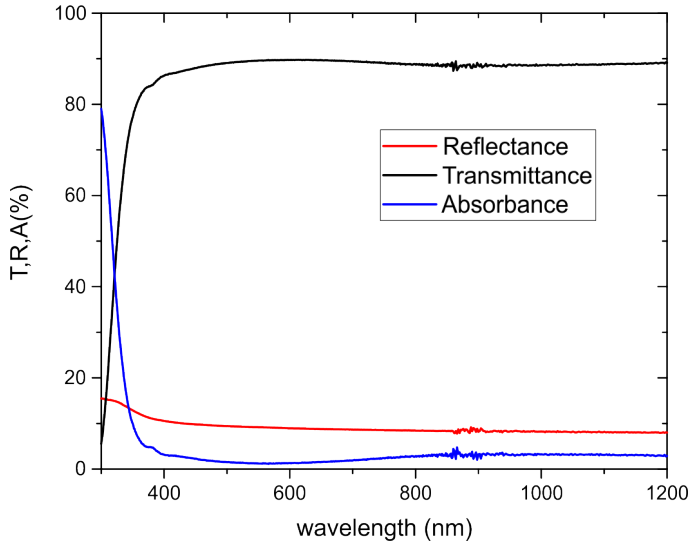

Figure 5.12: Transmittance, reflectance and absorbance spectra of pristine ALD NiO_x.

The graph shows that ALD NiO_x films are highly transparent in the 400-1200 nm wavelength region. On top of that, NiO_x reflectivity in VIS- NIR % region is around 10% and it only reaches 15% in the UV part.These observations are in a good agreement with literature [30],[85],[132]. Futhermore, from UV-VIS-NIR data the optical absorption coefficient of NiO_x films is calculated by formula 3.15. Consequently, NiO_x optical band gap is determined from Tauc's relation 3.16. Since NiO_x has a direct band gap [149],[153],[154], the power factor n in equation 3.16 is 1/2. Obtained Tauc's plot of ALD NiO_x is presented in the Figure 5.13. As it is seen, the estimated band gap value is around 3.8 eV, which is in a good agreement with the literature [30],[149],[154],[155].

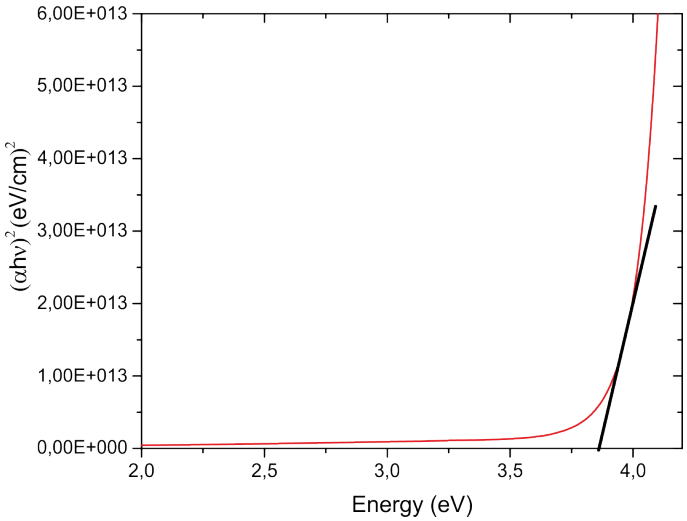

Figure 5.13: Tauc's plot of ALD NiO_x. The band gap is determined by the intersection point between x axis and linear extrapolation line.

5.1.6 Summary

As-deposited NiO_x is polycrystalline, highly transparent, having an optical band gap of 3.8 eV, which makes it a good candidate for a window layer in perovskite solar cells. On top of that, it has been revealed that the ionization potential of as-deposited NiO_x is around 5.4 eV. However, NiO_x films contain some adsorbed water, which can be detrimental for perovskite [52],[53].

5.2 Annealing effects

In this section, the effects of post-annealing treatment on ALD NiO_x material properties are analysed. For this study NiO_x films are annealed in air at 150°C for 1 hour or at 300°C for 20 minutes.

5.2.1 Annealing effects on NiO_x: morphology

In Figure 5.14 the XRD spectra of pristine and annealed ALD NiO_x films are presented. As it can be seen, peak position and structure do not change upon post-annealing. However, there are several studies [30],[85],[136], [156] reporting that ALD NiO_x diffraction peaks shift to higher diffraction angles with post-annealing temperature, which suggests that crystal lattice parameter of post-annealed NiO_x reduces. Thus, findings obtained in this work imply that NiO_x lattice is not affected by the annealing temperature. In addition, the post-annealed NiO_x do not change its preferential orientation and remains (100) oriented. All thing considered, the XRD graphs obtained in this work do not exhibit any noticeable changes, which implies that post-annealing treatment does not change NiO_x morphology.

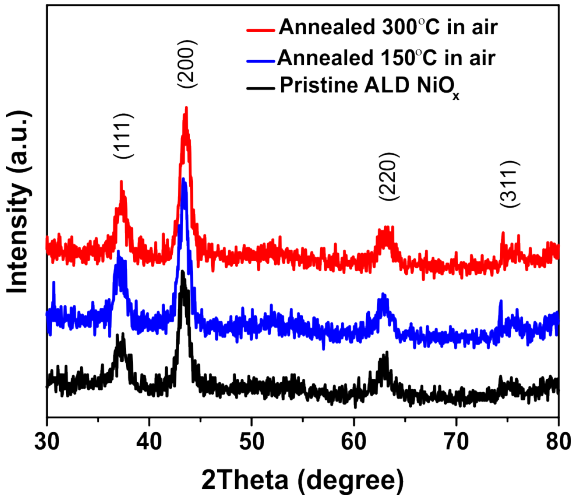

Figure 5.14: XRD spectrum of a) pristine and b) annealed at 300°C 10 nm thick NiO_x samples

5.2.2 Annealing effects on NiO_x: optical properties

In this subsection the post-annealing effects on NiO_x optical properties such as transmittance and optical band gap are presented. The NiO_x transmittance is obtained directly from UV-VIS-NIR spectroscopy measurements. In order to determine NiO_x optical band gap, the procedure, which is presented in the section 5.1.5, is followed. Figure 5.15 presents obtained NiO_x transmittance spectrum and Tauc's plot.

As it is seen in part a) both annealed and pristine NiO_x films are highly transparent in the wavelength region of 300-1200 nm. In fact, the most transparent films are the ones annealed at 300°C, whereas NiO_x annealed at 150°C has the lowest transmittance. Referring to the literature, Tyagi *et al.* [30] and Qiu *et al.* [85] report that transmittance of NiO_x increase systematically with post-annealing temperature due to reduction in native defects and improved film crystallinity. On the other hand, Manceriu *et al.* [133] show that transmittance of NiO_x post-annealed films get lower. This behaviour is associated to the increasing Ni^{3+} concentration. More detailed discussion is presented in the section 5.4.Figure 5.15 b) presents Tauc's plots of pristine and annealed ALD NiO_x films. It is seen that post annealing treatment does not change the band gap, which implies that effective density of energy states in conduction and valence bands is not reduced [30].

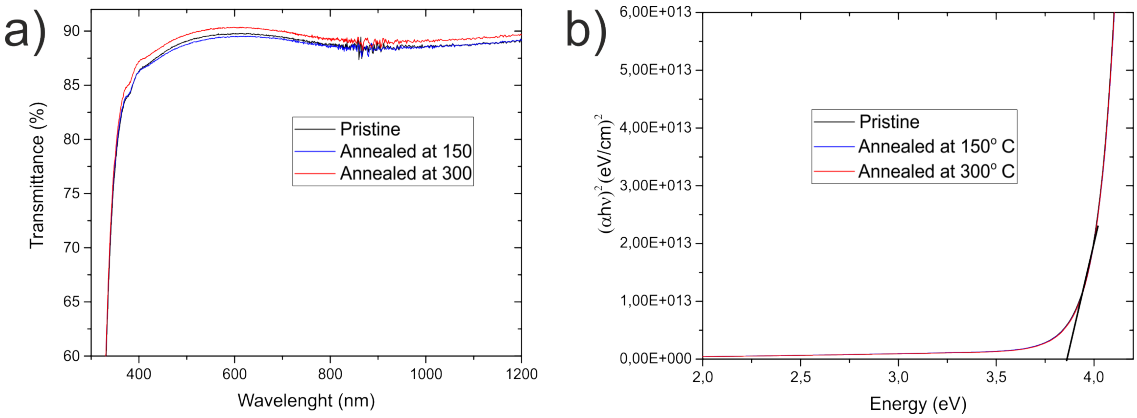

Figure 5.15: In a) ALD NiO_x transmittance and b) Tauc's plot. The linear extrapolation of the edge(black line) indicates the band gap.

5.2.3 Annealing effects on NiO_x: surface chemistry

In this section, the influence of post-annealing treatment on NiO_x surface chemistry is discussed. The cases when NiO_x sample is annealed in air at 150° C for 1 hour and at 300 ° C for 20 minutes are analysed. In order to have higher sensitivity to monitor surface groups, all the spectra are recorded at the take-off angle of 15 °. Figure 5.16 presents the XPS spectra of pristine (Ni $2p_{3/2}$) a) and (O 1s) b), annealed at 150°C (Ni $2p_{3/2}$) c) and (O 1s) d), annealed at (Ni $2p_{3/2}$) 300°C e) and (O 1s) f).

In both Ni $2p_{3/2}$ O 1s spectra (see Figure 5.16) it is evident that the relative intensity of peak attributed to hydroxyl groups diminishes with annealing temperature. In addition to this, the significance of O 1s peak attributed to adsorbed water also reduces, indicating that content of adsorbed water decreases with annealing temperature. Similar trend is observed by Seo *et al.* [31] and Yin *et al.* [86].

Reduction in hydroxyl groups and adsorbed water is also justified by the quantitative XPS analysis. In this case, the integrated areas of Ni$2p_{3/2}$, O1s peaks attributed to NiO, hydroxyl species and adsorbed water are calculated. Afterwards, ratios of hydroxyl groups to NiO and adsorbed water to NiO are calculated. The results of XPS quantitative study are presented in Table 5.8. As it is seen, ratios of hydroxyl groups to NiO and adsorbed water to NiO diminish with annealing temperature. This strongly suggests that hydroxyl groups and adsorbed water are reduced after post-annealing.

Table 5.8: Results of quantitative XPS analysis at take off angle 15°.

	From Ni $2p_{3/2}$	From O 1s	
Sample	hydroxyl groups/NiO	hydroxyl groups/NiO	adsorbed water/NiO
Pristine	3.69	1.13	0.3
Annealed at 150 °C	3.54	1.07	0.2
Annealed at 300 °C	3.21	0.76	0.08

Furthermore, the NiO_x surface chemical composition is analysed by measuring the atomic concentrations of the elements that are present in the film. Unlike in case presented in subsection 5.1.2, NiO_x films are not sputtered with Argon ions, thus surface groups are not eliminated. It is found that the carbon content in the annealed samples, especially in the ones annealed at 300°C, is substantially lower as compared to pristine films (see Table5.9). To sum up, post-annealed NiO_x films have less hydroxyl, adsorbed water and carbon species.

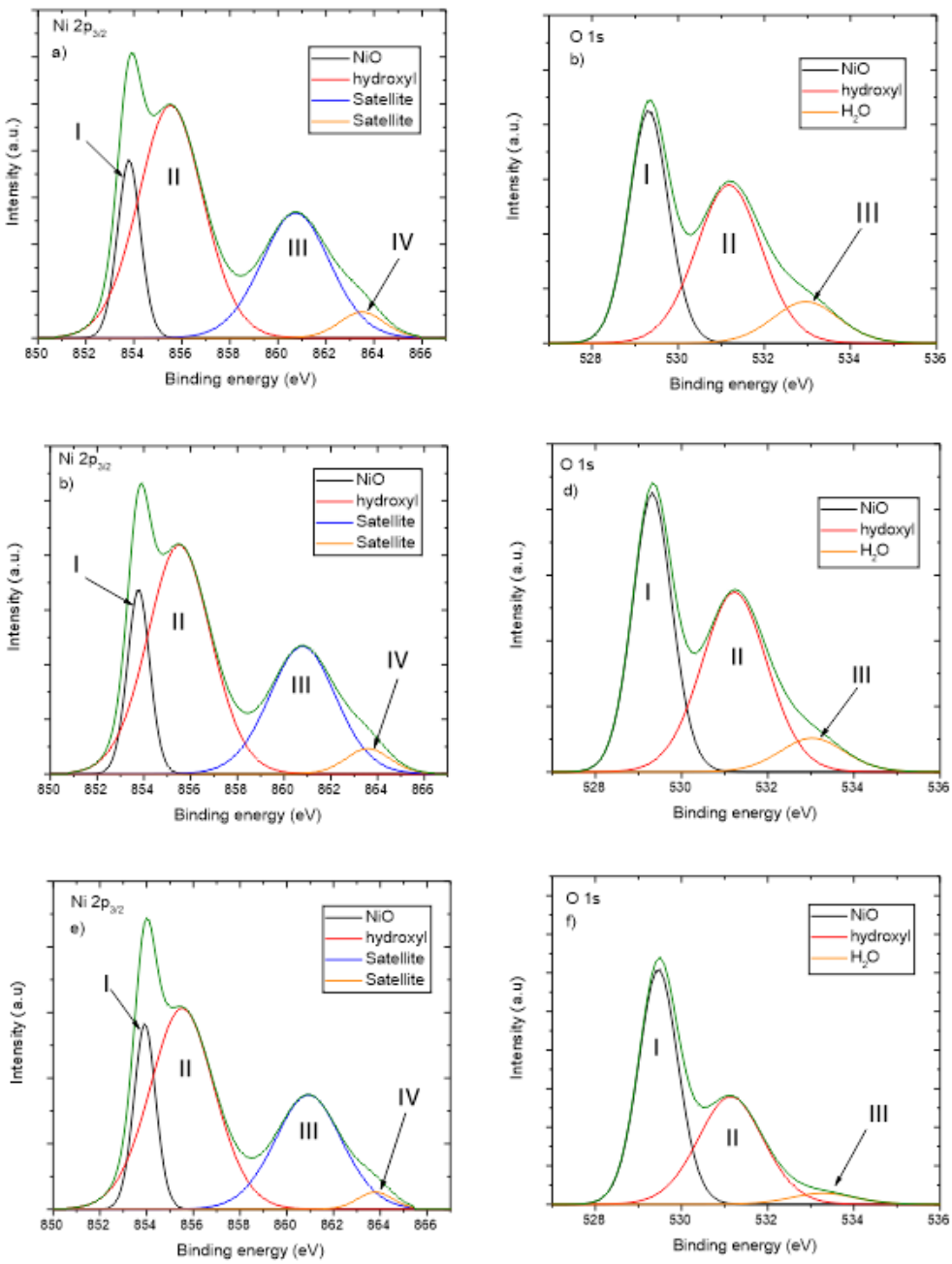

Figure 5.16: ARXPS specta at take-off angle of 15° of ALD NiO_x pristine: a)Ni $2p_{3/2}$, b) O 1s, annealed at 150°C: c)Ni $2p_{3/2}$, d) O 1s NiO_x and annealed at 300°C: e)Ni $2p_{3/2}$, f)O 1s

5.2.4 Annealing effects on NiO_x: energy levels

In order to investigate the annealing effects on NiO_x electronic structure, UPS measurements for three different cases are carried out. Pristine, annealed at 150° C for 1 hour and annealed at 300 ° C for 20 minutes NiO_x samples, which are deposited on ITO substrates, are used for this study. The leading edges of the UPS spectra are extrapolated using third order polynomial technique (detailed description of this technique can be found in subsection 3.2.6). Figure 5.17 a) and b) shows on-set and cut-off regions, respectively. The Fermi level is set to be at 0 eV.

Table 5.9: Atomic concentrations of ALD NiO_x films for three different cases: pristine, annealed at 150°C and at 300°C. All the information is extracted from the data obtained when take-off angle is 15°.

	Atomic concentrations [%]		
Sample	Carbon	Nickel	Oxygen
Pristine	37.03	16.04	46.95
Annealed at 150°C for 1 h	32.47	18.57	48.96
Annealed at 300°C for 20 min	19.91	25.02	55.09

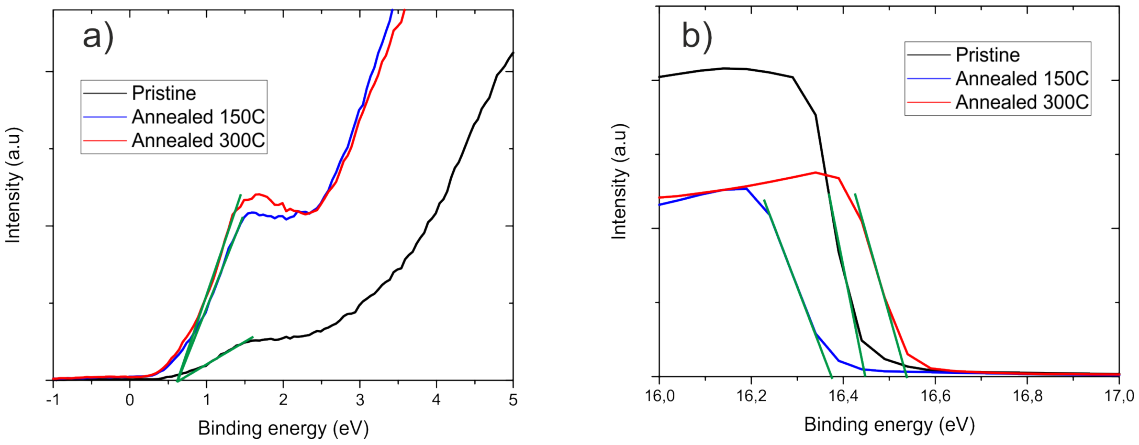

Figure 5.17: On-set a) and cut-off b) regions of NiO_x UPS spectra.

Figure 5.17 a) demonstrates that upon annealing the Fermi level shifts closer to the on-set edge, which represents valence band maximum. The exact valence band maximum values with respect to Fermi level are presented in Table 5.10. Provided the fact that the optical band gap of ALD NiO_x films does not change upon post-annealing (5.15), the shift of Fermi level closer to the valence band implies that NiO_x is more p-type. In fact, these findings are in good agreement with the observations made by Seo *et al.* [31] and Tiagy *et al.* [30]. In both of these studies, it has been suggested that NiO_x is more p-type due to enhanced concentration of nickel vacancies, which result in un-saturated bonds. In order to maintain the charge neutrality in NiO_x films, each nickel vacancy is compensated by two Ni^{3+} ions, which in turn generate holes [149],[150].

Looking at the opposite UPS spectra edge 5.17 b), it is seen that cut-off region of ALD NiO_x post-annealed in the air at 150°C shifts to lower binding energies, which indicates that work function (WF) increases, whereas specimen annealed at 300 °C attains the lowest work function (see table 5.10). Additionally, UPS results show that ionization potential change after post-annealing. The variations in ionization potential may be attributed to the reduction of hydroxyl groups [150]. The more detailed discussion about this phenomenon is available in section 5.4.

Table 5.10: Results of NiO_x UPS measurements.

	WF, eV	IP, eV	VBM, eV
Pristine	4.78	5.46	0.68
Annealed at 150° for 1 hour	4.84	5.49	0.65
Annealed at 300° for 20 minutes	4.67	5.3	0.63

In order to verify ionization potential results obtained by UPS, the APS spectroscopy is utilized. Figure 5.18 shows ion photo-current graphs of ALD NiO_x on n-Si substrate, which are acquired by APS. The ionization potential is determined by extrapolating photocurrent on-set edge to the background level.

APS results indicate that ionization potential grows up with annealing temperature. Initially,

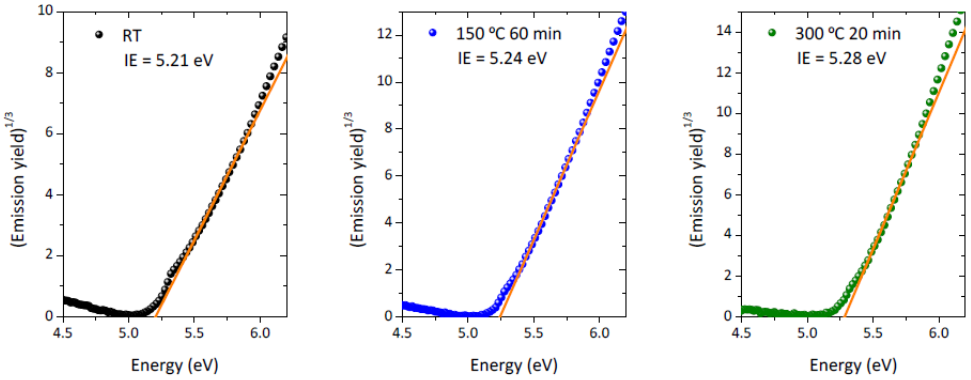

Figure 5.18: Photocurrent graphs of ALD NiO_x obtained by APS.

the ionization potential is 5.21 eV (pristine case) and upon post-annealing, it goes up to 5.28 eV (annealed at 300°C for 20 min case). Summary of the ionization potential determined by UPS and APS is presented in Table 5.11. As it can be seen, ionization potential values are comparable. However, there are small deviations in results, which are expected since experimental conditions during UPS and APS measurements are different. For instance, the probing depth in UPS is higher than in APS due to more energetic incident photon energy (UPS - 21.22 eV; APS from 3 to 7 eV). Furthermore, APS measurements are done under ambient pressure, whereas UPS in ultra-high vacuum. Thus, in APS case the influence of adsorbed surface species is not ruled out. Lastly, in APS case ionization potential is determined from ion photo-current, whereas in UPS from electron kinetic energy spectra. All aforementioned differences considered, in further discussions only UPS results are considered.

Table 5.11: ALD NiO_x ionization potential values obtained by UPS and APS.

	UPS	APS
	Ionization potential, eV	
Pristine	5.46	5.21
Annealed at 150° C	5.49	5.24
Annealed at 300° C	5.3	5.28

5.2.5 Annealing effects on NiO_x: surface wettability

As previously mentioned (see subsection 3.3.1), one of the steps during the manufacturing process of perovskite solar cells is perovskite spin-coating on top of NiO_x. In order to achieve highly efficient solar cells, perovskite layer has to be uniform, pin-hole free. It has been reported that NiO_x wettability behaviour may have an impact on the aforementioned perovskite film features [84]. Therefore, it is important to analyse NiO_x surface wettability behaviour. The study is performed by measuring perovskite solution contact angle with NiO_x surface. Captured images 5.19 reveal that NiO_x surface wettability changes upon annealing. Initially, pristine NiO_x films have good affinity with perovskite solution (see figure 5.19 a)), which is dissolved into ethyl acetate solvent. Subsequently, after annealing at 150° the contact angle of perovskite solution decreases (see figure 5.19 b)), indicating that NiO_x surface has improved affinity with perovskite solution. Lastly, the best wetting conditions are achieved when NiO_x films are annealed at 300°C (see figure 5.19 c)).

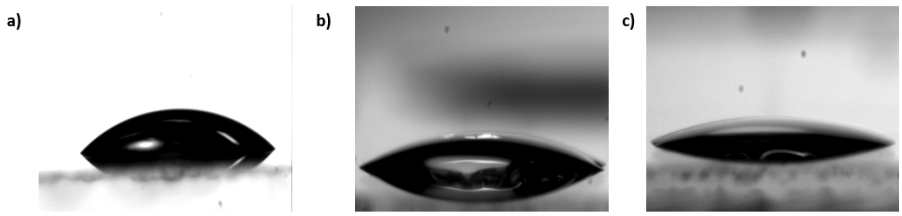

Figure 5.19: Pictures of perovskite solution droplet on pristine a), annealed at 150°C b) and annealed at 300°C NiO_x films.

5.2.6 Summary

In this section it is shown that upon post-annealing NiO_x morphology and optical band gap do not change. In addition, it is revealed that NiO_x samples annealed at 300°C have superior transmittance, whereas NiO_x annealed at 150°C is the least transparent. Moreover, it is shown that upon annealing ionization potential of NiO_x films changes. Along with that, it is observed that Fermi level shifts closer to the valence band, which indicates that NiO_x films become more p-type. Lastly, post-annealing treatment improves NiO_x films' affinity with perovskite solution.

5.3 Perovskite solar cells with ALD NiO_x as a hole transport layer

This section is divided into four parts. In the first part, ALD NiO_x implementation in the perovskite solar cells is discussed. Study about perovskite morphology on pristine and annealed NiO_x films is presented in the second part. The third part focuses on the representative solar cells and their J-V curve behaviour, external quantum efficiency and performance stability. Lastly, the fourth part is devoted to the statistical data of perovskite solar cells based on pristine or annealed NiO_x layers. In order to have more precise and representative results, five batches (≈100) of perovskite solar cells are used for this study.

5.3.1 Implementation of NiO_x in perovskite solar cells

In this work, ALD NiO_x is applied as a hole transport layer in the inverted planar perovskite solar cells. Due to good thermal stability and high absorption coefficient [72] triple cation perovskite $Cs_{0.05}(MA_{0.17}FA_{0.83})_{0.95}Pb(I_{0.83}Br_{0.17})_3$ is employed in these cells. Regarding the electron transport layer, organic C60/BCP (bathocuproine) is used. The principle structure of the analysed solar cell and its cross-sectional image captured by scanning electron microscopy (SEM) are presented in Figure 5.20.

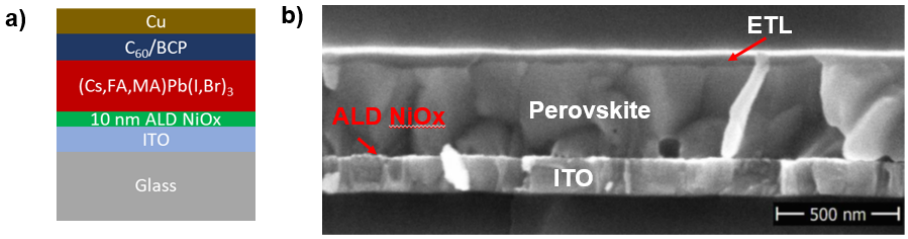

Figure 5.20: Principle scheme a) and cross-sectional SEM image b) of inverted planar perovskite solar cell.

As it can be seen, 10 nm ALD NiO_x is hardly visible in 5.20 b) because of the limited SEM resolution. In order to take a closer look at the ALD NiO_x layer and to check if NiO_x layer is uniform, high-resolution cross-sectional transmission electron microscopy (TEM) image of ALD NiO_x/perovskite interface is captured (see Figure 5.21 a)). Here, it is visible that the NiO_x layer is sandwiched between perovskite (the top dark part of the image) and ITO (the bottom grey part). Clear NiO_x structure suggests that film is crystalline and uniform. Furthermore, TEM image confirms that thickness of NiO_x layer is around 10 nm.

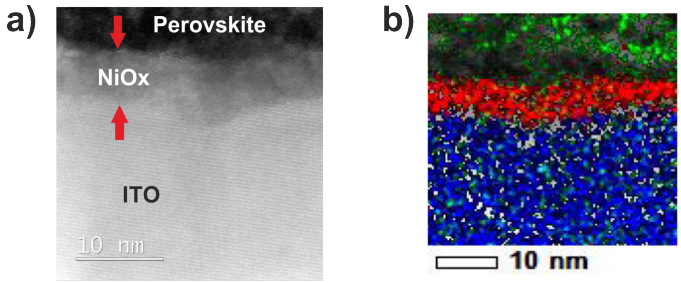

Figure 5.21: a) TEM image of ITO/ALD NiO_x/Perovskite; b)EDX image of ITO/ALD NiO_x/perovskite structure. Green dots represents Pb elements, red corresponds to Ni and blue dots are attributed to In atoms.

In order to verify results obtained from TEM pictures, the energy-dispersive X-ray (EDX)

spectroscopy is used. As previously described in subsection (3.2.10), scanning TEM can be used for EDX. Utilizing this characterization technique high-resolution images of elemental distribution in NiO_x films are obtained. The EDX image of perovskite/NiO_x/ITO structure is presented in the figure 5.21 b). As it can be seen, the distribution of Ni elements (red region) is localized at the interface between ITO (blue region) and perovskite (green region). Therefore, NiO_x films are uniform and compact.

5.3.2 Perovskite morphology on pristine and annealed NiO films

Changes in perovskite morphology may have implications for the optoelectronic features. For instance, the band gap of perovskites having contracted lattices is smaller than of perovskites with undistorted lattices [47]. Thus, it is crucial to investigate perovskite morphology and monitor any changes in lattice parameters. In order to reveal if perovskite crystallizes differently on pristine and annealed NiO_x samples, XRD measurements are performed. Figure 5.22 shows diffractograms of perovskite deposited on pristine and annealed NiO_x films. As it can be seen, XRD spectrum consists of typical triple cation perovskite diffractogram [157] and two additional not perovskite related peaks. The first peak at around 13° is attributed to PbI_2, which may be formed due to excess of lead and iodine in the perovskite solution. The second peak at around 30∘ represents ITO because perovskite/NiO_x/ITO stacks are used for XRD measurements and some X-rays penetrate through perovskite, NiO_x films and diffract from ITO substrate. NiO_x diffraction peaks are not visible because of relatively small NiO layer thickness. Comparing XRD spectra of perovskite on pristine and annealed NiO_x, no changes in peak intensities and positions are observed. These observations suggest that the crystallinity and morphology of the perovskite film are not depending on the NiO_x conditions and change in solar performance are not associated with perovskite bulk properties.

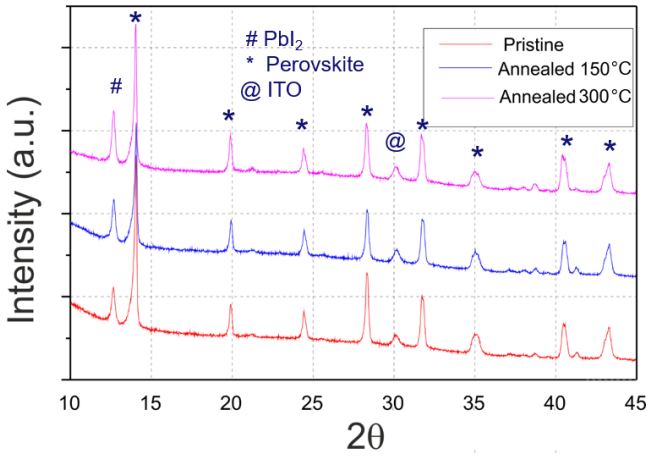

Figure 5.22: XRD of triple cation perovskite on pristine and annealed NiO_x.

To further confirm that perovskite morphology is not affected by the NiO_x post-annealing, the top view images of perovskite films are captured using SEM. Obtained images (see figure 5.23) indicate that perovskite film is crystalline with clearly visible dark grey grains, which regardless of NiO_x conditions have comparable size. Additionally, images display small light grey particles located at the grain boundaries between perovskite crystals. These small crystallites are attributed to excessive PbI_2 [158], which presence is also detected by XRD measurements. All things considered, results of XRD and SEM analyses reveal that perovskite morphology is not changing by post-annealing NiO_x films.

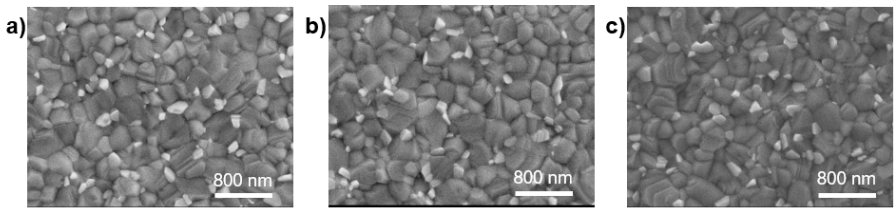

Figure 5.23: Top view SEM images of triple cation perovskite on a) pristine, b) annealed at 150°C and c) annealed at 300°C NiO_x

5.3.3 Representative Perovskite Solar Cells Performance Data

In this subsection (J-V), EQE and MPP results of perovskite solar cells (active area 0.1 cm^2) based on pristine, annealed at 150° or at 300°C are presented. Figure 5.24 a) shows (J-V) curves. Here, solid lines represent results which have been recorded in forward scan (from J_{SC} to V_{OC}) and dashed lines correspond to reverse (J_{SC} from V_{OC}) scan direction.

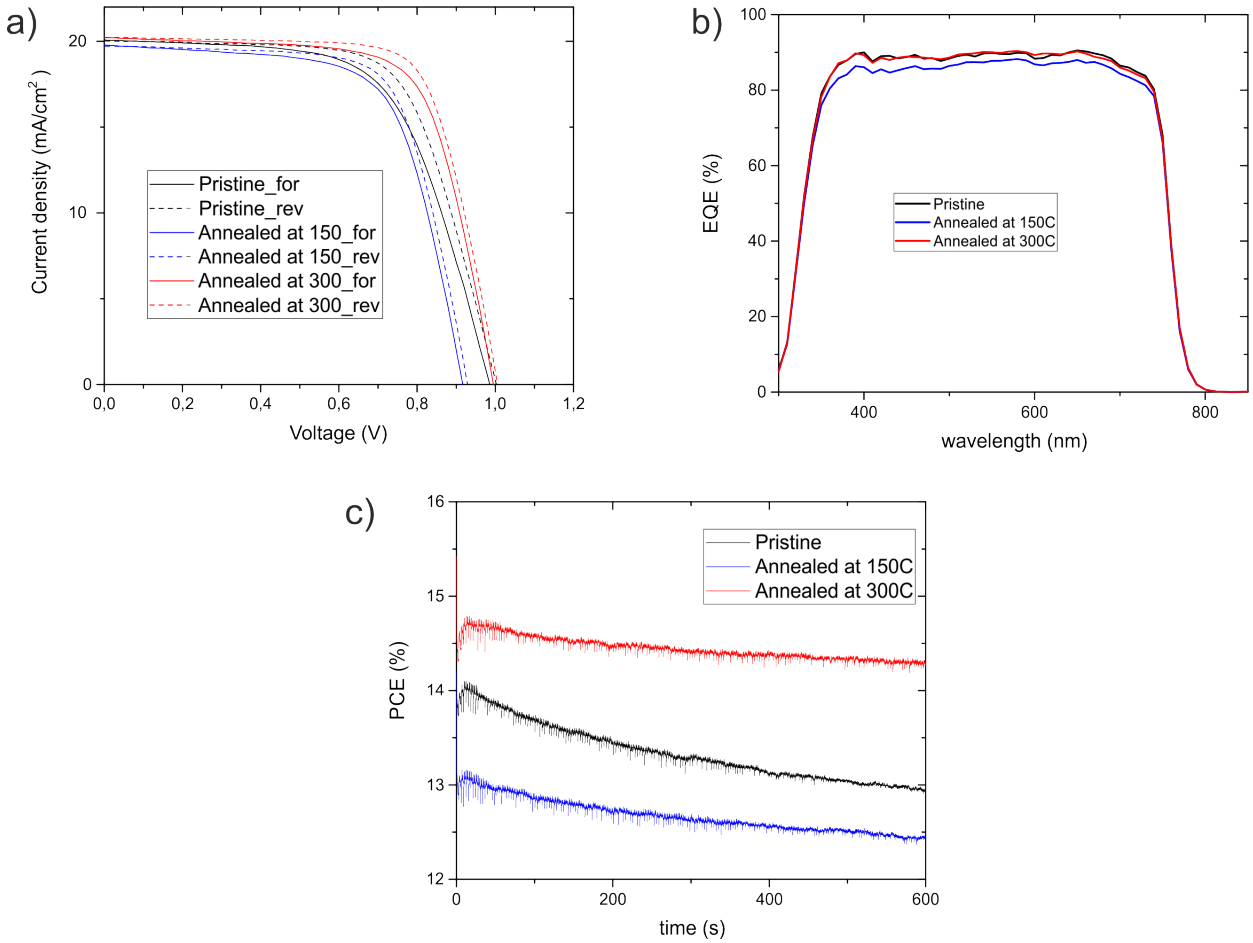

Figure 5.24: a) J-V curves of pristine and annealed cases. Reverse and forward scans are marked with dashed and solid lines, respectively. b) EQE of perovskite solar cells with pristine and annealed ALD NiO_x films. c) MPP tracking data.

As it can be seen the shape of J-V curve depends on the scan direction, which means that solar cells exhibit hysteresis behaviour. In fact, J-V results show that the extent of hysteresis is reduced with NiO_x annealing temperature. Similar trend is observed by Seo *et al.* [31]. Here, it has been proposed that hysteresis is mitigated due to higher NiO_x conductivity, which has been achieved by post-annealing NiO_x films. However, in this study NiO_x has not been characterized from an electrical point of view, thus reasons of reduced hysteresis are speculative.

Additionally, it is observed that slope of (J-V) curve in V_{OC} region becomes steeper with annealing temperature. Shape of (J-V) curve depends on device resistance (refer to subsection 3.3.2). More specifically, solar cells having lower series resistance exhibit J-V curve having steeper slope in V_{OC} region. Tangents of (J-V) curves in V_{OC} region have been calculated and results are presented in Table 5.12. Following the relation:

$$\frac{dI}{dV} \propto \frac{1}{R_S} \tag{5.1}$$

,obtained tangent values suggest that solar cells based on post-annealed NiO_x films have smaller series resistance. In addition to that, J-V curves show that NiO_x post-annealing treatment improves J_{SC} and V_{OC} of perovskite solar cells. More information about this is presented in the next subsection 5.3.4.

Table 5.12: Calculated tangent values in V_{OC} region of (J-V) curves recorded in forward direction.

Sample	Pristine	Annealed at 150°C	Annealed at 300°C
Tangent	81	123	128

In order to have a better understanding about the changes in J_{SC}, the external quantum efficiency (EQE), which by definition is a ratio of the number charge carriers collected by the solar cell to the number of incident photons at given energy, is measured. The EQE graphs are presented in Figure 5.24 b). It is seen that on-set region (300nm), which mainly depends on the window layer thickness and optical band gap, and the cut-off region (800 nm), which is determined by the perovskite band gap ($\approx$ 1.64 eV), do not shift upon annealing. This confirms that NiO_x optical band gap does not change upon annealing (see subsection 5.2.2) and suggest that perovskite band gap is also not affected by NiO_x annealing. Moreover, it is observed that in the whole UV-VIS-NIR (300-800nm) region EQE of solar cells based on NiO_x annealed at 150°C is lower compared to two other cases. This downward shift in EQE may be attributed to the reduced NiO_x transmittance (see subsection 5.2.2).

Perovskite solar cell performance stability is determined from maximum power point (MPP) tracking graphs, which are presented in Figure 5.24 c). The MPP tracking graph is recorded for for 10 minutes. As it is observed, PCE of perovskite solar cells with pristine NiO_x drops the most. In contrast, the PCE of the solar cells with NiO_x annealed at 300°C reduces the least. Improved PCE stability suggests that interface between NiO_x and perovskite is more stable upon post-annealing, which is attributed to the reduced adsorbed water concentration on post-annealed NiO_x surface (see subsection 5.2.3).

5.3.4 Statistical Data of Perovskite Solar Cells Performance

This subsection represents statistical data of perovskite solar cells performance parameters depending on the NiO_x conditions: pristine, annealed in air at 150°C for 1 hour and annealed in air at 300°C for 20 minutes. Since perovskite solar cells are sensitive to manufacturing conditions and thus may have limited reproducibility, 5 batches consisting of more than 100 solar cells are used for this study in order to get representative results. The statistical data of devices, which active area is 0.1 cm^2, is presented in box charts (refer to Figure 5.25). Here, a single measurement represents one data point. All pixels inside the box are between 25 % and 75 % percentiles. The median value of each data set is marked with a dash.

Figure 5.25 a) shows that FF increases systematically with ALD NiO_x annealing temperature. According to the fundamentals of the solar cells (see subsection 3.3.2.), FF depends on series R_s and sheet R_{sh} resistance. Efficient solar cells have high FF which is associated with low series R_s and high sheet R_{sh} resistance. Actually, in previous section it has been demonstrated that R_s gets reduced (see Table 5.12) with annealing temperature. Considering this finding along with the post-annealed NiO_x material properties (see section 5.2), the increase in FF may be attributed to the factors, which are listed below.

- **Annealed NiO_x films are more p-type and attain lower resistance**.

  Observed downward Fermi shift (see subsection 5.2.4) implies that carrier (hole) concentration in annealed NiO_x films is higher, which may lead to better conductivity and lower device resistivity. In fact, *J-V* results indicate that perovskite solar cells based on annealed NiO_x films exhibit lower series resistance.

- **Annealed NiO_x films have better affinity with perovskite solution**.

  Improved NiO_x surface wettability may lead to a better electrical contact between perovskite and NiO_x films. Along with that its reported that improved wettability behaviour may prevent pin-hole formation in perovskite film [82], [84] .

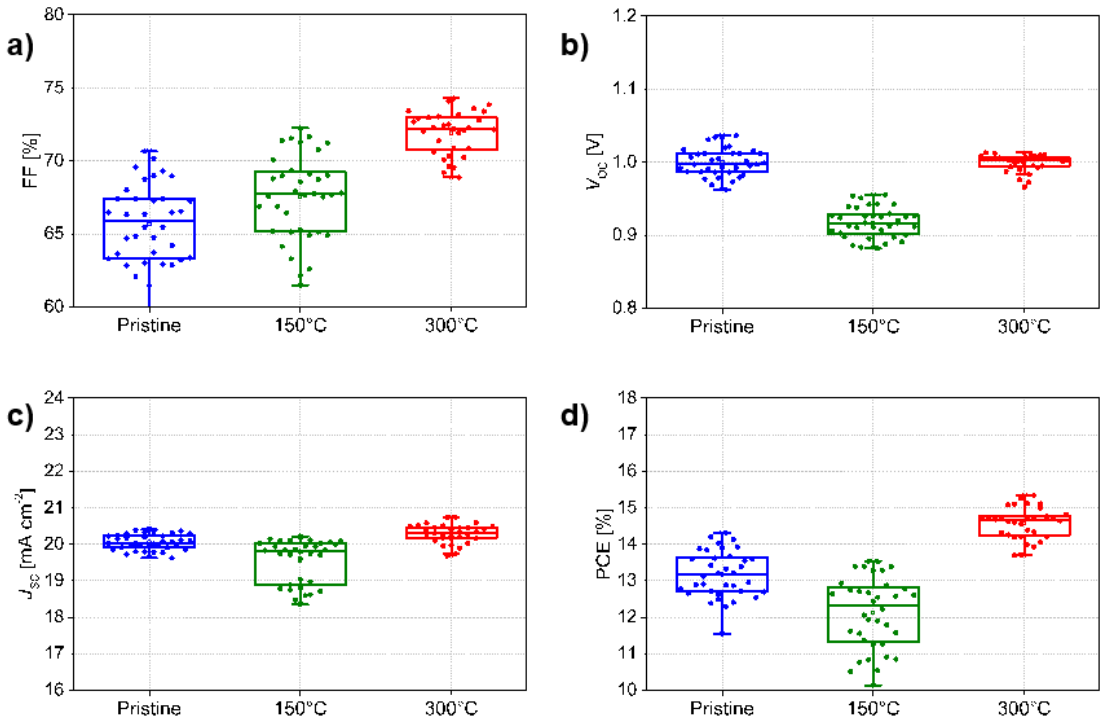

Figure 5.25: Box plot of solar cells performance. The median values are marked with dash inside the box. Plot: a) shows FF, b) presents V_{OC} , c) demonstrates J_{SC} and d) PCE.

Figure 5.25 b) indicates that post-annealing does not improve V_{OC}. In fact, perovskite solar cells with NiO_x annealed at 150°C have the lowest V_{OC} value. From studies reported in literature [82],[83] it is known that higher V_{OC} is attained when NiO_x valence band is in a good alignment with the perovskite valence band. In order to check if this is the case in this work, the ionization potential of triple-cation perovskite is determined by means of UPS. Figure 5.26 demonstrates that UPS spectral width is 15.17 eV. Considering that incoming photon energy is 21.22 eV, it follows that ionization potential is 6.05 eV.

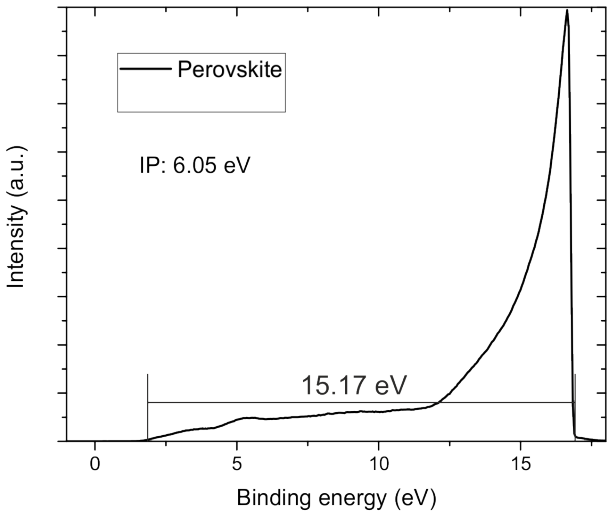

Figure 5.26: UPS spectrum of perovskite. The width is measured from on-set to cut-off energies.

Combining this and ALD NiO_x UPS results which are presented in subsection 5.2.4, energy band diagram of NiO_x and triple cation perovskite is made (see Figure 5.27). Here, it is considered that the vacuum level is constant. As it can be seen, the best valence band alignment is obtained in case of post-annealed NiO_x at 150°C. However, the V_{OC} of perovskite solar cells having films annealed at this conditions is the lowest. Thereby, there are other factors, which lead to a reduction in V_{OC}. For instance, according to Schockley-Queisser detailed balance limit [159], V_{OC} of the solar cells depends on the fraction of radiative recombination to the total recombination. In solar cells with high V_{OC} radiative recombination is dominant, which means that non-radiative recombination pathways are suppressed V_{OC}. Thus, the lower V_{OC} of the perovskite solar cells with NiO_x annealed at 150°C may be due to enhanced non-radiative recombination [160] at the NiO_x/perovskite interface.

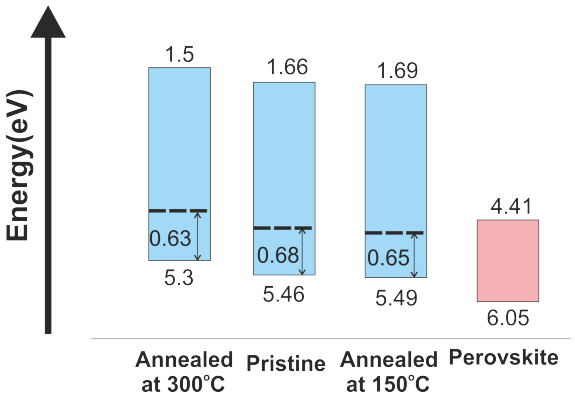

Figure 5.27: The principle energy band diagram of perovskite and ALD NiO_x. For each case ionization potential values are given at bottom of rectangles, whereas electron affinity values are shown at the top of rectangles. Dashed line demonstrates Fermi level and the valence band maximum values are placed inside rectangles.

The J_{sc} results of perovskite solar cells having annealed and pristine NiO_x are presented in

Figure 5.25 c). As it can be seen, highest J_{SC} values are achieved by perovskite solar cells with NiO_x annealed at 300° C, whereas perovskite solar cells utilizing NiO_x annealed at 150° C exhibit lowest J_{SC} values. Considering that NiO_x is a window layer in the analysed perovskite solar cells, J_{SC} may be influenced by NiO_x transmittance. Study of annealing effects on NiO_x optical properties(see subsection 5.2.2) has revealed that NiO_x is the most transparent when annealed at 300°C and has the lowest transmittance when annealed at 150° C. These findings correlate with J_{SC} results, suggesting that drop in J_{SC} may be attributed to the reduction in NiO_x optical transmittance.

Most importantly, PCE of perovskite solar cells can be improved upon post-annealing NiO_x. In figure 5.25 d) it is observed that the perovskite solar having NiO_x annealed at 300°C are the most efficient. The median values of solar cells performance parameters are presented in Table 5.13. Improvement in PCE is mainly attributed to the increased FF, since J_{SC} and V_{OC} of perovskite solar cells having pristine or annealed at 300° C NiO_x films are comparable. In this work, champion cell yields a J_{SC} of 20.73 mA/cm^2, V_{OC} of 1.005 V, FF 0.7357 and PCE 15.33%.

Table 5.13: Median values of perovskite solar cell performance parameters.

Annealing temperature (° C)	V_{OC} (V)	J_{SC} (mA cm^{-2})	FF (%)	PCE(%)
As-deposited	0.997	20.03	65.88	13.15
150	0.916	19.80	67.72	12.32
300	1.002	20.31	72.20	14.66

5.3.5 Summary

In this section it is reported that ALD NiO_x films incorporated in perovskite solar cells are uniform and compact. More importantly, it is shown that by post-annealing NiO_x films efficiency of perovskite solar cells can be improved. The enhancement in performance is attributed to the higher FF and J_{SC}. The obtained champion perovskite solar cell PCE is 15.33%.

5.4 Hypothesis about annealing effects on NiO_x

This section introduces possible reasons why upon annealing NiO_x ionization potential increases, why films change their transmittance upon annealing and why surface wettability properties are affected.

5.4.1 Hydroxyl groups and higher nickel oxides

In section 5.2.3 it is pointed out that ALD NiO_x contains hydroxyl groups, which consist of nickel hydroxides ($Ni(OH)_2$) and nickel oxy-hydroxides (NiOOH). These species have closely overlapping binding energies [36], [136],[161] therefore it is common to assign both hydroxyl species to single XPS peak [31]. Due to broad peak formation and overlapping bind energies, XPS have limited capabilities to monitor individual changes in $Ni(OH)_2$ and NiOOH. Interestingly, these species play a different role in NiO_x films owing to their opposite features, which are listed below:

- **Electrochromic features**.

  Hydrous nickel oxide is an electrochromic material, which means that the colour of hydrous nickel oxide changes with Ni oxidation state. Thereby, nickel hydroxide ($Ni(OH)_2$) is a highly transparent state in the visible region, whereas nickel oxy-hydroxide (NiOOH) has a bronze tint and absorbs light in the visible part of spectrum [162],[163]. Considering this dual nature of hydrous nickel oxide, the reduction in transmittance of NiO_x films annealed at 150°C may be attributed to the enhanced concentration of NiOOH species.

- **Wettability behaviour**.

  NiOOH and $Ni(OH)_2$ have different influence on NiO_x surface wettability. In experimental [164] and theoretical [165] *et al.* studies it is revealed that due to the weak interaction between $Ni(OH)_2$ and water molecules, surfaces terminated by $Ni(OH)_2$ are hydrophobic. The opposite wettability behaviour is observed for surfaces terminated by NiOOH species, which have strong dipole moment. Therefore, NiOOH terminated surfaces are not thermodynamically stable and water easily adsorbs on these surfaces, which means that surfaces terminated by NiOOH are hydrophilic. Considering that in this work perovskite solution is dissolved in ethyl acetate (see subsection 3.3.1), which is polar solvent like water, NiOOH and $Ni(OH)_2$ species may have similar effect on determining NiO_x surface affinity with perovskite solution.

- **Influence on ionization potential**.

  It has been reported that ionization potential of NiO_x films having species $Ni(OH)_2$ is lower compared to clean NiO_x surface [150]. In contrast, Ratcliff *et al.* [149] and Manders *et al.* [136] report that increase in NiOOH species results in higher ionization potential. This behaviour is attributed to the fact that NiOOH has strong dipole momentum and deep valence band [149]. Referring to UPS study results presented in subsection 5.2.4, higher ionization potential and downward Fermi level shift of NiO_x sample annealed samples may be attributed to the reduction in $Ni(OH)_2$ and increase in NiOOH species.

Additionally, in literature it is documented that at temperatures above 250°C hydroxyl groups may be converted to higher order oxides, such as Ni_2O_3,[166], [167]. The binding energies of Ni and O elements in Ni_2O_3 are overlapping with $Ni(OH)_2$ and NiOOH species (see Table C.1). Thus, it is hard to discern Ni_2O_3 by means of XPS analysis. However, Ni_2O_3 is an intrinsic p-dopant [149] in NiO_x films, thus downward Fermi level shift in case of NiO_x films annealed at 300°C may be caused by an increase in Ni_2O_3 species. Nonetheless, in order to confirm this hypothesis further theoretical and experimental investigations need to be carried out.

Chapter 6

Conclusions and Recommendations

6.1 Conclusions

In this thesis it has been demonstrated that using $Ni(MeCp)_2/O_2$ plasma chemistry NiO_x films can be deposited. Material characterization revealed that ALD NiO_x have desired properties to be implemented as hole transport layer in perovskite solar cells. Furthermore, ALD NiO_x films have been post-annealed at 150 °C or 300°C, in order to investigate relation between NiO_x interface properties and perovskite solar cell performance. The main conclusions of this work consist of answers to the research questions, which have been presented in the introduction of this report. Furthermore, several recommendation for further investigations are provided, which may provide deeper insight into post-annealing effects.

1. **What is the performance of perovskite solar cells utilizing pristine atomic layer deposited nickel oxide?**

   In this work, it has been shown that inverted planar perovskite solar cells having structure Ag/BCP/perovskite/ ALD NiO_x/ITO/Glass with pristine ALD NiO_x layer yields a J_{SC} of 20.03 (mA/cm^2), V_{OC} of 0.997 (V), FF of 65.88 (%) and PCE of 13.15 (%). These performance parameters are comparable with the previously reported studies on ALD NiO_x for perovskite solar cells [31],[32]. Thereby, plasma-enhanced ALD NiO_x films deposited at 150°C utilizing a $Ni(MeCp)_2/O_2$ plasma chemistry are suitable to be implemented as a hole transport layer in perovskite solar cells.

2. **How are the bulk/interface material properties of atomic layer deposited nickel oxide affected by post-annealing?**

   - Bulk properties.

     In this work, as-deposited ALD NiO_x is polycrystalline, highly transparent (∼85%) in the wavelength region of 400-1200 nm. It has been revealed that the crystallinity and morphology of post-annealed ALD NiO_x films do not change. Additionally, it has been found that the optical band gap of ALD NiO_x films does not change upon-post annealing. However, NiO_x optical transmittance is affected by annealing temperature. In the case of post-annealing at 150°C, NiO_x films are less transparent with respect to pristine, whereas films annealed at 300°C attain the highest transparency.

   - Interface properties.

     In this work, it has been shown that ALD NiO_x films deposited at 150°C contain hydroxyl groups. Results of angle resolved XPS have revealed that concentration of these species is higher at the surface.It has been found that hydroxyl groups are reduced

after post-annealing treatment. Furthermore, employing UPS technique, it has been demonstrated that post-annealing treatment has an influence on ALD NiO_x electronic structure. More particularly, it has been shown that Fermi level shifts closer to valence band with annealing temperature, which implies that post-annealed ALD NiO_x layers are more p-type. Accompanied with this finding, it has been shown that ALD NiO_x valence band position (ionization potential) is affected by post-annealing temperature. However, the change in ionization potential is not systematic. ALD NiO_x annealed at 150 °C have deepest valence band, whereas samples annealed at 300° have lowest ionization potential. Additionally, it has been demonstrated that wettability behaviour of ALD NiO_x improves upon post-annealing.

3. **How is the perovskite solar cell performance affected by NiO_x annealing?**

   In this work, statistical data of solar cell performance have shown that perovskite solar cells based on ALD NiO_x annealed at 300°C have the highest performance parameters. The champion cell exhibit a J_{SC} of 20.73 (mA/cm^2), V_{OC} of 1.005 (V), *FF* of 73.57 (%) which in turn translates into *PCE* of 15.33%. Since it has been shown that perovskite film crystallinity and quality is not affected by NiO_x annealing conditions, the improvement in solar cell performance has been solely attributed to changes in the interface of NiO_x/perovskite and NiO_x material properties. More specifically, the enhancement in perovskite solar cell performance has been attributed to reduction of surface hydroxyl groups, to better perovskite wetting on post-annealed ALD NiO_x films and to more p-type NiO_x films upon post-annealing treatment. Additionally, it has been found that perovskite solar cells performance stability improves with annealing temperature. It is attributed to reduced adsorbed water content on the ALD NiO_x surface.

   Notably, efficiency of perovskite solar cells based on ALD NiO_x annealed at 150°C exhibit the lowest performance in comparison to solar cells having pristine and annealed NiO_x films, even though the off-set between perovskite and ALD NiO_x valence bands is the lowest 0.55 eV, whereas in solar cells based on pristine and annealed at 300°C it is 0.58 eV and 0.74 eV, respectively. These observations strongly suggest that NiO_x valence band alignment with perovskite is not sufficient to have efficient solar cells.

6.2 Recommendations

- **To Perform Time Resolved Photoluminescence Measurements**

  This characterization technique will provide more information about the ALD NiO_x annealing effects on solar cell performance. Applying this method hole extraction rate can be measured. Good hole transport layers extract generated charges quickly so that the photoluminescence (PL) effect is quenched rapidly. Better charge extraction at the ALD NiO_x/perovskite interface layer may be a cause of higher J_{SC} and FF [84], [85]. Thereby, time-resolved PL measurements will be useful to elucidate possible reasons for improved *FF* and J_{SC}, that are observed in this study.

- **To Investigate Opportunities for Doped ALD NiO_x**

  In chapter 2, subsection 2.2.3 it is pointed out that perovskite solar cells based on doped NiO_x films exhibit superior performance due to improved electrical conductivity. Hitherto, there no publications reporting solar cells having doped ALD NiO_x films. Thereby, it is worth to discover doped NiO_x ALD chemistries and processes. Presumably, doped ALD NiO_x (Cu:NiO_x, Cs:NiO_x, Ag:NiO_x and etc.) films may have better conductivity and positive effect on solar cell performance.

- **To Perform Solar Cell Stability Measurements**

  In chapter 2 it is pointed out that perovskite solar cells have poor environmental stability. However, in this work, solar cell stability has not been the main focus of investigations.

Thereby, in further research, it is important to address this question more thoroughly and systematically by analysing light-induced, humidity-induced and heat-induced degradation processes in perovskite solar cells based on ALD NiO_x.

Appendix A

Photo-Absorber Band Gap Determination from EQE

On-set edge of the EQE graph in the longer wavelength region is directly related to the band gap of the photo-active layer in solar cells. Applying expression:

$$\left(h\nu * ln(1 - EQE)\right)^2 \tag{A.1}$$

, the band gap of photo-active layer is determined by extrapolating the on-set edge of curve which is obtained using formula presented above. Example of CZTS solar cell is presented in Figure A.1.

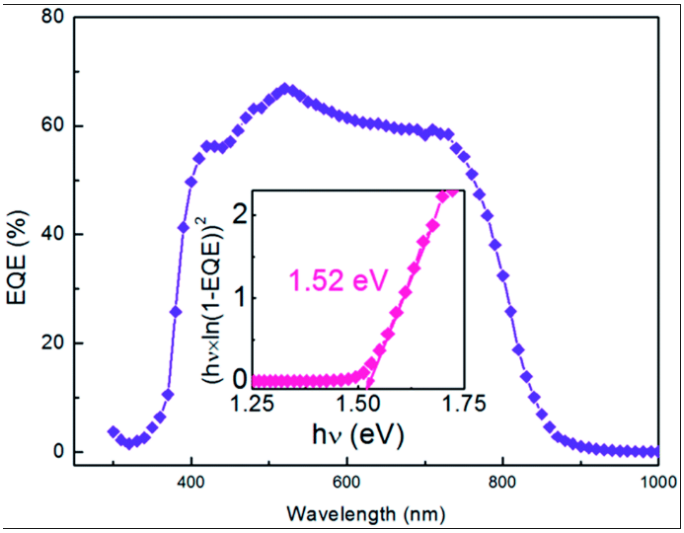

Figure A.1: EQE of CZTS solar cell and inset demonstrates the band gap of CZTS thin film obtained from EQE graph. Adopted from [168].

Appendix B

NiOx Surface Topology

In order to have a deeper insight into the interface, the NiOx surface topology is analysed. The atomic force microscopy (AFM) in tapping mode is used to investigate surface morphology. The pristine and annealed at 300°C NiOx samples, which are deposited on a silicon substrate, are investigated. Acquired surface topology pictures are presented in the figure B.1. From both a) pristine and b) annealed samples it is seen that NiOx film is uniform, pin-hole free film. Moreover, it is evident that there is no significant change in surface structure after post-annealing. This corroborates with XRD results 5.1, which suggest that crystallization degree is not higher after post-annealing treatment.

In quantitative surface topology analysis, the surface roughness (R_q) parameter is used. Conventionally, the surface roughness is defined as the root mean square (RMS) average of height deviations from mean measured data plane. Mathematically, this parameter is expressed as follows:

$$R_q = \sqrt{\frac{\sum_i Z_i^2}{N}} \tag{B.1}$$

,where Z_i is the height of i point and N total number of points. The Rq value is calculated using *Nanoscope* software. The obtained R_q values for a scan size of 330 nm are presented in the table B.1. It is seen that surface roughness of both samples is less then 1 nm, which means that surfaces are extremely flat and there is no change roughness upon post-treatment.

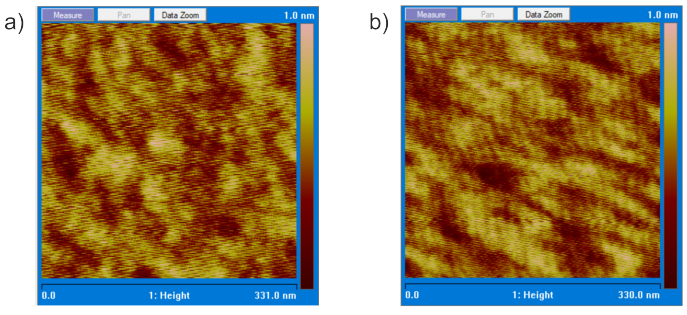

Figure B.1: AFM of NiOx a) pristine and b) annealed at 300°C

Table B.1: Surface roughness

Sample	Dimensions, nm	R_q, nm
Pristine	331	0.188
Annealed at 300°C for 1 hour	330	0.172

Appendix C

Binding Energies of Oxygen 1s and Nickel $2p_{3/2}$ Electrons in NiOx

The table below summarizes the reported binding energies for O 1s and Ni $2p_{3/2}$ electrons in NiOx.

Table C.1: Binding energies of oxygen 1s and nickel $2p_{3/2}$ electrons in NiOx

Paper	Chemical environment	O 1s, eV	Ni 2p 3/2, eV
Zhu et. al [131]	NiO	529.2	853.7
	NiOOH	531.9	855.5
Bodiu Islam et. al [132]	NiO	-	853.8
	NiOOH, Ni_2O_3	-	855.5
Cao et. al [137]	NiO	529.1	853.7
	NiOOH	531.6	856.2
	Ni_2O_3	531.1	855.5
Yin et. al [154]	NiO	-	853.6
	NiOOH	-	856.2
	Ni_2O_3	-	855
Ratcliff et. al [149]	NiO	529.7	854.7
	NiOOH	531.8	856.4
	$Ni(OH)_2$	531.1	854.7
Seo et. al [31]	NiO	529.5	854.1
	Defects, surface groups	531.6	856
Soo Kim et. al [36]	Ni^{2+}	-	854.5, 856
	Ni^{3+}	-	856.1
Chen et. al [81]	Ni^{2+}	529.6	854
	Ni^{3+}	531.4	856
Manceriu et. al [133]	Ni^{2+}	-	853.9
	Surface groups	-	856.1
	Ni^{3+}	-	855.3
Hsu et. al [87]	Ni^{2+}	529.6	853.9
	Ni^{3+}	531.4	855.7
Shim et. al [88]	NiO	529.4	853.9
	$Ni(OH)_2$	531.3	855.6
Manders et. al [136]	NiO	529.2	853.7
	Ni_2O_3,$Ni(OH)_2$, NiOOH	531.0	855.5
Greiner et. al [150]	NiO	529.4	853.9
	Ni_2O_3,$Ni(OH)_2$	530.6	855.6

Bibliography

[1] Iae: Key world energy statistics 2017. https://www.iea.org/publications/freepublications/publication/KeyWorld2017.pdf. Accessed: 2018-08-16. 1

[2] Dutch review: Last night was the hottest night ever in the netherlands. https://dutchreview.com/news/weather/last-night-was-to-hottest-night-ever-in-the-netherlands/. Accessed: 2018-08-10. 1

[3] Nasa: Global climate change. https://climate.nasa.gov/vital-signs/global-temperature/. Accessed: 2018-08-10. 1

[4] Richard Perez and Marc Perez. A fundamental look at energy reserves for the planet. 50, 2009. 1

[5] REN21. Renewables 2018 global status report. Technical report, Paris, 2018. 1, 2

[6] Gavin Conibeer et al. Third-generation photovoltaics. *Materials today*, 10:42–50, 2007. 2

[7] Fraunhofer photovoltaics repor. https://www.ise.fraunhofer.de/content/dam/ise/de/documents/publications/studies/Photovoltaics-Report.pdf. Accessed: 2018-08-11. 2

[8] H. P. Mahabaduge et al. High-efficiency, flexible cdte solar cells on ultra-thin glass substrates. *Appl. Phys. Lett.*, page 133501, 2016. 2

[9] Friedrich Kessler and Dominik Rudmann. Technological aspects of flexible cigs solar cells and modules. *Solar Energy*, 77:685–695, 2004. 2

[10] Abundance of elements in earth's crust. https://en.wikipedia.org/wiki/Abundance_of_elements_in_Earth$%$27s_crust. Accessed: 2018-08-12. 2, 3

[11] National Renewable Energy Laboratory. Best research-cell efficiencies, 2018. 2, 3, 6, 7, 8

[12] Julian Burschka,Norman Pellet et al. Sequential deposition as a route to high-performance perovskite-sensitized solar cells. *Nature*, 499:316319, 2013. 3

[13] Mingzhen Liu et al. Efficient planar heterojunction perovskite solar cells by vapour deposition. *Nature*, 501:395398, 2013. 3

[14] Lingbo Li et al. Recent advances of exible perovskite solar cells. *Journal of Energy Chemistry*, 27:673–689, 2018. 3

[15] Alexander D. Jodlowski et al. Large guanidinium cation mixed with methylammonium in lead iodide perovskites for 19% efficient solar cells. *Nature Energy*, 2:972–979, 2017. 4, 10

[16] Konrad Domanski et al. Michael Saliba, Taisuke Matsui. Incorporation of rubidium cations into perovskite solar cells improves photovoltaic performance. *Science*, 10:1126, 2016. 4, 10

[17] JinWook Lee et al. Stabilizing perovskite structures by tuning tolerance factor: Formation of formamidinium and cesium lead iodide solid-state alloys. *Adv. Energy Mater.*, 5:1501310, 2015. 4, 10

[18] Dibyashree Koushik et al. High-efficiency humidity-stable planar perovskite solar cells based on atomic layer architecture. *Energy Environ. Sci.*, 10:91–100, 2017. 4, 10

[19] Malgorzata Kot et al. Improvement of the humidity stability of organic inorganic perovskite solar cells using ultrathin al_2o_3 layers prepared by atomic layer deposition. *ChemSusChem*, 9:3401–3406, 2016. 4

[20] Jiangzhao Chen and Nam-Gyu Park. Inorganic hole transporting materials for stable and high efficiency perovskite solar cells. *J. Phys. Chem. Lett*, 122:14039–14063, 2018. 4, 10, 11, 12

[21] Seong Sik Shin et al. Colloidally prepared la-doped $basno_3$ electrodes for efficient, photostable perovskite solar cells. *Science*, 356:167–171, 2017. 4, 10

[22] Dae-Yong Son et al. Self-formed grain boundary healing layer for highly efficient ch3nh3pbi3 perovskite solar cells. *NATURE ENERGY*, 1:1–8, 2016. 4, 10

[23] Kelvin H. L. Zhang et. al. Electronic structure and band alignment at the nio and srtio3 pn heterojunctions. *ACS Appl. Mater. Interfaces*, 9:26549–26555, 2017. 4, 12, 43, 45

[24] Hefei Liu et al. Nano-structured electron transporting materials for perovskite solar cells. *Nanoscale*, 8:6209–6221, 2016. 4

[25] Hong Zhang et al. Pinhole-free and surface-nanostructured niox film by room-temperature solution process for high-performance flexible perovskite solar cells with good stability and reproducibility. *ACS Nano*, 10:15031511, 2016. 4, 12, 13, 14

[26] Jong Hoon Park et al. Efficient ch3nh3pbi3 perovskite solar cells employing nanostructured ptype nio electrode formed by a pulsed laser deposition. *Adv. Mater.*, 27:4013, 2015. 4

[27] Fengxian Xie et al. Vertical recrystallization for highly efficient and stable formamidinium-based inverted-structure perovskite solar cells. *Energy Environ. Sci.*, 10:1942, 2017. 4, 12, 13

[28] Shizhong Yue et. al. Efficacious engineering on charge extraction for realizing highly efficient perovskite solar cells. *Energy Environ. Sci*, 10:2570–2578, 2017. 4, 13, 43, 45

[29] Elijah Thimsen et al. Energy levels, electronic properties, and rectification in ultrathin p-nio films synthesized by atomic layer deposition. *J. Phys. Chem. C*, 2012. 4, 13, 33

[30] Manisha Tyagi et. al. Electronic structure of 3d-transition-metal oxides: on-site coulomb repulsion versus covalency. *J. Mater. Res.*, 28:723732, 2013. 4, 46, 47, 49, 52

[31] Seongrok et. al Seo. An ultra-thin, un-doped nio hole transporting layer of highly efficient (16.4%) organic-inorganic hybrid perovskite solar cells. *Nanoscale*, 8:11403–11412, 2016. 4, 14, 33, 38, 39, 40, 45, 50, 52, 58, 61, 63, 68

[32] Seongrok Seo et al. Perovskite solar cells with inorganic electron- and hole- transport layers exhibiting long-term (500 h) stability at 85 c under continuous 1 sun illumination in ambient air. *Adv. Mater.*, page 1801010, 2018. 4, 14, 63

[33] Helen Megaw. Crystal structure of barium titanate. *Nature*, 1945. 6

[34] Akihiro Kojima et al. Organometal halide perovskites as visible-light sensitizers for photovoltaic cells. *J. AM. CHEM. SOC.*, 131:60506051, 2009. 6, 7

[35] Teck Ming Koh et al. Formamidinium-containing metal-halide: An alternative material for near-ir absorption perovskite solar cells. *J. Phys. Chem. C*, 118:1645816462, 2014. 6

[36] Dong Soo Kim and Hee Chul Lee. Nickel vacancy behavior in the electrical conductance of nonstoichiometric nickel oxide film. *J. Appl. Phys.*, 112:034504, 2012. 6, 61, 68

[37] F. Hao et al. Lead-free solid-state organicinorganic halide perovskite solar cells. *Nat. Photonics*, 8:489–494, 2014. 6

[38] Jin Hyuck Heo et al. Planar ch3nh3pbbr3 hybrid solar cells with 10.4 % power conversion efficiency, fabricated by controlled crystallization in the spincoating process. *Nat. Photonics*, 26:8179–8183, 2014. 6

[39] Qi Chen et al. The optoelectronic role of chlorine in ch3nh3pbi3(cl)-based perovskite solar cells. *Nat. Communications*, 6:7269, 2015. 6

[40] Shivam Singh et al. Effect of thermal and structural disorder on the electronic structure of hybrid perovskite semiconductor ch3nh3pbi3. *J. Phys. Chem. Lett.*, 2016. 6

[41] A.S. Bhalla et al. The perovskite structure a review of its role in ceramic science and technology. *Mater. Res. Innovations*, 4:3–26, 2000. 7

[42] Taame Abraha Berhe et al. Organometal halide perovskite solar cells: degradation and stability. *Mater. Res. Innovations*, 9:323, 2016. 7, 9

[43] Martin A. Green et al. The emergence of perovskite solar cells. *Nat. Photonics*, 8:506, 2014. 7

[44] Stefaan De Wolf et al. Organometallic halide perovskites: Sharp optical absorption edge and its relation to photovoltaic performance. *J. Phys. Chem. Lett.*, 5:1035–1039, 2014. 7, 8

[45] Norman Pellet et al. Mixed-organic-cation perovskite photovoltaics for enhanced solar-light harvesting. *Angew. Chem. Int. Ed.*, 2014. 7

[46] Sneha A. Kulkarni et al. Band-gap tuning of lead halide perovskites using a sequential deposition process. *J. Mater. Chem. A*, 2:9221, 2014. 7

[47] Rohit Prasanna et al. Band gap tuning via lattice contraction and octahedral tilting in perovskite materials for photovoltaics. *Materials today*, 139:1111711124, 2017. 7, 56

[48] Giacomo Giorgi and Koichi Yamashita. Organicinorganic halide perovskites: an ambipolar class of materials with enhanced photovoltaic performances. *J. Mater. Chem. A*, 3:8981–8991, 2015. 7

[49] Samuel D. Stranks et al. Electron-hole diffusion lengths exceeding 1 micrometer in an organometal trihalide perovskite absorber. *Science*, 342:341–344, 2013. 7

[50] Tze Chien Sum and Nripan Mathews. Advancements in perovskite solar cells: photophysics behind the photovoltaics. *Energy Environ. Sci.*, 7:2518–2534, 2014. 7

[51] pv-magazine. `https://www.pv-magazine.com/2018/06/26/oxford-pv-hits-world-record-efficiency-for-perovskite-silicon-tandem-cell/`. Accessed: 2018-07-30. 8

[52] Jack Chun-Ren Ke et al. In situ investigation of degradation at organometal halide perovskite surfaces by x-ray photoelectron spectroscopy at realistic water vapour pressure. *Chem. Commun.*, 53:5231, 2017. 9, 48

[53] Youzhen Li et al. Degradation by exposure of coevaporated ch3nh3pbi3 thin films. *J. Phys. Chem. C*, 119:2399624002, 2015. 9, 48

[54] Bertrand Philippe et al. Chemical and electronic structure characterization of lead halide perovskites and stability behavior under different exposures – a photoelectron spectroscopy investigation. *Chem. Mater*, 27:1720–1731, 2015. 9

[55] Guangda Niu et al. Study on the stability of ch3nh3pbi3 films and the effect of post-modification by aluminum oxide in all-solid-state hybrid solar cells. *J. Mater. Chem. A*, 2:705–710, 2014. 9

[56] Qi Wang et al. Qualifying composition dependent p and n self-doping in ch3nh3pbi3. *Appl. Phys. Lett.*, 105:163508, 2014. 9

[57] Wan-Jian Yin et al. Unusual defect physics in ch3nh3pbi3 perovskite solar cell absorber. *Appl. Phys. Lett.*, 104:063903, 2014. 9

[58] Bert Conings et al. Intrinsic thermal instability of methylammonium lead trihalide perovskite. *Adv. Energy Mater.*, 5:1500477, 2015. 9

[59] Nam-Koo Kim et al. Investigation of thermally induced degradation in ch3nh3pbi3 perovskite solar cells using in-situ synchrotron radiation analysis. *Scientific Reports*, 7:4645, 2017. 9

[60] Tomas Leijtens et al. Towards enabling stable lead halide perovskite solar cells; interplay between structural, environmental, and thermal stability. *J. Mater. Chem. A*, 5:11483, 2017. 9

[61] Youzhen Li et al. Light-induced degradation of ch3nh3pbi3 hybrid perovskite thin film. *J. Phys. Chem. C*, 121:39043910, 2017. 9

[62] Nicholas Aristidou et al. Fast oxygen diffusion and iodide defects mediate oxygen-induced degradation of perovskite solar cells. *NATURE COMMUNICATIONS*, 8:15218, 2017. 9

[63] Feng Hao et al. Lead-free solid-state organicinorganic halide perovskite solar cells. *Nature Photonics*, 8:489–494, 2014. 9

[64] S. Shao et al. Citation for: Highly reproducible snbased hybrid perovskite solar cells with 9% efficiency. *Adv. Energy Mater.*, 2018. 9

[65] Michael Saliba et al. How to make over 20% efficient perovskite solar cells in regular (nip) and inverted (pin) architectures. *Chem. Mater.*, 2018. 9

[66] Young Yun Kim et al. Fast two-step deposition of perovskite via mediator extraction treatment for large-area, high-performance perovskite solar cells. *J. Mater. Chem. A*, 6:12447–12454, 2018. 9

[67] Yan-Zhen Zheng et al. Hexamethylenetetramine-mediated growth of grain-boundary-passivation ch3nh3pbi3 for highly reproducible and stable perovskite solar cells. *Journal of Power Sources*, 377:103–109, 2018. 9

[68] W. Tress et al. Understanding the rate-dependent jv hysteresis, slow time component, and aging in ch3nh3pbi3 perovskite solar cells: the role of a compensated electric field. *Energy Environ. Sci.*, 8:995–1004, 2015. 9

[69] Christopher Eames et al. Ionic transport in hybrid lead iodide perovskite solar cells. *NATURE COMMUNICATIONS*, 6:7497, 2015. 9

[70] Yuchuan Shao et al. Origin and elimination of photocurrent hysteresis by fullerene passivation in ch3nh3pbi3 planar heterojunction solar cells. *NATURE COMMUNICATIONS*, 5:5784, 2014. 9

[71] Wenzhe Li et al. Effect of cesium chloride modification on the film morphology and uv-induced stability of planar perovskite solar cells. *J. Mater. Chem. A*, 4:11688, 2016. 10

[72] Michael Saliba and Taisuke Matsui et al. Cesium-containing triple cation perovskite solar cells: improved stability, reproducibility and high efficiency. *Energy Environ. Sci.*, 9:1989, 2016. 10, 30, 55

[73] Karunakara Moorthy Boopathi et al. Synergistic improvements in stability and performance of lead iodide perovskite solar cells incorporating salt additives. *J. Mater. Chem. A*, 4:1591, 2016. 10

[74] Xu Dong et al. Improvement of the humidity stability of organic inorganic perovskite solar cells using ultrathin al_2o_3 layers prepared by atomic layer deposition. *J. Mater. Chem. A*, 3:5360, 2015. 10

[75] Zonglong Zhu et al. Enhanced efficiency and stability of inverted perovskite solar cells using highly crystalline sno_2 nanocrystals as the robust electron-transporting layer. *Adv. Mater.*, 28:6478–6484, 2016. 10

[76] Ze Yu and Licheng Sun. Inorganic hole-transporting materials for perovskite solar cells. *Small Methods*, 2:1700280, 2018. 11, 12

[77] Daniel Perez del-Rey et al. Interfacial modification for high-efficiency vapor-phase-deposited perovskite solar cells based on a metal oxide buffer layer. *J. Phys. Chem. Lett*, 9:1041–1046, 2018. 12

[78] Anand S. Subbiah et al. Inorganic hole conducting layers for perovskite-based solar cells. *J. Phys. Chem. Lett.*, 5:17481753, 2014. 13, 14

[79] Wei Chen et al. Hybrid interfacial layer leads to solid performance improvement of inverted perovskite solar cells. *Energy Environ. Sci.*, 8:629–640, 2015. 13

[80] Kuo-Chin Wang et al. Low-temperature sputtered nickel oxide compact thin film as effective electron blocking layer for mesoscopic nio/ch3nh3pbi3 perovskite heterojunction solar cells. *ACS Appl. Mater. Interfaces*, 6:1185111858, 2014. 13

[81] T.F. Chen et. al. Property modulation of nio films grown by radio frequency magnetron sputtering. *Journal of Alloys and Compounds*, 643:167–173, 2015. 12, 68

[82] JunYuan Jeng et al. Nickel oxide electrode interlayer in ch3nh3pbi3 perovskite/pcbm planar-heterojunction hybrid solar cells. *Adv. Mater.*, 2014. 13, 59

[83] Long Hu et al. Sequential deposition of ch3nh3pbi3 on planar nio film for efficient planar perovskite solar cells. *ACS Photonics*, 1:547–553, 2014. 13, 59

[84] Zonghao Liu et al. Nickel oxide nanoparticles for efficient hole transport in p-i-n and n-i-p perovskite solar cells. *J. Mater. Chem. A*, 2017. 13, 53, 59, 64

[85] Zhiwen Qiu et. al. Enhanced physical properties of pulsed laser deposited nio films via annealing and lithium doping for improving perovskite solar cell efficiency. *Journal of Materials Chemistry C*, 5:7084, 2017. 13, 14, 45, 47, 49, 64

[86] Xingtian Yin et. al. Solvothermal derived crystalline niox nanoparticles for high performance perovskite solar cells. *Journal of Power Sources*, 329:398–405, 2016. 14, 50

[87] Che-Chen Hsu et. al. Atomic layer deposition of nio holetransporting layers for polymer solar cells. *Nanotechnology*, 26:385201, 2015. 14, 33, 38, 40, 68

[88] Jae Won Shim et. al. Polymer solar cells with nio hole-collecting interlayers processed by atomic layer deposition. *Organic Electronics*, 14:2802–2808, 2013. 14, 39, 40, 68

[89] Shashank Balasubramanyam et al. Plasma-enhanced atomic layer deposition of tungsten oxide thin films using (tbun)2(me2n)2wand o2 plasma. *J. Vac. Sci. Technol. A*, 2018. 15

[90] Saravana Balaji Basuvalingam et al. Comparison of thermal and plasma-enhanced atomic layer deposition of niobium oxide thin films. *J. Vac. Sci. Technol. A*, 2018. 15, 35

[91] H.C.M. Knoops, S.E. Potts, A.A. Bol, and W.M.M. Kessels. 27 - atomic layer deposition. 15

[92] Adrian Kitai. *Principles of Solar Cells, LEDs and Diodes: The role of the PN junction.* John Wiley and Sons, 2011. 19

[93] Sven Tougaard. Surface analysis — x-ray photoelectron spectroscopy. *Reference Module in Chemistry, Molecular Sciences and Chemical Engineering*, 2013. 20

[94] Richard T. Haasch. *X-Ray Photoelectron Spectroscopy (XPS).* Springer Science, 2014. 20

[95] Xps simplified. `https://xpssimplified.com/UPS.php`. Accessed: 2018-04-23. 21

[96] Nist database. `https://srdata.nist.gov/xps/selEnergyType.aspx`. Accessed: 2018-04-19. 22

[97] Electronegativity chart. `https://periodictable.me/electronegativity-chart`. Accessed: 2018-04-23. 22

[98] Stefan Hufner. *Photoelectron Spectroscopy Principles and Applications.* Springer, 2003. 22, 42, 43

[99] Antoine Kahn. Fermi level, work function and vacuum level. *Mater. Horiz.*, 3:7–10, 2016. 25

[100] Iain D. Baikie et al. Ambient pressure photoemission spectroscopy of metal surfaces. *Phys. Status Solidi C*, 323:45–53, 2014. 26

[101] R. H Fowler et al. The analysis of photoelectric sensitivity curves for clean metals at various temperatures. *Phys. Status Solidi C*, 38:45–56, 1931. 26

[102] Kptechnology. `http://www.kelvinprobe.com/products_info.php?ind=1`. Accessed: 2018-07-02. 26

[103] Ratnesh Sharma et al. Effect of cobalt doping on micro structural and optical properties of nickel oxide thin films. *Materials Science in Semiconductor Processing*, 23:42–49, 2014. 27

[104] Douglas J.C. Gomes et al. Using a monocular optical microscope to assemble a wetting contact angle analyser. *Measurement*, 46:3623–3627, 2013. 27

[105] Britannica. `https://www.britannica.com/technology/scanning-electron-microscope`. Accessed: 2018-08-02. 28

[106] Britannica. `https://www.britannica.com/technology/transmission-electron-microscope`. Accessed: 2018-08-02. 29

[107] jeol. `https://www.jeol.co.jp/en/words/emterms/search_result.html?keyword=HAADF-STEM`. Accessed: 2018-08-02. 29

[108] Mark Lundstrom. Introduction to photovoltaics. `https://www.slideshare.net/Jupiter276/20110720-ncnsc01lundstrom`. Accessed: 2018-07-19. 31

[109] Feilong Cai et al. Eliminated hysteresis and stabilized power output over 20 percent in planar heterjonction perovskite solar cells by compositional and surface modification to the low-temperature-processed tio layer. *J. Mater. Chem. A*, 2017. 32

[110] Julien Bachmann et al. Stoichiometry of nickel oxide films prepared by ald. *Chem. Vap. Deposition*, 2011. 33

[111] H. L. Lu et. al. Atomic layer deposition of nio films on si(100) using cyclopentadienyl-type compounds and ozone as precursors. *The Electrochemical Society*, 155:H807–H811, 2008. 33

[112] Taek Seung Yang et al. Atomic layer deposition of nickel oxide films using ni(dmamp)2 and water. *J. Vac. Sci. Technol. A*, 2005. 33, 38

[113] Seul Ji Song et al. Substrate dependent growth behaviors of plasma-enhanced atomic layer deposited nickel oxide films for resistive switching application. *Chem. Mater.*, 2012. 33, 34, 36

[114] Masato ISHIKAWA et al. Ni precursor for chemical vapor deposition of nisi. *Japanese Journal of Applied Physics*, 2011. 34, 35

[115] Laurent BRISSONNEAU et al. Ni precursor for chemical vapor deposition of nisi. *Japanese Journal of Applied Physics*, 2000. 34

[116] Jong-Hee Park and T.S. Sudarshan, editors. *Chemical Vapor Deposition*. ASM International, 2001. 35, 36

[117] H.D. Kaesz et al. Deposition of transition metal and mixed metal thin films from organometallic precursors. *New journal of Chemistry*, 1990. 35

[118] Erik Lindahl et al. Atomic layer deposition of nio by the ni(thd)2/h2o precursor combination. *Chem. Vap. Deposition*, 2009. 35

[119] Jeong Hwan Han et al. Reaction chemistry during the atomic layer deposition of sc2o3 and gd2o3 from sc(mecp)3, gd(iprcp)3, and h2o. *Chem. Mater.*, 26:1404–1412, 2014. 36

[120] J. W. Elam et al. Mechanism for zirconium oxide atomic layer deposition using bismethylcyclopentadienylmethoxymethyl zirconium. *Appl. Phys. Lett.*, 2007. 36

[121] H. Kumagai et al. Preparation and characteristics of nickel oxide thin film by controlled growth with sequential surface chemical reactions. *, J. Mater. Sci. Lett*, 1996. 38

[122] Byung-Soo So et al. Crystallization of amorphous silicon thin films using self-limiting ald of nickel oxide. *Electrochem. Solid-State Lett*, 2007. 38

[123] Mikko Utriainen et al. Studies of nio thin film formation by atomic layer epitaxy. *Mater. Sci. Eng. B.*, 1998. 38

[124] Mikko Utriainen et al. Studies of metallic thin film growth in an atomic layer epitaxy reactor using m (acac)2 m (ni, cu, pt) precursors. *Appl. Surf. Sci*, 2000. 38

[125] Sawanta S. Mali et. al. Nanoporous p-type niox electrode forp-i-n inverted perovskite solar celltoward air stability. *Materials Today*, 2017. 38

[126] Christopher B. Jacobs et. al. Imaging of electrical response of niox under controlled environment with sub-25-nm resolution. *J. Photon. Energy*, 6:038001, 2016. 38

[127] Juncheng Hu et. al. Preparation and surface activity of single-crystalline nio(111) nanosheets with hexagonal holes: A semiconductor nanospanner. *Adv. Mater*, 20:267–271, 2008. 38

[128] M. Schulze et. al. Photoelectron study of electrochemically oxidized nickel and water adsorption on dened nio surface layers. *Electrochimica Acta*, 44:3969–3976, 1999. 38

[129] M. A. Langell et. al. Stabilization of nio(lll) thin films by surface hydroxyls. *J. Phys. Chem.*, 99:4162–4169, 1995. 38, 39

[130] Jeffrey M. McKay and Victor E. Henrich. Surface electronic structure of nio: Defect states, o2 and h2o interactions. *PHYSICAL REVIEW B*, 32:6765, 1985. 38

[131] Zonglong Zhu et. al. High-performance hole-extraction layer of solgel-processed nio nanocrystals for inverted planar perovskite solar cells. *Angew. Chem. Int. Ed.*, 53:1257112575, 2014. 39, 40, 68

[132] Md. Bodiul Islam et. al. Niox hole transport layer for perovskite solar cells with improved stability and reproducibility. *ACS Omega*, 2:22912299, 2017. 39, 47, 68

[133] Laura Maria Manceriu et. al. Straightforward prediction of the ni1xo layers stoichiometry by using optical and electrochemical measurements. *J. Phys. D: Appl. Phys*, 50:225501, 2017. 39, 42, 45, 49, 68

[134] M.A. Langell et al. Adsorption of acetic acid on hydroxylated nio(111) thin films. *Surface Science*, 320:25–38, 1994. 39

[135] B.P. Payne et al. The study of polycrystalline nickel metal oxidation by water vapour. *Journal of Electron Spectroscopy and Related Phenomena*, 175:55–65, 2009. 39

[136] Jesse R. Manders et. al. Solution-processed nickel oxide hole transport layers in high effi ciency polymer photovoltaic cells. *Adv. Funct. Mater.*, 23:2993–3001, 2013. 40, 49, 61, 62, 68

[137] Jie Cao et. al. Low-temperature solution-processed niox films for air-stable perovskite solar cells. *J. Mater. Chem. A*, 5:1107111077, 2017. 40, 68

[138] R Zimmermann et. al. Electronic structure of 3d-transition-metal oxides: on-site coulomb repulsion versus covalency. *J. Phys.: Condens. Matter*, 11:16571682, 1999. 42

[139] Claudia Rdl and Andr Schleife. Photoemission spectra and effective masses of n- and p-type oxide semiconductors from first principles: Zno, cdo, sno2, mno, and nio. *Phys. Status Solidi A*, 211:74–81, 2014. 42, 43

[140] J.H. Scofield. 43

[141] D. E. Eastman and J. L. Freeouf. Photoemission partial state densities of overlapping p and d states for nio, coo, feo, mno, and cr2o3. *Physical review letters*, 34:395, 1975. 43

[142] Fei Jiang et. al. Post-treatment-free solution-processed non-stoichiometric nio x nanoparticles for effi cient hole-transport layers of organic optoelectronic devices. *Adv. Mater.*, 27:2930–2937, 2015. 43, 45

[143] Jeonggi Kim et. al. Solution-processed nickel oxide nanoparticles with niooh for hole injection layers of high-efficiency organic light-emitting diodes. *Nanoscale*, 8:17608, 2016. 43, 45

[144] Lifang Wei et. al. Valence band edge shifts and charge-transfer dynamics in li-doped nio based p-type dsscs. *Electrochimica Acta*, 188:309–316, 2016. 43, 45

[145] Guijun Li et. al. Overcoming the limitations of sputtered nickel oxide for high-efficiency and large-area perovskite solar cells. *Adv. Sci.*, 2017. 45

[146] Uisik Kwon et. al. Solution-processible crystalline nio nanoparticles for high- performance planar perovskite photovoltaic cells. *Scientific Reports*, 6:30759, 2016. 45

[147] A. B. Huang et. al. Achieving high-performance planar perovskite solar cells with co-sputtered co-doping niox hole transport layers by efficient extraction and enhanced mobility. *J. Mater. Chem. C*, 4:10839, 2016. 45

[148] Sven Tengeler et. al. The impact of different si surface terminations in the (001) n-si/niox heterojunction on the oxygen evolution reaction (oer) by xps and electrochemical methods. *Journal of The Electrochemical Society*, 165:H3122–H3130, 2018. 45

[149] Erin L. Ratcliff et. al. Evidence for near-surface niooh species in solution-processed niox selective interlayer materials: Impact on energetics and the performance of polymer bulk heterojunction photovoltaics. *Chem. Mater.*, 23:4988–5000, 2011. 45, 47, 52, 62, 68

[150] Mark T. Greiner et. al. Effects of processing conditions on the work function and energy-level alignment of nio thin films. *J. Phys. Chem. C*, 114:19777–19781, 2010. 45, 52, 62, 68

[151] Selina Olthof and Klaus Meerholz. Substrate-dependent electronic structure and film formation of mapbi3 perovskites. *Scientific Reports*, 7:40267, 2017. 44

[152] Elisa M. Miller et. al. Substrate-controlled band positions in ch3nh3pbi3 perovskite films. *Phys. Chem. Chem. Phys*, 16:22122–22130, 2014. 44

[153] Hui Wang et al. Nickel flux induced effects on structural and optical properties of nio films fabricated by pa-mocvd. *Vacuum*, 119:77–80, 2015. 47

[154] Xingtian Yin et. al. High efficiency hysteresis-less inverted planar heterojunction perovskite solar cells with a solution-derived niox hole contact layer. *J. Mater. Chem. A*, 3:24495, 2015. 47, 68

[155] M. Martnez-Gil et al. Influence of annealing temperature on nickel oxide thin films grown by chemical bath deposition. *Materials Science in Semiconductor Processing*, 72:37–45, 2017. 47

[156] Jiin-Long Yang et al. Effect of heat treatment on the properties of non-stoichiometric p-type nickel oxide films deposited by reactive sputtering. *Thin Solid Films*, 488:242–246, 2005. 49

[157] Ting Zhang et al. High speed and stable solution-processed triple cation perovskite photodetectors. *Adv. Optical Mater.*, 2018. 56

[158] Changlei Wang et al. Low-temperature plasma-enhanced atomic layer deposition of tin oxide electron selective layers for highly efficient planar perovskite solar cells. *J. Mater. Chem. A*, 2016. 56

[159] WILLIAM SHOCKLEY and HANS J. QUEISSER. Detailed balance limit of efficiency of p-n junction solar cells. *JOURNAL OF APPLIED PHYSICS*, 1960. 60

[160] Nandi Wu et al. Identifying the cause of voltage and fill factor losses in perovskite solar cells by using luminescence measurements. *Energy Technol.*, 2017. 60

[161] Pingli Qin et al. Transition metal oxides as hole-transporting materials in organic semiconductor and hybrid perovskite based solar cells. *Science China Chemistry*, 60:472–489, 2017. 61

[162] Gholamabbas Nazri et al. Angle-resolved infrared spectroelectrochemistry. 1. an in situ study of thin-film nickel oxide electrodes. *Langmuir*, 5:17–22, 1989. 61

[163] P.C. YU et al. In-situ spectroscopic studies of electrochromic hydrated nickel oxide films. *Solar Energy Materials*, 19:1–16, 1989. 61

[164] Ya-Huei Chang et al. A short-range ordereddisordered transition of a niooh/ni(oh)$_2$ pair induces switchable wettability. *Nanoscale*, 6:15309, 2014. 62

[165] Mohammad Javad Eslamibidgoli et al. Surface configuration and wettability of nickel(oxy)hydroxides: a first-principles investigation. *Phys.Chem.Chem.Phys.*, 19:22659, 2017. 62

[166] P.R. NORTON et. al. A photoemission study of the interaction of ni(100), (110) and (111) surfaces with oxygen. *Surface Science*, 65:13–36, 1977. 62

[167] K. S. KIM and NlCHOLAS WINOGRAD. X-ray photoelectron spectroscopic studies of nickel-oxygen surfaces using oxygen and argon ion-bombardment. *Surface Science*, 43:625–643, 1974. 62

[168] Jun He et al. Cu_2znsns_4 thin film solar cell utilizing rapid thermal process of precursors sputtered from a quaternary target: a promising application in industrial processes. *RSC Adv.*, 4:43080–43086, 2014. 66